Discrimination of cancer cells and tissues by applying advanced nonlinear microscopy techniques

Ph.D. Thesis

Evangelia Gavgiotaki

Heraklion, June 2019

FORTH
INSTITUTE OF ELECTRONIC STRUCTURE AND LASER

Discrimination of cancer cells and tissues by applying advanced nonlinear microscopy techniques

Ph.D. Thesis

Evangelia Gavgiotaki

Advisory Committee

Aggelaki Sofia, Prof., University of Crete **(Supervisor)**

Kotsakis Athanasios, Prof. Univeristy of Thessaly

Athanassaki Irene, Prof. University of Crete

Advisory Committee

Aggelaki Sofia, Prof. University of Crete **(Supervisor)**

Kotsakis Athanasios, Prof. Univeristy of Thessaly

Athanassaki Irene, Prof. University of Crete

Tzardi Maria, Prof. University of Crete

Georgoulias Vasilios, Prof. University of Crete

Anastasiadis Spiros, Prof. University of Crete

Mavroudis Dimitrios, Prof. University of Crete

Heraklion, June 2019

We acknowledge financial support from the Stavros Niarchos Foundation within the framework of the project ARCHERS (‘Advancing Young Researchers’ Human Capital in Cutting Edge Technologies in the Preservation of Cultural Heritage and the Tackling of Societal Challenges’).

We acknowledge support of this work by the project “Advanced Research Activities in Biomedical and Agro alimentary Technologies” (MIS 5002469) which is implemented under the “Action for the Strategic Development on the Research and Technological Sector”, funded by the Operational Programme ”Competitiveness, Entrepreneurship and Innovation” (NSRF 2014-2020) and co-financed by Greece and the European Union (European Regional Development Fund).

Co-financed by Greece and the European Union

Abstract

The aim of this thesis was to develop advanced new microscopic non-invasive techniques as novel diagnostic tools for cancer research. The past decades have seen the rapid development of imaging techniques that limited in visualizing the vasculature and organ structures. Until now the observation in cellular level requires tissue isolation and appropriate treatment for immunohistochemical, protein or molecular analysis. Non-linear microscopy offer non-invasive visualization in subcellular level, without the need of any preparation of the samples e.g. fixation or staining.

The main objective of this dissertation is the discrimination of cancer cells and tissues by developing non-destructive, label free microscope techniques. First , quantitative discrimination of the different subtypes of human breast cancer cell lines was achieved as compared to peripheral blood mononuclear cells (PBMCs) based on their lipid content. These results combined with Fourier Transform Infrared (FTIR) spectroscopy and provided additional valuable chemical information on breast cancer cells, correlating Third Harmonic Generation (THG) signal to lipid drafts . Furthermore, non-linear microscopy techniques were used as novel digital pathology methods in human breast cancer tissues. It was shown that the quantification of THG signals can differentiate malignant from normal breast tissue samples and distinguish the different grades of cancer. This study has a significant clinical potential since it can monitor quantitative changes in cellular behavior in healthy and pathological human tissues. Finally, the detection of mouse T cells activation achieved by using THG imaging in an attempt to follow the immune response development. THG signal was correlated with Raman Spectroscopy and implemented during T cell activation in the presence of higher concentration of cholesterol and lipids.

This essay provided an important opportunity to advance the understanding of cancer research by utilizing non-invasive innovative spectroscopic modalities. Both qualitative and quantitative approaches were employed in these investigations in case of cancer diagnosis and immunotherapy. The findings of this thesis revealed that non-linear microscopy techniques could be used as promising tools in the future for the determination of cancer limits at subcellular level during surgery.

Περίληψη

Στο πλαίσιο της διδακτορικής διατριβής αναπτύχθηκε μια νέα διαγνωστική/ απεικονιστική μη παρεμβατική τεχνική για την επίτευξη διαχωρισμού μεταξύ καρκινικών και φυσιολογικών κυττάρων. Η διακριτική ικανότητα των μέχρι σήμερα χρησιμοποιούμενων απεικονιστικών τεχνικών in vivo περιορίζεται στο επίπεδο του οργάνου και της αγγείωσης αυτού χωρίς να μπορεί να διεισδύσει σε κυτταρικό επίπεδο. Η όποια μελέτη σε επίπεδο κυττάρου επιβάλλει την απομόνωση του ιστού και την κατάλληλη επεξεργασία για ανοσοϊστοχημική, πρωτεϊνική ή μοριακή ανάλυση. Η μη γραμμική μικροσκοπία παρέχει μια μη παρεμβατική απεικόνιση των υποκυττάριων δομών. Επιπλέον δεν υπάρχει αναγκαιότητα μονιμοποίησης ή χρώσης του κυττάρου.

Στη παρούσα διατριβή πραγματοποιήθηκαν απεικονιστικές μετρήσεις σε μη σημασμένες καρκινικές κυτταρικές σειρές, αντιπροσωπευτικές τριών διαφορετικών υποτύπων καρκίνου μαστού για να ταυτοποιηθεί το προφίλ του μη γραμμικού σήματος Γένεσης Τρίτης Αρμονικής (THG) συχνότητας από τα υπό ακτινοβόληση δείγματα (Κεφάλαιο 5). Παρατηρήθηκε ότι με τη χρήση THG απεικόνισης ως καινοτόμου διαγνωστικού εργαλείου μπορεί να γίνει κατηγοριοποίηση των διαφόρων υποτύπων των καρκινικών σειρών με βάση τη ποσότητα των ενδοκυττάριων λιπιδικών εναποθέσεων ανά επιφάνεια κυττάρου. Παράλληλα έγινε έλεγχος του προφίλ της THG απεικόνισης σε μονοπύρηνα κύτταρα περιφερικού αίματος (PBMCs) φυσιολογικών αιμοδοτών έτσι ώστε να γίνει σύγκριση και διαφοροποίηση των καρκινικών σειρών από τα φυσιολογικά κύτταρα.

Για τη διάκριση των φυσιολογικών κυττάρων από τα καρκινικά χρησιμοποιήθηκε ένας αλγόριθμος (MATLAB) βασισμένος στα συλλεγόμενα σήματα THG . Πιο συγκεκριμένα ο αλγόριθμος αυτός μελετά την κατανομή, το μέγεθος και τη σύσταση των ενδοκυττάριων λιπιδικών σωματίων με στόχο να γίνει η διάκριση των φυσιολογικών κυττάρων του περιφερικού αίματος από τα καρκινικά κύτταρα. Τα αποτελέσματα έδειξαν ότι με τη μέθοδο της THG μπορεί να γίνει στατιστικά σημαντική διάκριση και σαφής διαχωρισμός των διαφόρων υποτύπων των καρκινικών σειρών από τα φυσιολογικά κύτταρα ως προς την ποσότητα των ενδοκυττάριων λιπιδικών εναποθέσεων.

Στη συνέχεια διεξήχθησαν βιοχημικές μετρήσεις με τη μέθοδο φασματοσκοπίας υπερύθρου FTIR με στόχο τη συσχέτιση και επεξήγηση των αποτελεσμάτων της ποσοτικοποίησης του συλλεγόμενου σήματος της τρίτης αρμονικής με βιοχημικές πληροφορίες. Τα αποτελέσματα αυτής της μελέτης έδειξαν ότι υπάρχουν χημικές αλλαγές στις λιπιδικές εναποθέσεις που συμβάλουν στη διαφοροποίηση μεταξύ καρκινικών σειρών σε σχέση με τα φυσιολογικά κύτταρα. Πιο συγκεκριμένα το υψηλότερο σήμα της τρίτης αρμονικής συσχετίστηκε με τις λιπιδικές σχεδίες (lipid rafts) στις κυτταρικές μεμβράνες λόγω της αυξημένης συγκέντρωσης της χοληστερόλης. Η εφαρμογή της προτεινόμενης έρευνας θα οδηγήσει στην ανάπτυξη νέας τεχνολογίας όπου ο συνδυασμός της μη-γραμμικής μικροσκοπίας με

άλλες τεχνικές θα μπορεί να οδηγεί στο διαχωρισμό των καρκινικών κυττάρων έναντι των φυσιολογικών στην περίπτωση καρκινικών κυκλοφορόντων κυττάρων (CTCs).

Στην συνέχεια χρησιμοποιώντας την αποκτηθείσα γνώση και εμπειρία, έγινε προσπάθεια διάκρισης ενεργοποιημένων και μη Τ λεμφοκυττάρων από σπλήνα ποντικού και ποσοτικοποίηση των διάφορων σταδίων ενεργοποίησης τους μέσω της καταγραφής του σήματος THG (Κεφάλαιο 7). Πιο συγκεκριμένα χρησιμοποιήθηκαν δυο διαφορετικοί τρόποι ενεργοποίησης με την χρήση της μιτογόνου ουσίας concanavalin-A; (ConA) και του ειδικού αντιγόνου human serum albumin; (HSA) για την παρακολούθηση τους στο μη γραμμικό μικροσκόπιο. Οι ποιοτικές και ποσοτικές αναλύσεις μέσω της THG έδειξαν στατιστικά σημαντική αλλαγή στον αριθμό των ενδοκυττάριων λιπιδικών εναποθέσεων κατά την ενεργοποίηση των Τ λεμφοκυττάρων σε σχέση με τα μη ενεργοποιημένα κύτταρα. Επιπλέον για την συσχέτιση του σήματος της τρίτης αρμονικής με χημική πληροφορία πραγματοποιήθηκαν μετρήσεις φασματοσκοπίας Raman και απέδειξαν σημαντικές αλλαγές στους διαφορετικούς τρόπους ενεργοποίησης καθώς και στην συσχέτιση με τα μη ενεργοποιημένα κύτταρα. Ειδικά η ανάλυση με γραμμική προσαρμογή (linear fitting) έδειξε υψηλή συσχέτιση του σήματος τρίτης αρμονικής με δεσμούς λιπιδικών εναποθέσεων, χοληστερόλης όμως όχι τριγλυκεριδίων . Η μελέτη αυτή αναμένεται να προσφέρει σημαντικές καινοτόμες πληροφορίες για τις βιολογικές διεργασίες των Τ λεμφοκυττάρων, ενώ ταυτόχρονα θα μπορεί να προσφέρει τον άμεσο εντοπισμό των ενεργοποιημένων κυττάρων στη διαγνωστική της ανοσοθεραπείας.

Παράλληλα, χρησιμοποιήθηκε η τεχνολογία της μη γραμμικής μικροσκοπίας στη μελέτη καρκινικών και φυσιολογικών ιστών μαστού (Κεφάλαιο 6). Ειδικότερα, χρησιμοποιήθηκαν τα μη γραμμικά φαινόμενα γένεσης δεύτερης αρμονικής (SHG) για την παρακολούθηση της κατανομής του κολλαγόνου και τρίτης αρμονικής (THG) για την αποκάλυψη λιπιδικών εναποθέσεων, ανομοιογενειών και διεπιφανειών στον ιστό. Οι ιστοί που μελετήθηκαν είναι από φυσιολογικούς μάρτυρες (control) και από ασθενείς σε διαφορετικό στάδιο ανάπτυξης του καρκίνου (grade I-III) . Τα πειραματικά αποτελέσματα από την ποσοτική ανάλυση μέσω τρίτης αρμονικής είναι ιδιαιτέρως ενθαρρυντικά και έδειξαν ότι μπορεί να γίνει διάκριση των καρκινικών κυττάρων στον ιστό βασιζόμενη στις μεμβράνες και στις λιπιδικές εναποθέσεις και η διαφοροποίησή τους από τα φυσιολογικά κύτταρα. Παράλληλα επιτεύχθηκε διαχωρισμός των διάφορων σταδίων (grade I-III) του καρκινικού ιστού μαστού βασιζόμενο στις λιπιδικές εναποθέσεις και τις ανομοιογένειες .

Συμπληρωματικά, βασιζόμενοι στα εξαγόμενα μορφολογικά χαρακτηριστικά των κυττάρων, χωρίς την χρήση καμίας χρώσης μόνο με την συλλογή των μη γραμμικών σημάτων, υπολογίστηκε ο λόγος της επιφάνειας του πυρήνα προς την επιφάνεια του κυτταροπλάσματος που είναι ένας από τους ευρέως γνωστούς τρόπους διάγνωσης καρκινικών ιστών από τους παθολογοανατόμους. Επιπλέον, μέσω της συλλογής των μη γραμμικών σημάτων (ένταση, αριθμός λιπιδικών εναποθέσεων και όγκος κυττάρου) έγινε διάκριση των καρκινικών κυττάρων στην περιοχή σάρωσης και εκτίμηση του ποσοστού των καρκινικών κυττάρων στον ιστό.

Στην συνέχεια πραγματοποιήθηκε μελέτη φασματοσκοπίας FTIR στους ιστούς για την συσχέτιση των μη γραμμικών σημάτων με βιοχημική πληροφορία. Η συσχέτιση αυτή υπέδειξε ότι βασιζόμενοι σε συγκεκριμένους λιπιδικούς δεσμούς μπορεί να υπάρξει συσχέτιση του μη γραμμικού σήματος της Τρίτης αρμονικής με τα λιπίδια και να επιτευχθεί η διάκριση του καρκινικού από το φυσιολογικό ιστό. Στο τελευταίο μέρος της διατριβής, έγινε προσπάθεια σάρωσης μεγαλύτερης επιφάνειας του ιστού (σε

επίπεδο χιλιοστού) μέσω της μη γραμμικής μικροσκοπίας.

Η σημαντικότητα της έρευνας αυτής είναι ότι η χρήση μη γραμμικών απεικονιστικών μετρήσεων χωρίς κάποια ιδιαίτερη προετοιμασία του δείγματος ή την χρήση σημάνσεων (markers) στον ιστό, προσφέρει τη δυνατότητα διαχωρισμού των φυσιολογικών από τους καρκινικούς ιστούς, σε αντίθεση με τις έως τώρα μοριακές μεθόδους που χρησιμοποιούνται στις κλινικές. Η μέθοδος της μη γραμμικής μικροσκοπίας προτείνεται ως ένα νέο καινοτόμο διαγνωστικό εργαλείο που θα μπορεί να χρησιμοποιηθεί για τον έλεγχο των υγιών ορίων σε επίπεδο κυττάρου κατά την διάρκεια επέμβασης.

To my family...

Acknowledgments

Undertaking this PhD has been a truly life-changing experience for me and it would not have been possible to do without the support and guidance that I received from many people.

Firstly, I would like to thank my supervisor Prof. Sofia Agelaki for her guidance , great support and kind advice throughout my PhD research studies.

Moreover, I would like to express my sincere gratitude to my advisor Prof. Irene Athanassakis for the continuous support of my Ph.D study and related research, for her patience, motivation, and immense knowledge. Her guidance helped me in all the time of research and writing of this thesis. I could not have imagined having a better advisor and mentor for my Ph.D study.

Besides my advisors, I would like to thank the rest of my thesis committee: Prof. A. Kotsakis, Prof. V. Georgoulias, and Prof. M.Tzardi, for their insightful comments and encouragement, but also for the hard question which incented me to widen my research from various perspectives.

In particular, I would like to express my highest appreciation to my advisor Dr. George Filippidis. It would never have been possible for me to take this work to completion without his incredible support and encouragement. Moreover, his careful editing contributed enormously to the production of this thesis

My sincere thanks also goes to Dr. G. Kenanakis, Dr. I. Zerva, and Mrs. H. Markomanolaki, who provided me an opportunity to join their team as intern, and who gave me access to the laboratory and research facilities. Without their precious support it would not be possible to conduct this research.

I thank my fellow labmates for working together and for all the fun we have had in the last years V. Tsafas, S. Bovasianos, Dr. M. Mari.

Also I thank my friends in the IESL institution E. Serpetzoglou, I. Paradisanos, D. Angelaki, E. Kavatzikidou, V. Skoulas, N.Korakas, G. Kourmoulakis, G. Violakis.

Last but not the least, I would like to thank my family: my parents, my sister and my brothers for supporting me spiritually throughout writing this thesis. Thanks for all your encouragement!

Contents

1 Introduction **1**

2 Nonlinear Optical Microscopy **7**
2.1 Nonlinear Optics Background 8
2.2 Two Photon Excitation Fluorescence 12
2.3 Second Harmonic Generation 14
2.4 Third Harmonic Generation 18
2.5 Multi-contrast non-linear optical microscopes 22

3 Vibrational Spectroscopy **31**
3.1 FT-IR spectroscopy 34
3.1.1 Transmission method 36
3.1.2 Reflectance method ATR 37
3.1.3 FT-IR microspectroscopy 37
3.2 Raman spectroscopy 38

4 Methods **43**
4.1 Biological sample preparation 43
4.1.1 T cells 43
4.1.2 Breast cancer cell lines 45
4.1.3 Breast Tissues 46
4.2 Experimental Setups 47
4.2.1 Nonlinear Microscope 47
4.2.2 Raman Spectrometer 48
4.2.3 FTIR spectrometer 49
4.3 Data analysis 50
4.3.1 Signal's mean total area calculation 50
4.3.2 Signal's intensity calculation 50
4.3.3 Statistical analysis 51

5 Distinction between breast cancer cell subtypes using third harmonic generation microscopy 53
5.1 Breast cancer 53
5.2 THG microscopy as diagnostic tool for breast cancer cell lines 55

5.3 Quantification of THG signaling in breast cancer cell lines 65
5.4 FTIR spectroscopy and correlation to THG signal of breast cancer cell lines 70
5.5 Conclusion 75

6 THG microscopy in breast tissue **81**
6.1 Breast cancer and diagnosis 81
6.2 Nonlinear microscopy in cancer studies 82
6.3 Lipid Bodies as indicators in cancer 83
6.4 Non-linear imaging of breast tissues 83
6.5 Calculation of nuclear to cytoplasmic ratio 88
6.6 Quantification analysis 90
6.7 FTIR spectroscopy in breast tissues 95
6.8 Correlation of THG signal with FTIR spectra 99
6.9 Conclusion 100

7 Detection of the T cell activation state using non-linear optical microscopy **107**
7.1 T cells 107
7.2 Study of T cell activation via THG microscopy 110
7.3 Lipid Bodies and Inflammation 111
7.4 Non-linear microscopy applications in immunological studies 111
7.4.1 Discrimination between B and T cells 112
7.4.2 T cell activation 114
7.4.3 Quantification of THG signal area 115
7.5 Raman Spectroscopy of resting and activated T cells 118
7.6 Correlation THG signals with Raman spectra 123
7.7 Conclusion 125

8 Outlook and future aspects **131**

A Appendix A **135**
A.1 FTIR analysis in breast cancer cells 135

B Appendix B **141**
B.1 Cell segmentation 141
B.2 THG intensity quantification 143

List of Figures

2.1 Description of the interaction of light with matter. 8

2.2 Jablonski diagram one photon fluorescence, two-photon excitation fluorescence (TPEF), second-harmonic generation (SHG) and third harmonic generation (THG). Note that in SHG and THG no actual electronic excitation takes place. 10

2.3 Absorption spectra of major intracellular absorbers. The molecular extinction coefficients of oxygenated haemoglobin and melanin and the absorption coefficient of water are shown. Most animal cells and tissues are considered to be nearly transparent in the spectral range from about 700 nm to 1100 nm owing to the lack of efficient one-photon absorbers. 11

2.4 A demonstration of the localization of two-photon excitation volume. For two-photon excitation using a second objective with the same numerical aperture, fluorescence excitation occurs only from a 3D localized spot. 13

2.5 Second Harmonic generation. (a) Geometry of the interaction, (b) Spatial confinement of signal generation with nonlinear excitation (c) the wavelength description. 14

2.6 a. Energy level description of SHG b. Schematic diagram depicting ordered molecules at a small spherical surface. An ultrafast pump laser pumps light with frequency ω which generates light at 2ω from the locally non-centrosymmetric media [10] 15

2.7 Phase matching condition for SHG. a) Low-efficiency frequency doubling of light in a positive-index medium without phase-matching ($k_{2\omega} \neq 2k_{\omega}$, $n_{2\omega} \neq n_{\omega}$). b) phase-matching for SHG ($k_{2\omega} = 2k_{\omega}$), where the fundamental and harmonic waves possess the same index of refraction. The red- and blue-colored lines in the schematics represent the fundamental and second-harmonic waves, respectively. [11] 16

2.8 Endogenous second-harmonic-generation (SHG) imaging. (a)SHG image from skeletal muscle (b) SHG image from a mature rat tail tendon collagen (c) SHG imaging of starch grains in chloroplasts, (d)SHG arises from mitotic spindles and from interphase microtubule ensembles in red blood cells. 17

2.9 Forward detected polarization second harmonic generation imaging microscopy obtained from a fresh flour paste sample. The excitation linear polarization rotates counterclockwise between 0–170°, in steps of 10°. Arrows indicate the incident polarization. Scale bar is 10 μm. 18

2.10 Third Harmonic generation. (a) Geometry of the interaction, (b) Spatial confinement of signal generation with nonlinear excitation and (c) the wavelength description. . . 19

2.11 Intensity and phase distribution of a focused Gaussian beam. 2D distribution of intensity and phase near the focus. 20
2.12 For a material presenting a perfect dispersion compensation between frequencies ω and 3ω (implying that the phase matching condition $\Delta k = 3(k(\omega) + k_G) - k_{(3\omega)} = 0$ is satisfied), the momentum conservation of the respective photons can be met. However, no signal is generated due to destructive interference of THG waves. For common normal dispersive material ($n_{3\omega} > n_\omega$), momentum conservation condition cannot be met in any manner; and therefore, effective THG is not possible. If $n_{3\omega} < n_\omega$, efficient THG can occur since the angularly spread wave vectors of the focused fundamental beam can be added effectively so that the total momentum before and after the non-linear interaction is conserved [35] 21
2.13 THG optical microscopy applied in different biological models. 22
2.14 Multi-contrast non-linear imaging modalities (SHG, THG , TPEF) applied in different biological models. 23

3.1 Illustration of the different vibrational methods; absorption and Raman scattering [4]. 32
3.2 Illustration of the excitation of molecular vibrations in IR and Raman spectroscopy. In IR spectroscopy, the vibrational transitions are induced by absorption of light quanta from a continuous light source in IR spectral region. Vibrational Raman transitions correspond to inelastic scattering (ν_R scattering (ν_0) is represented by thick arrow. This is an example of SO_2 which is both IR and Raman active molecule. 33
3.3 Schematic diagram of Michelson Interferometer 35
3.4 Demonstration of FT-IR spectrometers in transmission method. 37
3.5 Schematic of a typical attenuated total reflectance cell. The diagram shows how the infrared light is directed into the ATR crystal, where it is totally internally reflected before passing to the detector. The sample is placed directly on top of the crystal as shown. 37
3.6 Energy diagram representing the elastic Rayleigh scattering and the inelastic anti-Stokes and Stokes Raman scattering. 39
3.7 Typical setup for a Raman spectrometer with a laser attached to a microscope [14]. . 40
3.8 An example of Raman spectra of a sample where interfere fluorescence (red) and normal Raman spectra (black) are shown for comparison. 40

4.1 Cells preparation for the performance of the non-linear imaging measurements. . . . 44
4.2 Tissues included in the present research 46
4.3 Nonlinear optical setup photograph (a) and the schematic diagram (b) 48
4.4 Horiba LabRAM HR Raman setup 49
4.5 FT-IR experimental setup - Bruker Vertex 70v spectrometer 50

5.1 Illustration of the different vibrational methods; absorption and Raman scattering [1]. 54
5.2 Cellular morphologic changes upon apoptosis inductions in tumor cells. MPEF in orange and THG in cyan [20]. 56

5.3 Identification of sub-cellular organelles of BV-2 cells that produce high THG signals. THG and TPEF images were collected simultaneously. (a) 2D image (500 x 500 pixels) of a BV-2 cell stained with nile red (THG in blue-green, TPEF in magenta, (b) 2D image of a BV-2 cell stained with Mitotracker red fm (THG in blue-green, TPEF in red), (c) 2D image of a BV-2 cell stained with Alexa 488 (THG in blue-green, TPEF in yellow). Scale bars denote 5 μm. 58
5.4 Quantitative correlation of TPEF and THG threshold images based on PCC analysis. The same stained control BV-2 cells as in Fig. 3 were implemented. (a) Nile red (lipid droplets, 53% correlation), (b) Mitotracker (mitochondria, 8% correlation), (c) Alexa 488 (late endosomes 0.4% correlation). Scale bars denote 5 μm. 59
5.5 THG images of BV-2 cells (a) control (b) activated. The scale bar depicts 5 μm. . . . 59
5.6 2D THG image of a cancer cell. Scale bar depicts 5 μm. 61
5.7 THG signal distribution (maximum z projections) of different cell types. Scale bar depicts 5 μm. 61
5.8 THG images (z-projection) of breast cancer cell lines and control cells. Luminal (MCF7 and T47D), HER2 positive (BT474 and SKBR3), triple negative (MDA-MB231 and Hs578T) cancer cell lines as well as non-tumorigenic MCF10a breast cells and control PBMCs were submitted to THG imaging as described in chapter methods The yellow arrows depict the amorphous nucleus and the enclosed nucleolus of cells. Scale bar depicts 5 μm. 63
5.9 SEM images of characteristics cells 64
5.10 2D THG images of MCF-7, SKBR3 and MCF10a cells (cyan) and 2D TPEF images of the same cells stained with Nile-Red (red). In the merged images (third column), the co-localization of THG-TPEF signals is presented in white color. The scale bar depicts 5 μm. 65
5.11 Quantification of THG signals using threshold images: (a) sequential 2D THG images of a cancer cell and below their threshold image respectively. 66
5.12 THG signal quantification depicted as (a) mean total area, (b) mean THG total area divided by the surface cell area. Data represent mean values $\pm$ S.E.M. (n=40 each case). The $***$ denotes p<0.005 statistical significance. 67
5.13 z projection THG images of cancer cell's parts (a) whole cell (b) cellular membrane (c) nucleus area and (d) intracellular area. Lower their threshold images are shown respectively. Scale bar depicts 5 μm. 68
5.14 THG area of the different cellular compartments (intracellular organelles, cellular membrane, nucleus) divided by the total area of each cell. 68
5.15 THG intensity. Data represent mean values $\pm$ S.E.M. (n=40 each case). The $***$ denotes p<0.005 statistical significance. 69

5.16 3D graph for the distinction between cancer and PBMCs cells via THG signals quantification. THG area/ surface area of the cell in x-axis, THG intensity values in y-axis and cell surface area in z- axis. The Her2 positive cancer cells (BT474 and SKBR3) and the PBMCs normal cells appeared clearly as separable sub populations of spots in the scatter plot (N=20 for each cell type). 70
5.17 FTIR spectra of cancer cell lines (BT474, MCF7, MDA-MB231) and control cells (PBMCs). 71
5.18 Schematic diagram of lipid raft. 71
5.19 2nd derivative of FTIR spectra of cancer cell lines (BT474, MCF7 , MDA-MB231) and control cells (PBMCs) specified in lipid regions a (3000-2800 cm^{-1}), b(1800-1450 cm^{-1}). 72
5.20 Percentage of FTIR 2nd derivative spectrum area at wavelengths 1737, 1746, 2845, 2853 and 2910 cm^{-1}. Data representing mean values of three single experiments of the five different peaks mainly correspond to lipid rafts. BT474 cells appear higher values as compared to MCF7, MDA-MB231 breast cancer cells and PBMCs. SEM is in the order of 25% of the values (not shown) due to the limited number of FTIR measurements (n=3 in each case). 73
5.21 Correlation of FTIR 2nd derivative spectra with THG (a, left column) mean area divided by the surface cell area and (b, right column) mean THG intensity values for specific peaks of spectrum of lipid regions. With exception of the mean THG intensity at 2853 cm^1 (R^2_{2853} = 0.4474, Figure 5.21b_4), in all other cases, satisfactory fitting values were obtained. 74

6.1 a) Schematic diagram of collecting multimodal nonlinear signal of breast tissue, b) Multimodal nonlinear image (MPEF, THG, SHG) . SHG (in red) indicates collagen ,THG (in cyan) reflects inhomogeneities of the sample and lipid droplets while MPEF (in yellow) distributes autofluorescence of the tissue. Scale bar depicts 100 μm. . . . 85
6.2 Illustration of human breast (a) and the different cases of ductal carcinoma in situ (b).[30] 86
6.3 Characteristic H&E stained images of the investigated breast tissues 87
6.4 Nonlinear images (a. SHG, b. THG) of breast cancer tissue and the multimodal nonlinear image with the corresponding sequential tissue section image of H&E stained. Scale bars denotes 100 μm 87
6.5 H&E images and the corresponding nonlinear images (SHG & THG) of benign and malignant (grade I, grade I , grade III) breast tissues. Characteristics THG images of tissues indicate LBs and inhomogeneities and SHG images collagen. Scale bar of nonlinear images depicts 5 μm. The squares in H&E images indicate the regions that were scanned via the performance of nonlinear imaging measurements. 88
6.6 Morphological characteristics of the cell in benign and cancerous tissues respectively via THG imaging. 89
6.7 THG images of cancerous tissues. Arrows depict the irregular nuclear (distributed as black area) of cells. 89

6.8 THG images of cells in cancerous tissues. Arrows depict the nucleoli located in nuclear area (interface of nucleus and nucleoli). 89
6.9 Calculation of N/C ratio of cells in benign (control) and cancerous tissues (grade I,II, III). 90
6.10 Illustration of THG tissue processing. The isolation of individual cells for quantification analysis (based on their LBs, membranes and inhomogeneities). Scale bar depicts 5 μm 91
6.11 Quantification of THG signal area of breast tissues (N=40 cells of each tissue) 91
6.12 Quantification of cell volume (N=40 cells of each tissue) 92
6.13 Quantification of mean THG signal area divided with cell volume (N=40 cells of each tissue) 92
6.14 Quantification of THG signal intensity (N=40 cells from each tissue). 93
6.15 3D graph for the distinction between cancerous and control tissues via THG signals quantification. THG area/ cell volume area of the cell in x-axis, THG intensity values in y-axis and mean THG area in z- axis. The grade III cancer tissue and the control tissue appeared clearly as separable sub populations of spots in the scatter plot (N=40 for each tissue type). 93
6.16 3D graph for the distinction between cancerous and control area tissues of a patient via THG signals quantification. THG area/ cell volume area of the cell in x-axis, THG intensity values in y-axis and mean THG area in z- axis. N=40 cells for each tissue. . 94
6.17 3D graph for the distinction between cancerous and control tissues of same patient via THG signals quantification. THG area/ cell volume area of the cell in x-axis, THG intensity values in y-axis and mean THG area in z- axis. N=40 cells for each tissue. . 94
6.18 Stack graphs of characteristic FTIR spectra of breast tissues. 96
6.19 Characteristic ATR spectra of breast tissues (control and cancerous). One representative area for each tissue is shown (N=2 patients for each state of tissue). 97
6.20 2nd derivative integrated area of ATR characteristic spectra. 99
6.21 Correlation of FTIR spectra correlated with mean THG area in specific lipid bonds. . 100
6.22 Correlation of FTIR spectra with mean THG area divided by cell volume in specific lipid bonds. 100

7.1 Image of a T cell. 108
7.2 Schematic diagram of personalized T cell therapy. 109
7.3 Image of killer T cells attacking a cancer cell. 109
7.4 Cell preparation for the performance of the non-linear imaging measurements. 113
7.5 Discrimination T cells of B cells by using anti-CD19PE staining. The first two (a, b) are B cells while the last present T cell (c) as not TPEF signal detected. Cells are visualized by THG imaging (first column), and TPEF imaging (second column). Merged signals are shown in third column. Scale bar depicts 2 μm. 114

7.6 THG images of T cells (a) control, (b) HSA activation and (c) Con A activation. A characteristic example of one cell out of at least 40 in each case is shown here. The white arrows depict nuclei while blue arrows show intracellular LBs. Scale bar depicts 2 μm. 114
7.7 THG images and the corresponding threshold images for THG intensity and THG area quantification. Scale bar depicts 3 μm. 115
7.8 Quantification of mean THG area of T cells before and after activation. N=40 for each case. 116
7.9 Quantification of mean THG area divided by cell volume of T cells before and after activation . N=40 for each case. 117
7.10 Quantification of mean THG area divided by cell volume of T cells before and after activation. N=40 for each case. 117
7.11 Characteristic Raman spectra and brightfield images of control and activated (Con A, HSA) T cells. One representative cell out of N=15 cells for control and for the two different ways of activation is shown here. 119
7.12 Line chart represents the concentration of lipid and phospholipids bonds of control and activated (Con A & HSA) T cells. Data represents mean values of N=15 cells for each case. Activated T cells appear higher values of lipid concentration as compared to control cells in most of the peaks. 122
7.13 Line chart represents the concentration of cholesterol (614 cm^{-1}, 1441 cm^{-1}, 1444-5 cm^{-1}, 1669 cm^{-1}) and triglycerides (1073 cm^{-1}, 1264 cm^{-1}, 1656 cm^{-1}) bonds of control and activated (ConA or HSA) T cells. Data represents mean values of N=15 cells for each case. 123
7.14 Correlation of Raman spectra with mean THG area in lipids, cholesterol and triglyceride peaks respectively. The mean values of fractions for $^{ConA}/_{control}$, $^{HSA}/_{control}$ and $^{ConA}/_{HSA}$ were calculated from Table 7.1 for Raman spectra and from Figure 7.8 for THG area. 124
7.15 Correlation of Raman spectra with mean THG signal intensity in lipids, cholesterol and triglyceride peaks respectively. The mean values of fractions for $^{ConA}/_{control}$, $^{HSA}/_{control}$ and $^{ConA}/_{HSA}$ were calculated from Table7.1 for Raman spectra and from Figure7.10 for THG intensity signal. 124

B.1 Characteristic scanning region of tissue. 141
B.2 Smoothing of tissue 142
B.3 Cell segmentation 142
B.4 Set threshold 143
B.5 Measure mean area of particles 143

Chapter 1

Introduction

Light was found to be useful for medical purposes quite a long time ago. Diagnostics using tissue transillumination with light has been used for breast cancer tumor detection since 1929. Medical examination and treatment methods involving light were developed and gained popularity after the invention of the first laser in 1960. Today, after more than fifty years of development, laser is used in innumerable every-day medical applications. During the recent years, medical laser techniques are developing rapidly to meet medical demands for alternative and improved methods of diagnostics as well as therapy. In this essay, a laser microscopy technique based on the nonlinear optic theory was employed [1].

Although nonlinear optics (NLO) theory was described in relatively early stage, their application as a research field started only when lasers were invented . NLO is the result of a laser beam interaction with materials and has already be proved to play a major role in the emerging photonic technology. The impact of NLO on science is widely understood and has enabled at least nine Nobel prizes in physics and chemistry [2].

In particular, in 1905 Albert Einstein proposed the idea that two photons can combine their energy to produce an excitation to the level of the sum of the two. This theory afterwards led to his nobel prize among the photoelectric phenomeno in 1921. There have been 85 years from the physical conception to the first practical biological application by Denk et al 1990 [3].

Along with this discovery and the spirit of scientific development, Maria Goppert – Mayer reported in her doctoral dissertation the quantum mechanical formulation of two- photon molecular excitation in 1931. And yet, another 30 years had to pass before bright enough lasers deliver the necessary energy to a molecule for absorption of two photons. This theoretical foundation was the chain of scientific and technology developments that led to the nonlinear optical microscopy application in several biomedical studies . Nonlinear processes are inherently ‘weak’ and many biomedical applications of nonlinear optics could not be feasible without the input of ultrashort laser pulses, microscope objectives with a high numerical aperture (NA) and high sensitivity detectors [4].

Nonlinear optical microscopy (NLOM) is an enabling technology that allows the visualization and measurement of biological processes uniquely, often with unprecedented performance. NLOM features have emerged as important techniques with ever-increasing numbers of applications in clinical medicine for diagnostics and guidance of surgery [5]. Among the various applications of nonlinear

optical imaging, its utility is the most significant in the field of preclinical and clinical cancer research [6, 7]. The information from a simple microscope is provided as a snapshot and gives qualitative information about the specimen. On the contrary, NLOM can generate three dimensional real-time images with fine sub-cellular details having a comparable resolution to confocal imaging microscope, without having to rely on exogeneous labels. Since NLOM is based on non-linear interaction of photons with the imaged sample, emission occurs only in the focal plane, resulting in reduced photobleaching and photodamage. Furthermore, the use of longer imaging wavelengths in the near infrared range by NLOM enables deeper tissue imaging. Due to these merits, NLOM is rapidly emerging as a viable non-invasive diagnostic tool for biomedical research.

Recent advancements in the field of biomedical sciences have led to an increased demand for chemical and structural information on biological materials. This essay relies on multidisciplinary research, involving physics, chemistry, biology and medicine, while embracing light based technologies, such as nonlinear optical imaging and vibrational spectroscopy to biomedicine.

The application of nonlinear optical imaging was another milestone in biological imaging, since it enabled researchers to move from cultured cells deep into tissues and whole organs, even in live animal models. Over the past years, life science interdisciplinary research has routinely used nonlinear microscopy techniques. In the present thesis, a combination of nonlinear optical modalities was applied for the production of structural maps of complex biological systems. NLOM techniques allow inspecting the assembly of single cells, tissues, and organs as well as monitoring structural and chemical changes related to cellular activation mechanisms as well as diseases.

Nonlinear optical microscopy enables stretching of the resolution limit in high scattering materials, and gives a chance to investigate inherent processes without destroying the sample. Second and Third harmonic generation signals are produced from the intrinsic properties of the sample. In the case of SHG, the signal is originated mostly from non-centrosymmetric molecules such as collagen, myosin, amylopectin and tubulin, while in the case of THG, the generated signal is due to the heterogeneities in the sample (change of the refractive index or change of third order susceptibility values) such as membranes and lipid bodies (LBs). In the case of multiphoton excitation fluorescence (MPEF), a fluorescent staining is required. However, these, alternative approaches take also advantage of endogenous fluorescent molecules, such as tryptophan, NADH, NADPH, flavins, as well as and the effects of relevant biochemical processes on their fluorescent properties.

The main objective of the present thesis was to explore the potential of label-free NLOM as a non-invasive imaging modality in diagnosis and therapy and application to clinical practice. In particular, in this essay, nonlinear optical microscopy enabled quantitative diagnosis between breast cancer and healthy cells, based on THG signals contingent on lipid structures. The results of this analysis were correlated for the first time with vibrational spectroscopy techniques (FTIR) and revealed the presence of specific chemical structures corresponding to precise membrane formations (lipid rafts).

Furthermore, this work extrapolated the study of breast cancer cells to breast cancer tissue diagnosis. NLOM discriminated successfully benign from malignant breast tissues and could grade malignancy based on the amount of LBs and inhomogeneities. The output of this analysis was further correlated with FTIR spectroscopy for obtaining chemical information. Finally, the NLOM technology was applied in the diagnosis of immune cells during inflammation. The nonlinear signals were

correlated with Raman spectroscopy and revealed that activated cells display distinct differences as to on their LB profiles.

The present research emphasizes on nonlinear microscopy modalities on different biological applications in diagnosis and therapy and the potential of this field towards clinical applications and adaptation of application-driven instrumentation. The various studies described in this thesis can be outlined as following:

Chapter 2 gives a comprehensive review concerning nonlinear optical imaging modalities, focusing on THG, SHG, MPEF optical techniques along with a general introduction to their basic theory and their applications respectively.

Chapter 3 briefly summarizes the background of molecular vibrations, which is fundamental to the understanding of vibrational spectra. In this chapter the basic principles of FT-IR and Raman techniques are being determined and the difference between IR and Raman spectroscopy is explained.

Chapter 4 describes the methods used within this thesis, the biological sample preparation and the different experimental setups. Thus, the application of nonlinear microscopy techniques, such as THG, SHG and MPEF in biomedicine, as well as various spectroscopic techniques such as FTIR and Raman spectroscopy combined with nonlinear signals for additional chemical information, are being discussed. This study examined different types of cells, including breast cancer cell lines and T cells as well as breast tissues.

Chapter 5 focuses on THG modality and it‘s capability to visualize the lipid profiles of various breast cancer cells in a non-invasive, label-free manner. The collected THG signal arises mostly from the lipid bodies and the membrane lipid bilayer. A quantitative approach of THG imaging modality was employed to offer additional information of the specimen. Quantification of THG signal indicated that it can accurately distinguish cancer cells from normal cells. Further analysis using Fourier transform infrared (FTIR) spectra was correlated to THG signal outputs for further chemical information.

Chapter 6 describes the application of nonlinear microscopy utility in a more complex environment of cells, namely in human breast cancer tissues. In particular, non-linear microscopy was applied to differentiate and categorize the different breast tissues. Herein, the main objective of this effort was to define new diagnostic tools for the recognition and grading the tumor samples using nonlinear microscopy, without the need of staining or further processing and damaging of the tissues. Quantification analysis of THG signals, based on THG area and THG intensity, successfully differentiated malignant from normal tissue samples and distinguished between the different tumor grades. Additionally, FTIR spectroscopy methods were used to obtain chemical information on the different tissues and correlated with THG signals.

Chapter 7 focuses on the development of a non invasive label free imaging technique for real time monitoring T cell activation. After studying how nonlinear microscopy could be a useful diagnostic tool in cancer, in this final chapter the possibility of using nonlinear microscopy in evaluating the effectiveness of an immunotherapy treatment was investigated. Therefore, the distinction between activated and resting T cells was examined, using THG imaging as the diagnostic tool. Qualitative and quantitative analysis showed statistically significant increase of THG mean area and THG signal intensity in activated versus resting T-cells. Different types of activation were tested. Moreover, the connection of THG imaging to chemical information (lipids, cholesterol distribution) was achieved

using Raman spectroscopy.

Chapter 8 provides an overview of the results and subsequent conclusions of the studies described in this thesis. Additionally, a brief outlook on the future use of nonlinear optical microscopy for cancer diagnostics is covered.

Bibliography

[1] Marion Jürgens et al. “Introduction to biophotonics”. In: *Handbook of Biophotonics* (2013), pp. 1–38.

[2] Elsa Garmire. “Nonlinear optics in daily life”. In: *Optics Express* 21.25 (2013), pp. 30532–30544. doi: 10.1364/OE.21.030532. url: http://www.opticsexpress.org/abstract.cfm?URI=oe-21-25-30532.

[3] W. Denk, J. H. Strickler, and W. W. Webb. “Two-photon laser scanning fluorescence microscopy”. In: *Science* 248.4951 (1990), pp. 73–6. issn: 0036-8075 (Print) 0036-8075.

[4] Barry R Masters and Peter So. *Handbook of biomedical nonlinear optical microscopy*. Oxford University Press, 2008. isbn: 0198036825.

[5] Thomas Bocklitz et al. “Non-linear multimodal imaging for disease diagnostics and treatment monitoring”. In: *International Conference on Biophotonics V*. Vol. 10340. International Society for Optics and Photonics, 2017, 103400F.

[6] J. Hou et al. “Visualization of Breast Cancer Metabolism Using Multimodal Nonlinear Optical Microscopy of Cellular Lipids and Redox State”. In: *Cancer Research* 78.10 (2018), pp. 2503–2512. issn: 0008-5472. doi: 10.1158/0008-5472.can-17-2618. url: %3CGo%20to%20ISI%3E://WOS:000432317900006.

[7] Rui Li et al. “Advances in nonlinear optical microscopy for biophotonics”. In: vol. 12. SPIE, p. 13.

Chapter 2

Nonlinear Optical Microscopy

The word “microscope” originates from the Greek words for “small” and “to view” , which describe exactly what microscopy is: viewing something small. This is achieved by magnifying the object and increasing the resolution of the image. Microscopy measurements can reveal unique molecular features of microscopic objects that are otherwise obscured by the ensemble – averaged measurements. In optical microscopy, the object is exposed to light and the transmitted, reflected, or emitted signal is analyzed.

The constant evolution of optical microscopy over the past century has been driven by the desire to improve the spatial resolution and image contrast with the goal to achieve a better characterization of smaller specimens. Nonlinear optical microscopy shares several inherent benefits compared with other optical techniques. It possesses intrinsic depth resolution due to the multiphoton nature of the process. Illumination is performed using near-infrared light, which penetrates deeper into tissue on the one hand and induces less damage on the other. Nonlinear optics has been applied to a variety of imaging tasks and has now become the technique that offers unique information without the use of staining.

In this context, nonlinear optical measurements that are used in conjunction with microscopy observation have created new opportunities. Nonlinear optical microscopy is quickly becoming a standard tool for determining the molecular mechanisms of complicated biological processes. The number of publications focused on nonlinear microscopy developments indicates that it has created its own field of research. Also, given the status of femtosecond laser advancements, it is to be expected that these techniques will be utilized for high resolution microscopy in a variety of applications. The applications of nonlinear optical microscopy as a diagnostic tool in a variety of biological samples will extensively be discussed.

The nonlinear optics studies the interaction of electromagnetic waves with atoms and molecules. In this case only the electric field will act on atoms or molecules by distorting or polarizing them. The induced polarization will follow the driving oscillating external driving field, and will build up for frequencies matching a transition in the atom or molecule (Figure 2.1 depicts the main light matter interactions).

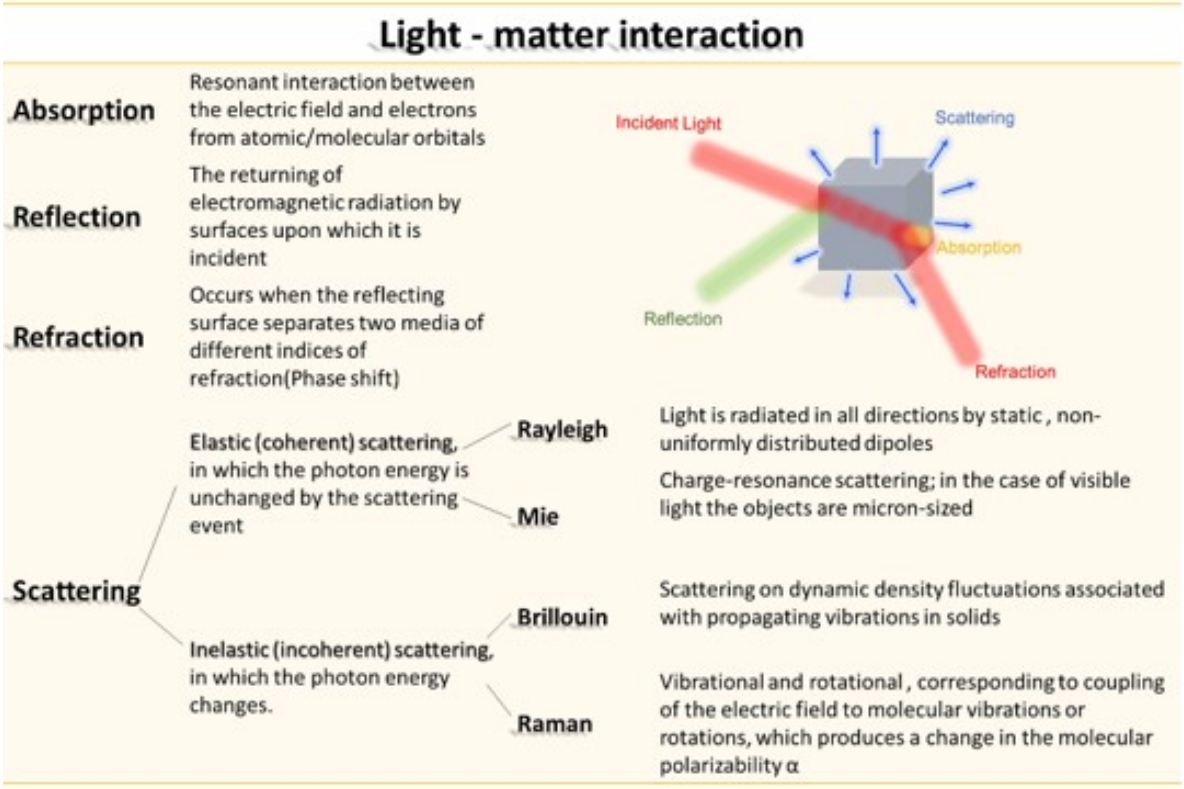

Figure 2.1: Description of the interaction of light with matter.

This chapter gives a background to nonlinear optical microscopy techniques, focusing in THG, SHG and MPEF modalities along with a general introduction to their basic theory and their applications respectively.

2.1 Nonlinear Optics Background

The term 'nonlinear' originates from the relation between a dielectric material and incoming light. Nonlinear optical phenomena occur when the response of a material to the applied optical field depends nonlinearly on the strength of the field. The applied field may cause changes in the distribution or motion of the internal electric charges such as electrons, ions, or nuclei within a molecular system, resulting in a field-induced electric dipole moment which, in turn, acts as a new source to emit a secondary wave. This is the fundamental process of optically field-induced polarization in a molecular system and re-emission of a secondary electromagnetic wave.

The induced polarization in a medium depends on the strength of the applied field and can be written as:

$$P = \varepsilon_0 \chi^{(1)} E \tag{2.1}$$

where ε_0 is the vacuum permittivity and the constant $\chi^{(1)}$ is the first-order electric susceptibility characterizing the medium. The electric susceptibility $\chi^{(1)}$ is dimensionless and indicates the ability of the electric dipoles in a dielectric environment to align themselves with the electric field. The equation

2.1 is linear, as long as the field strength E is moderate. However, if the field strength becomes too high, the oscillating charges will reach a saturated level; their response can be expressed as a power series expansion:

$$P = \varepsilon_0(\chi^{(1)}E + \chi^{(2)}E^2 + \chi^{(3)}E^3 + ...) \tag{2.2}$$

where the quantities $\chi^{(2)}$, $\chi^{(3)}$ are known as the second and third-order nonlinear electric susceptibilities, respectively. The first term describes linear absorption, scattering, and reflection of light; the second term describes SHG and optical rectification and the third term describes two– and three-photon absorption, third harmonic generation, and stimulated Raman processes such as CARs. The linear susceptibility is much larger than the nonlinear terms, which is the reason for the high intensities needed for nonlinear optical processes. The susceptibilities $\chi^{(n)}$ are bulk quantities and are related to the microscopic quantities α (polarizability), β (first order hyperpolarizability), and γ (second-order hyperpolarizability). In the case of a harmonic light wave of the form:

$$E = E_0 \sin \omega t \tag{2.3}$$

the equation 2.2, after using some trigonometric identities, can be written as:

$$P = \varepsilon_0[\chi^{(1)}E_0 \sin \omega t + \frac{\chi^{(2)}{E_0}^2}{2}(1 - \sin 2\omega t) + \frac{\chi^{(3)}{E_0}^3}{4}(3\sin \omega t + sin3\omega t) + ...] \tag{2.4}$$

As we can observe, equation 2.4 is described by an infinite sum of oscillating terms with angular frequencies that are integer multiples of ω. Specifically, the first term in equation 2.4 constitutes the linear response of the medium in the applied time-varying field. The second term is consisted of two components; the first component represents a constant quantity, which depends on the square of the field amplitude and the second component presents a dependence on the $\cos 2\omega t$ function, which shows that the angular frequency is the double of the fundamental field frequency. The double frequency as well, represents the second harmonic irradiation, which is generated. Correspondingly, the third term of equation 2.4 shows that polarization contains a component, which oscillates at an angular frequency 3ω; hence, it is responsible for the re-radiation of the incident field energy as third harmonic generation light [1, 2]. SHG is a second order process whereas THG and TPEF are both third order processes. Notably, equation 2.4 shows that the same excitation source can induce several nonlinear effects simultaneously.

The property of nonlinear harmonic generation via virtual states leaves no residual energy in the medium and the emitted photon has exactly the same amount of energy as that of the absorbed photons. The conservation of energy in such a nonlinear process provides the noninvasive property of imaging in the microscope applications of biological material.

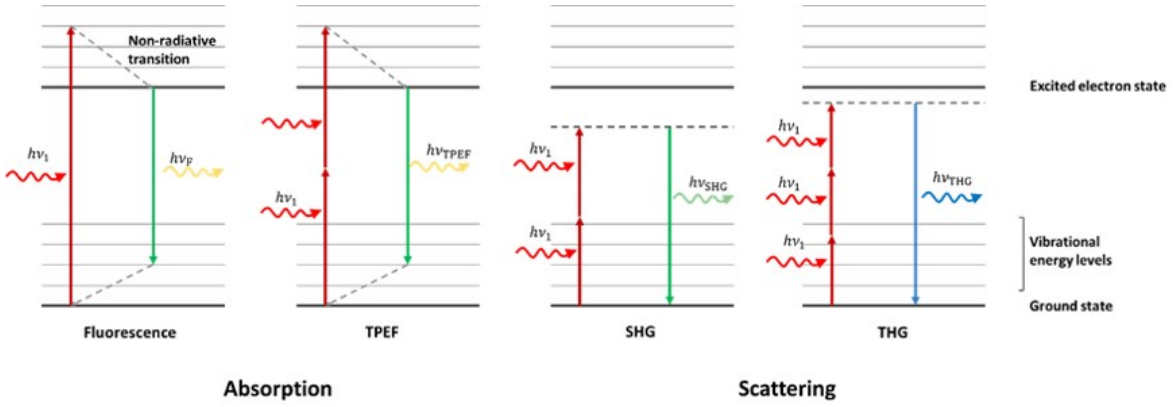

Figure 2.2: Jablonski diagram one photon fluorescence, two-photon excitation fluorescence (TPEF), second-harmonic generation (SHG) and third harmonic generation (THG). Note that in SHG and THG no actual electronic excitation takes place.

Multiphoton absorption is one of several possible nonlinear interactions. Another possibility includes optical-harmonic generation, in which two or more photons are 'simultaneously' scattered, generating a single photon of exactly twice (thrice, and so on) the incoming quantum energy (Figure 2.2). Harmonic generation requires no actual absorption but is enhanced near a resonance, albeit at the expense of parasitic absorption. It also differs from multiphoton absorption in that it is a coherent, phase-preserving process, which causes speckles, possible cancellation, predominantly forward-directed emission and supralinear dependence on the chromophore density.

However, the nonlinear polarization can efficiently produce an output signal only if a certain phase-matching condition is satisfied. Phase matching conditions and optical harmonics generation could be achieved by using birefringent materials. These materials have an index of refraction, which depends on the polarization and propagation direction of the incident light. Nevertheless, in case of biological samples harmonic generation occurs in the presence of a large wavevector mismatch, which is leading to a greatly reduced efficiency of the whole process. Nonetheless, the conversion efficiency is typically sufficient enough to produce a signal that can be detected by extremely sensitive photomultiplier devices. As a result, harmonic generation is useful as a method to study certain biological structures (e.g. collagen myosin lipids).

When the energy density at the focal spot of a microscope is sufficiently large, nonlinear optical effects such as, harmonic generation, sum-frequency generation, coherent anti-stoles Raman scattering, parametric oscillations, and multi-photon fluorescence can be observed. These optical phenomena can be used in a nonlinear optical microscope to study the biological material. Nonlinear optical microscopy may be divided into incoherent and coherent modes. Incoherent microscopy produces an optical signal whose phase is random and whose power is proportional to the concentration of radiating molecules. In this case, they produce optical signals whose phase is rigorously prescribed by a variety of factors including the excitation light phase and the geometric distribution of the radiating molecules. Fluorescence is a common example of an incoherent signal. Nonlinear versions of fluorescence microscopes are based on the simultaneous absorption of two or more photons, the most well-known being two-photon excited fluorescence (TPEF) microscopy. On the other hand coher-

ent signal power is proportional to the square of the concentration of radiating molecules. Nonlinear versions of coherent microscopy are based on the simultaneous scattering of two or more photons. Examples of such modalities include second-harmonic generation (SHG), third -harmonic generation (THG) and coherent anti-Stokes Raman scattering (CARS) microscopy.

One motivation for using nonlinear effects and in particular harmonic generation in microscopy is to provide enhanced transverse and longitudinal resolution. The resolution is enhanced because nonlinear effects are excited most efficiently only in the region of maximum intensity of a tightly focused laser beam. Microscopy based on harmonic generation also offers the advantage that the signal is far removed in frequency from the unwanted background light that results from linear scattering of the incident laser beam. For effective nonlinear harmonic generation effect, the specimen must be relatively transparent to the wavelength of fundamental illumination light usually located in the near infrared (NIR) region of the spectrum.

Near-infrared light (700–1100 nm) can penetrate biological tissues such as skin and blood cells more efficiently than visible light because these tissues scatter and absorb less light at these longer wavelengths.

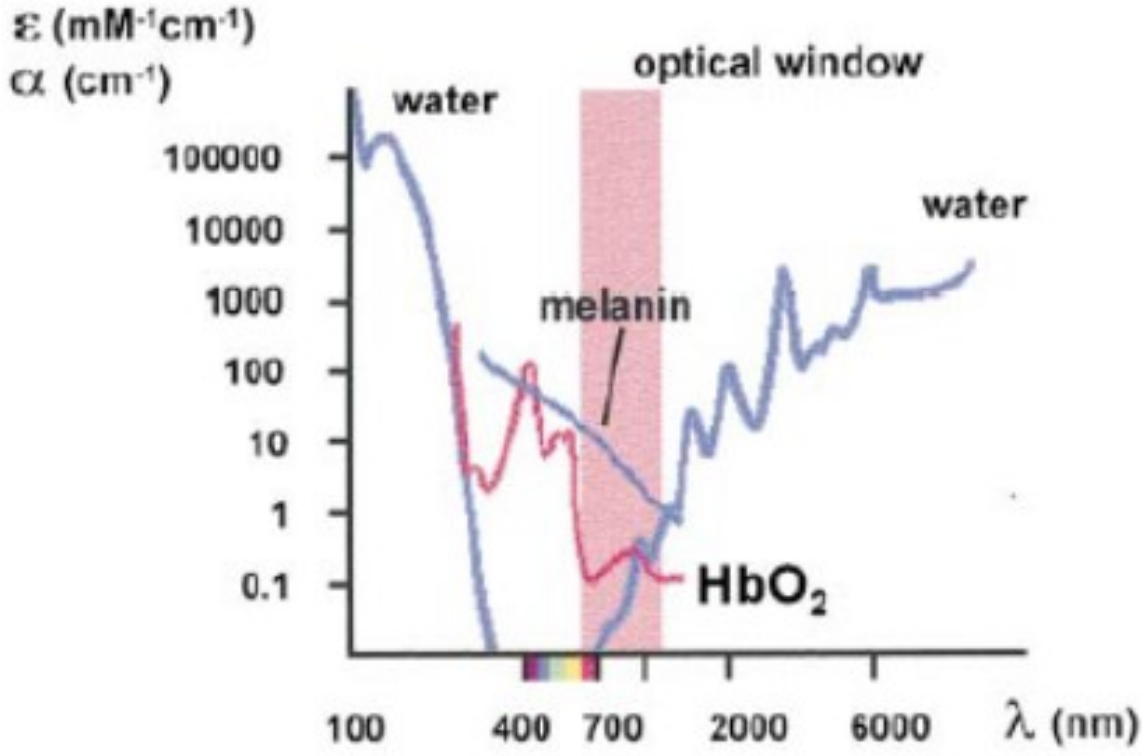

Figure 2.3: Absorption spectra of major intracellular absorbers. The molecular extinction coefficients of oxygenated haemoglobin and melanin and the absorption coefficient of water are shown. Most animal cells and tissues are considered to be nearly transparent in the spectral range from about 700 nm to 1100 nm owing to the lack of efficient one-photon absorbers.

Both scattering and absorption are wavelength dependent, and the components water, melanin and hemoglobin have low absorption coefficients for wavelengths between 700 and 1100 nm, see Figure 2.3 [3]. This spectral range is called “the optical window” as the tissue is literally an open window at

this region.

In addition, light, at a wavelength sufficiently long that it will not damage biological materials, can be used to achieve a resolution that would normally require a much shorter wavelength due to the nonlinearity. Harmonic generation microscopy can either make use of the intrinsic nonlinear response of biological materials or can be used with materials that are labeled with chromophores [1, 4].

Second and third harmonic generations (SHG and THG, respectively) and two-photon excitation fluorescence (TPEF) are currently the most widely used contrast mechanisms in nonlinear optical microscopy. The nonlinear contrast is based on second and third-order nonlinear light-matter interactions that are induced at the focus of a high numerical aperture (NA) microscope objective. Since these nonlinear optical effects are proportional to the second or third power of the fundamental light intensity, essentially, only the light at the focal plane of the optic efficiently drives the nonlinearity. This effectively eliminates out-of-focus contributions and results in the optical sectioning inherent to nonlinear imaging techniques. Therefore, it is a straightforward task to generate a sharp, two-dimensional (2D) image when nonlinear optical signals are utilized. The excitation beam is simply raster scanned across the focal plane, and the signal intensity (from the desired optical nonlinearity or nonlinearities) is measured as a function of this beam position. Extrapolation to three-dimensional (3D) images requires only one further step recording a series of these images as a function of depth by either scanning the specimen through the focal plane (stepping axially) or vice versa [5].

The combination of SHG, THG and the method of two-photon excitation laser scanning microscopy can be used for complementary information of the examining specimen. One of the advantages of the aforementioned nonlinear optical techniques is that only one illuminating source is required. In addition, the emitted signals differ significantly and can be separated to different detectors. Thereafter, a brief introduction to each of the three main contrast mechanisms used in nonlinear microscopy is discussed. Each section includes a review of the applications that have been demonstrated in biological systems. Furthermore applications of recent developed multimodal nonlinear microscopes will be mentioned.

2.2 Two Photon Excitation Fluorescence

The invention of two-photon fluorescence light microscopy by Denk, Webb and co-workers revolutionized three-dimensional (3D) in vivo imaging of cells and tissues. In 1931, the theoretical basis of two-photon excitation was established, by Maria Goppert - Mayer, and this photophysical effect was verified experimentally by Kaiser and Garret in 1963. Two-photon excitation is a fluorescence process in which a fluorophore (a molecule that fluoresces) is excited by the simultaneous absorption of two photons (Figure 2.4). The compression of the pulse and the simultaneous increase of the intensity lead to an increase the intensity of two photon excitation fluorescence. The familiar one-photon fluorescence process involves exciting a fluorophore from the electronic ground state to an excited state by a single photon. This process typically requires photons in the ultraviolet or blue/green spectral range. However, the same excitation process can be generated by the simultaneous absorption of two less energetic photons (typically in the infrared spectral range) under sufficiently intense laser illumination. This nonlinear process can occur if the sum of the energies of the two photons is greater than the energy

gap between the molecule's ground and excited states. Since this process depends on the simultaneous absorption of two infrared photons, the probability of two-photon absorption by a fluorescent molecule is a quadratic function of the excitation radiance. Under sufficiently intense excitation, three-photon and higher photon excitation is also possible and deep UV microscopy based on these processes has been developed.

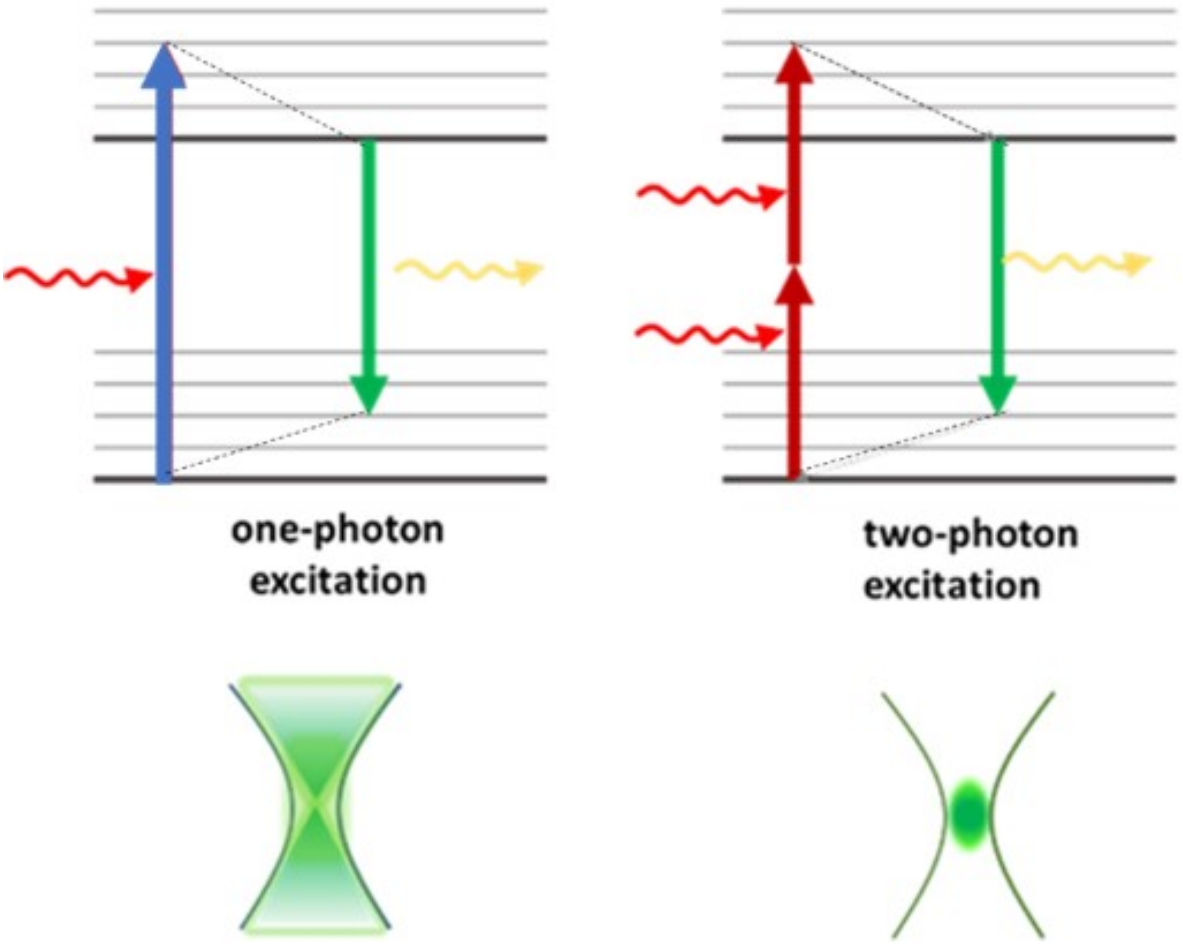

Figure 2.4: A demonstration of the localization of two-photon excitation volume. For two-photon excitation using a second objective with the same numerical aperture, fluorescence excitation occurs only from a 3D localized spot.

Although the possibility of nonlinear excitation was recognized in 1978 (Sheppard and Kompfner, 1978), two-photon microscopy was not demonstrated until 1990 [6, 7]. The investigators noted that the two-photon process could be exploited to implement microscopy imaging in three dimensions. Depth discrimination is one of the most important properties of two-photon microscopes equipped with high numerical aperture objectives. For a spatially uniform specimen, fluorescence signals are generated equally from each z-section above and below the focal plane for one-photon excitation. In contrast, over 80 % of the total fluorescence signal can be confined to a region 1 μm thick about the focal point using two-photon excitation. This depth discrimination results from the quadratic dependence of the fluorescence probability on the spatial distribution of the excitation radiance. Appreciable two-photon

fluorescence occurs only at the microscope focal volume, where the photon density is high; negligible fluorescence is excited outside of this volume (Figure 2.4).

TPEF microscopy is already widely used for characterization of biological samples [7–9], because of its many advantages compared with other microscopy methods. This optical technique offers sectioning of planes in 3-D imaging, minimizes photobleaching and photodamage, has the capability of deep imaging and can be combined with other optical modalities.

2.3 Second Harmonic Generation

As already mentioned, SHG is based on an interaction between two photons of equal energy which produces a third photon of exactly twice the energy, i.e. half the wavelength, of the incoming light 2.5.

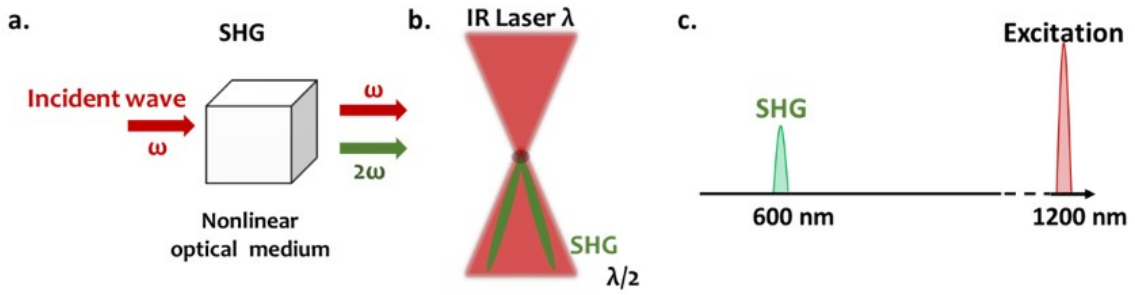

Figure 2.5: Second Harmonic generation. (a) Geometry of the interaction, (b) Spatial confinement of signal generation with nonlinear excitation (c) the wavelength description.

In Figure 2.6, two photons of frequency ω are converted into one photon of twice the frequency at 2ω. The energy levels, represented by solid lines,are atomic or molecular levels and dotted lines represent the virtual states. These virtual energy states are combined states of the molecular system and the photons of the incident radiation.

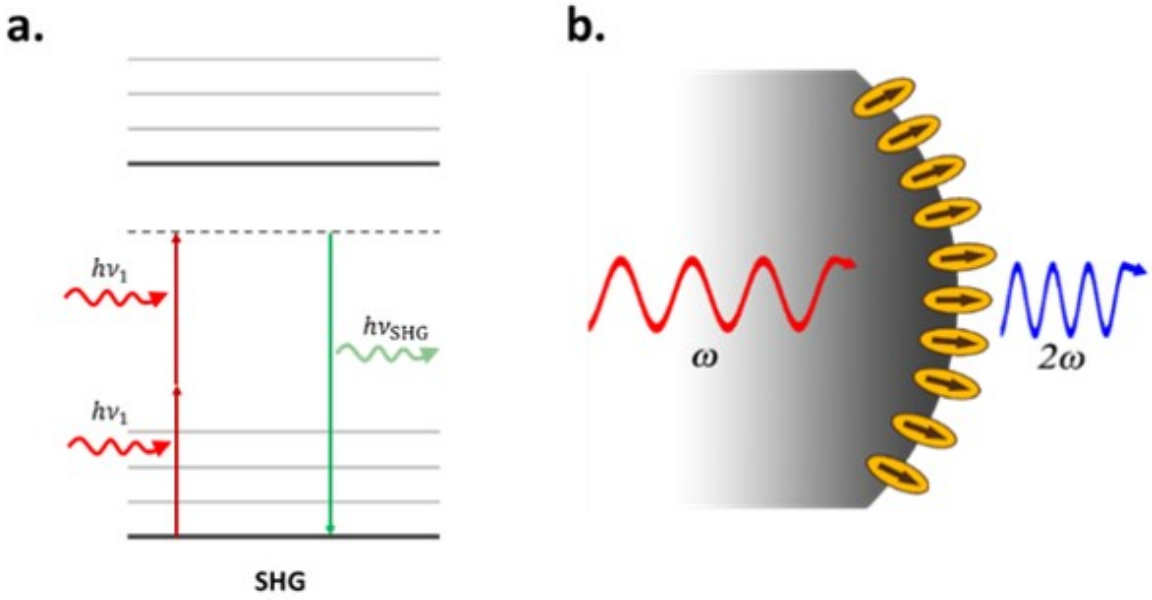

Figure 2.6: a. Energy level description of SHG b. Schematic diagram depicting ordered molecules at a small spherical surface. An ultrafast pump laser pumps light with frequency ω which generates light at 2ω from the locally non-centrosymmetric media [10]

Second-harmonic (but not third-harmonic) generation depends on the absence of inversion symmetry, which not only requires that individual molecules are inversion-asymmetric (as some biological molecules are) but also that they are spatially ordered Figure 2.6.

Since SHG is a second-order nonlinear optical process, it can arise only from media lacking a center of symmetry. This is because, if the SHG wave is a vector quantity and the induced polarization in a centrosymmetric sample (such as dye molecules in solution) were equal and opposite and vector would sum to zero. It is well known that this criterion can be satisfied at interfaces and by anisotropic crystals. This constraint can also be met by structural protein arrays because the dipole moments of the molecules align in a highly ordered fashion, and additionally, because the chirality in the helices increases the overall asymmetry of the assembly.

The intensity of Second Harmonic Generation (SHG) has the form

$$I_{SHG} = \frac{\omega_1^2[\chi^{(2)}]^2 I_1{}^2 L^2}{2n_1{}^2 n_2 \varepsilon_0 c^3} \sin c^2\left(\frac{\Delta k L}{2}\right) \tag{2.5}$$

where n_1 is the refractive index of the medium for the incident beam, c is the speed of light, $\chi^{(2)}$ is the second order susceptibility, L is the length of the interaction region, intensity of the laser beam I_1, angular frequency ω and $\Delta k = k_{2\omega} - 2k_{\omega}$ is the phase mismatch.

Conversion efficiency in SHG relates to spatiotemporal overlap of waves at fundamental and second harmonic frequencies, as well as to their group and phase velocity matching. For effective energy transfer from the fundamental wave to the second harmonic waves, both the energy ($\hbar\omega_0+\hbar\omega_0=\hbar 2\omega_0$, where $\hbar=\frac{h}{2\pi}$ with h being Planck's constant) and momentum conservation ($\hbar k_0 + \hbar k_0 = \hbar 2k_0$) must be satisfied. These two conservation requirements lead to phase matching requirement for the refractive

index of the nonlinear medium at the two frequencies as $n_{2\omega} = n_{\omega}$. For isotropic materials, this condition is not satisfied, since $n_{2\omega} > n_{\omega}$ in a normal dispersion. This condition is satisfied only for an anomalous dispersion or in a birefringent crystal Figure 2.7.

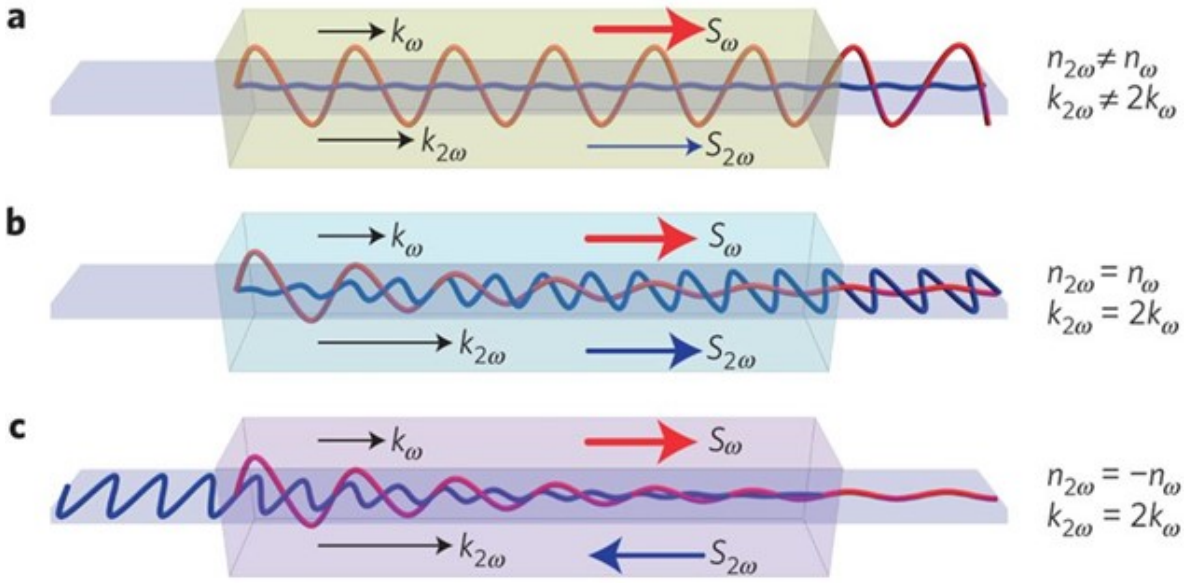

Figure 2.7: Phase matching condition for SHG. a) Low-efficiency frequency doubling of light in a positive-index medium without phase-matching ($k_{2\omega} \neq 2k_{\omega}$, $n_{2\omega} \neq n_{\omega}$). b) phase-matching for SHG ($k_{2\omega} = 2k_{\omega}$), where the fundamental and harmonic waves possess the same index of refraction. The red- and blue-colored lines in the schematics represent the fundamental and second-harmonic waves, respectively. [11]

Second harmonic generation (SHG) is produced in birefringent crystals or in biological tissues with non□centrosymmetric structure. Although theoretically predicted by Maria Göpert□Mayer in 1930s, the experimental SHG demonstration arrived with the invention of the laser in the 1960s. SHG was first obtained in ruby by using a high excitation oscillator. After that starting point, the harmonic generation reached an increasing interest and importance, based on its applications to characterize biological samples using multiphoton microscopes.

Biological SHG imaging was first reported in 1986, when Freund investigated the polarity of collagen fibers in rat tail tendon at a resolution of $\backsim$50 μm. In 2002, Mohler and Campagnola reported practical implementation of tissue imaging at high resolution and rapid data acquisition using laser scanning, and since then, SHG microscopy has been an increasingly used imaging tool [12].

Significant progress has been made in establishing SHG as a viable microscopic imaging technology for biomedical applications, both in terms of exploration of its physical principles, development of the technology, and identification of practical applications.

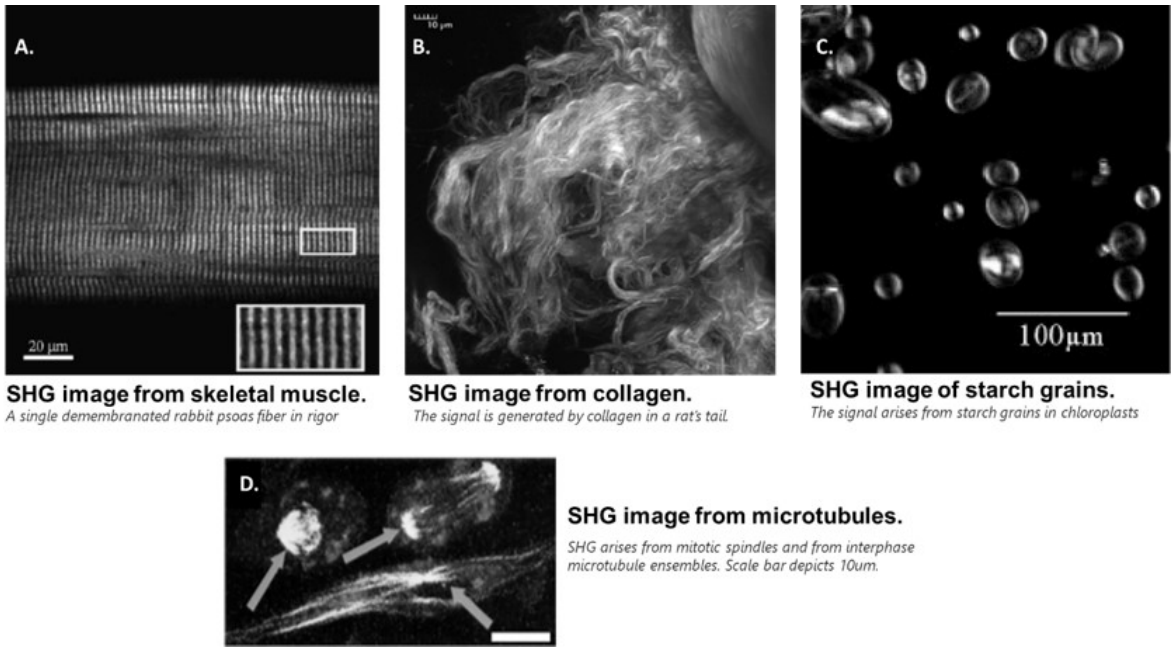

Figure 2.8: Endogenous second-harmonic-generation (SHG) imaging. (a)SHG image from skeletal muscle (b) SHG image from a mature rat tail tendon collagen (c) SHG imaging of starch grains in chloroplasts, (d)SHG arises from mitotic spindles and from interphase microtubule ensembles in red blood cells.

Many animal tissue structures can be imaged via SHG microscopy, by virtue of intrinsic contrast generated by filamentous proteins: collagen fibrils in connective tissues [13–18], tubulin [19–21], and the actomyosin lattice of muscle cells [19, 22–25] (Figure 2.8).

In addition a major characteristic of SHG signal is the dependence on the orientation, polarization, and local symmetry properties of chiral molecules [26]. Based on this capability, SHG microscopy was used for the investigation of the dependence between the incident laser beam polarization and the emitted SHG signals. Until now, an amount of studies [17, 27–29] combined nonlinear microscopy and polarization to detect changes in collagen arrangement and has been proposed to characterize collagen – based tissues. SHG intensity has been reported to exhibit structural anisotropy in type -I collagen fibers that can be characterized by the ratio of hyperpolarizabilities or polarization anisotropy $= xxx/xyy$, which provides information about the internal collagen structure.

Moreover, recent research from our group focused on polarization sensitive second harmonic generation measurements that can quantitatively discriminate aged from fresh starch based glues, used for conservation or restoration of painted artworks or papers and books of cultural heritage (see Figure 2.9) [30].

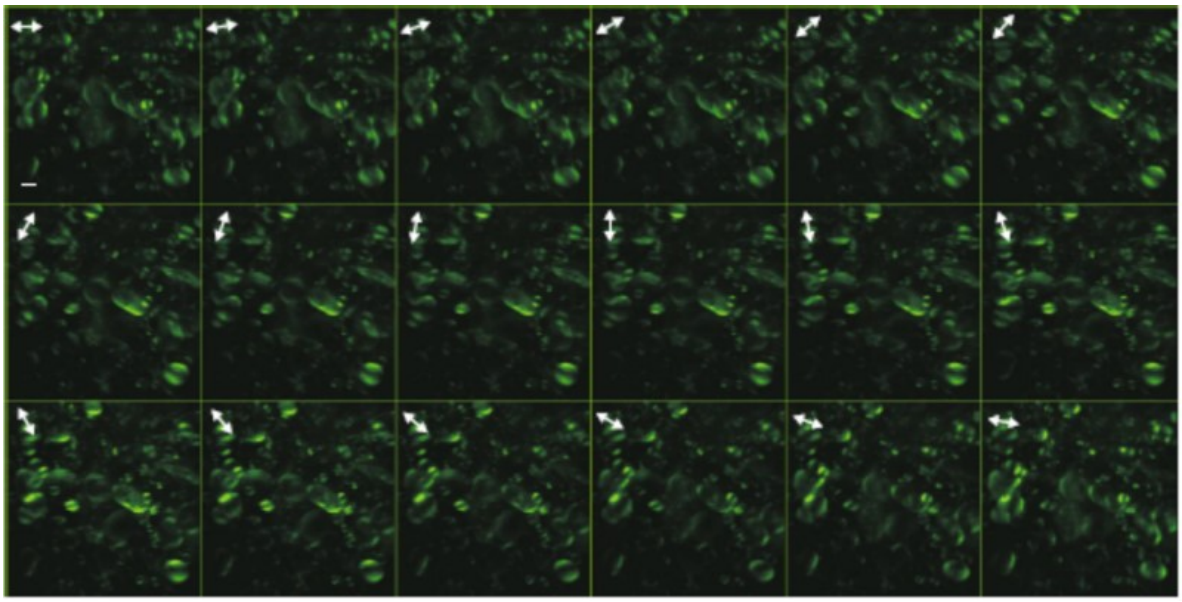

Figure 2.9: Forward detected polarization second harmonic generation imaging microscopy obtained from a fresh flour paste sample. The excitation linear polarization rotates counterclockwise between 0–170°, in steps of 10°. Arrows indicate the incident polarization. Scale bar is 10 μm.

SHG microscopy has several advantages that make it ideal for imaging tissues in situ. A particularly strong attribute is that SHG microscopy directly visualizes the tissue structure, since the contrast is produced purely from endogenous species. SHG signals arise from an induced polarization rather than from absorption, which leads to substantially reduced photobleaching and phototoxicity relative to fluorescence methods (including multiphoton). In addition, laser fundamental wavelengths typically lie in the NIR spectral range (700-1000 nm), and consequently, SHG microscopy can achieve high resolution imaging, to depths of several hundred microns.

2.4 Third Harmonic Generation

Third-harmonic generation (THG) is one of the basic nonlinear-optical processes, which have been intensely studied during the early days of nonlinear optics. In THG microscopy, third harmonic light is generated at the focal point of a tightly focused ultra-short pulsed laser beam. As already mentioned, it relies on coherent nonlinear process in which three infrared photons (typically between 900nm and 1.5μm) are coherently scattered by a molecule to produce one harmonic photon, as illustrated in Figure 2.10. Due to the coherent nature of THG, no net signal is obtained when focused inside a homogeneous, normally dispersivemedium. This is because of the Gouy phase shift, experienced by the excitation beam near the focus point, that will be explained further in this section [31–33]. However, when the nonlinear medium is not uniform, either in the refractive index or in the nonlinear susceptibility $\chi^{(3)}$, the THG signaldoes not vanish, and significant THG output can be obtained. This coherent nature of the THG process, renders THG microscopy highly sensitive to in homogeneities and the efficiency of signal generation strongly depends on the relative size of the in-homogeneity and the focal volume. This specificity makes THG microscopy useful as a tool for sub cellular biological

material characterization.

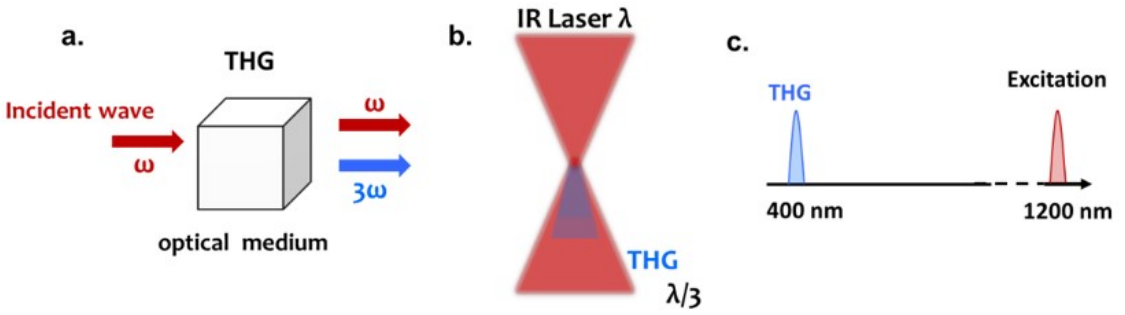

Figure 2.10: Third Harmonic generation. (a) Geometry of the interaction, (b) Spatial confinement of signal generation with nonlinear excitation and (c) the wavelength description.

In contrast to the Second Harmonic Generation (SHG), which requires a non-centrosymmetric medium, Third Harmonic Generation (THG) can appear to every kind of material. Nevertheless, the optical harmonic signal is obtained only if the phase matching condition is fulfilled, which means that the individual generated harmonic waves are added totally constructively, when the excitation light propagates through the material. It is necessary to clarify the meaning of the term phase matching, by introducing some equations. In case of a focused laser beam, the generation of harmonics can display quite different behavior. In such a situation, the peak amplitude A_N of the generated N^{th} harmonic wave is related to the peak amplitude A_1 of the fundamental wave by:

$$A_N(z) = \frac{iN\omega}{2nc}\chi^N(A_1)^N J_N(\Delta k, z_0, z) \tag{2.6}$$

where $J_N(\Delta k, z_0, z)$ represents the integral

$$J_N(\Delta k, z_0, z) = \int_{z_0}^{z} \frac{e^{(i\Delta k z')}}{1+(\frac{2iz'}{b})^{(N-1)}} dz' \tag{2.7}$$

and z_0 expresses the value of z at the entrance to the nonlinear medium, $b = \frac{2w_0^2}{\lambda_1}$ is the confocal parameter of the fundamental laser beam, and w_0 is its beam radius measured to the $\frac{1}{e}$ amplitude point.

For the case of a beam that is tightly focused into the bulk of the interaction region, the limits of integration can be replaced by $\pm\infty$, and the integral can be evaluated

$$J_N(\Delta k, z_0, z) = \begin{cases} 0, & \Delta k \leqslant 0 \\ \frac{b}{2}\frac{2\pi}{(N-2)!}(\frac{b\Delta k}{2})(N-2)e^{-\frac{\Delta k}{2}}, & \Delta k > 0 \end{cases} \tag{2.8}$$

This result shows that harmonic generation vanishes whenever $\Delta k \leqslant 0$, which, however, is the usual case of normal dispersion. The vanishing of the harmonic generation is a result of destructive interference between the contributions to the harmonic field from both sides of the beam waist.

The efficiency of THG depends mainly on the third order susceptibility $\chi^{(3)}$ of the medium and the phase – matching conditions. The total generated THG intensity by a laser beam with intensity I_1

and angular frequency ω in a medium is given by

$$I_{THG} = \frac{9\omega_1^2[\chi^{(3)}]^2 {I_1}^3 L^2}{16{n_1}^3 n_3 {\varepsilon_0}^2 c^4} \sin c^2(\frac{\Delta kL}{2}) \tag{2.9}$$

where η_1 is the refractive index of the medium for the incident beam, c is the speed of light and $\Delta k = (\frac{n_3 3\omega}{c} - 3\frac{n_1\omega)}{c}$ is the phase mismatch. In a homogeneous medium with a positive phase mismatch Δk, the term $\sin c^2(\frac{\Delta kL}{2})$ in equation 2.9 goes to zero and no THG is produced, irrespective of the magnitude of I_1 and $\chi^{(3)}$. Partial phase matching can be achieved by introducing a small inhomogeneity at the focus, resulting in a finite THG signal.

The intensity distribution is not the only change. By considering a Gaussian excitation beam, the field distribution near the focal point (Figure 2.11), also exhibits a progressive phase slippage along the optical axis z, known as the Gouy phase shift that results in an overall π radian phase difference, between a plane wave and a focused beam. The Gouy phase shift is particularly significant for THG phase matching and makes the phase matching conditions derived for a plane wave invalid, in the case of a focused beam [2].

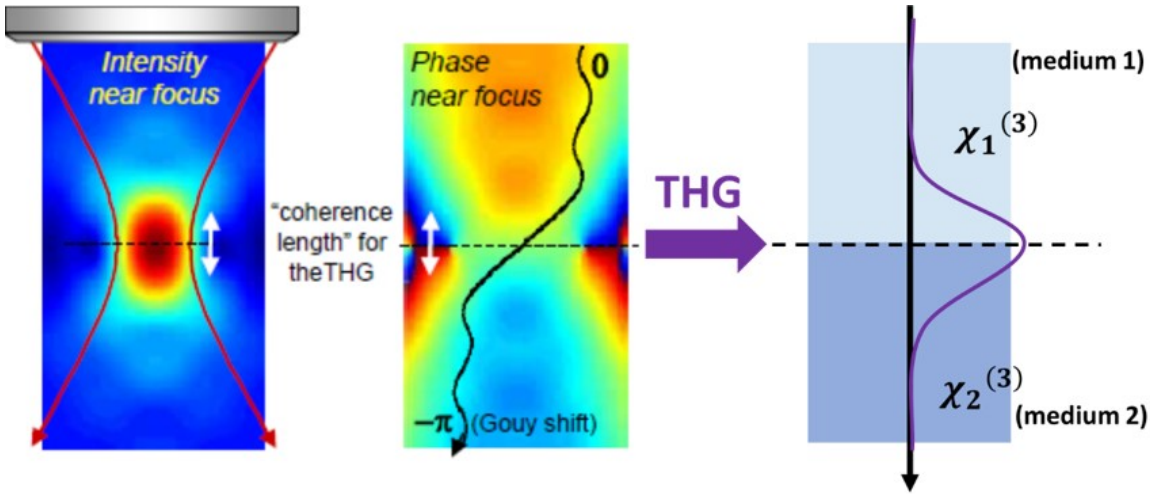

Figure 2.11: Intensity and phase distribution of a focused Gaussian beam. 2D distribution of intensity and phase near the focus.

An explanation of the signal-generation mechanism of THG microscopy was provided by Cheng at al. [34], who considered the interaction between a focused Gaussian excitation beam and a harmonic plane wave propagating along the same axis. The projection on the propagation axis of the phase difference between two beams can be expressed as

$$\Delta k = k(3\omega) - 3(k(\omega) + k_G) \tag{2.10}$$

where k_G represents the Gouy phase shift an is negative.

Consequently, the non-linear polarization will be unable to couple efficiently to the generated wave of amplitude unless a wave vector mismatch Δk is introduced to compensate for the phase shift due to passage of the incident wave through its focus. The reason why Δk should be positive, can be

understood intuitively looking at the Figure 2.12.

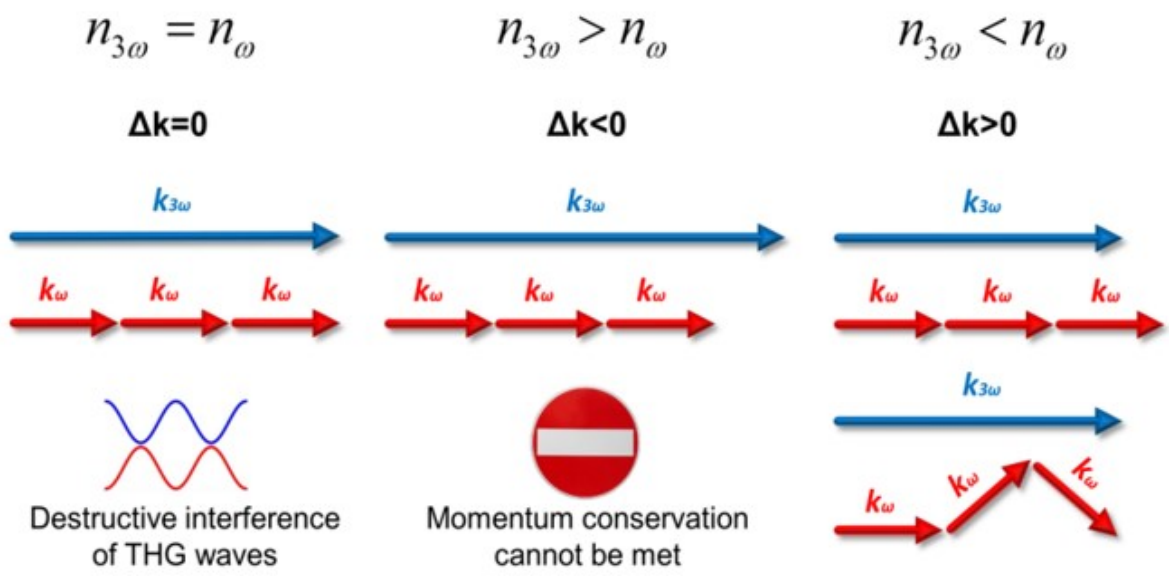

Figure 2.12: For a material presenting a perfect dispersion compensation between frequencies ω and 3ω (implying that the phase matching condition $\Delta k = 3(k(\omega) + k_G) - k_{(3\omega)} = 0$ is satisfied), the momentum conservation of the respective photons can be met. However, no signal is generated due to destructive interference of THG waves. For common normal dispersive material ($n_{3\omega} > n_{\omega}$), momentum conservation condition cannot be met in any manner; and therefore, effective THG is not possible. If $n_{3\omega} < n_{\omega}$, efficient THG can occur since the angularly spread wave vectors of the focused fundamental beam can be added effectively so that the total momentum before and after the non-linear interaction is conserved [35]

Third harmonic generation is the most closely related non-linear contrast mechanism, to SHG. Like SHG, THG is also a non-resonant, coherent process and has been used as a tool, to up-convert lasers to shorter wavelengths. Although, THG is a much weaker process as compared to SHG, it is more versatile, because it does not requires a specific asymmetry of the structure to be imaged. While both SHG and THG have been used to image membranes, they consequently do so, through different mechanisms. For example, THG probes the volume around a membrane, whereas interfacial SHG probes the two dimensional membrane itself [36]. THG signal is elicited by different types of materials, particularly phase transitions, such as water-lipid interfaces [37, 38].

During the first attempts of THG microscopy applications in biology, researchers visualized chara plant rhizoids [32]. Subsequently, laser scanning THG microscopy was utilized for demonstrating live neurons in cell culture and internal organelles in yeast cells [39]. Afterwards, the development of high power lasers, the optimization of objective lens and photomultipliers of high sensitivity, enabled numerous applications of THG microscopy in biological systems.

Specifically, THG has been used to image red blood cells [27, 40, 41], embryonic development [42–45], neurons [46], skin biopsy samples [47, 48], muscle fibers [49], collagen [50], lipid bodies [37, 38, 51], bones [52, 53] and tissues [54–56].

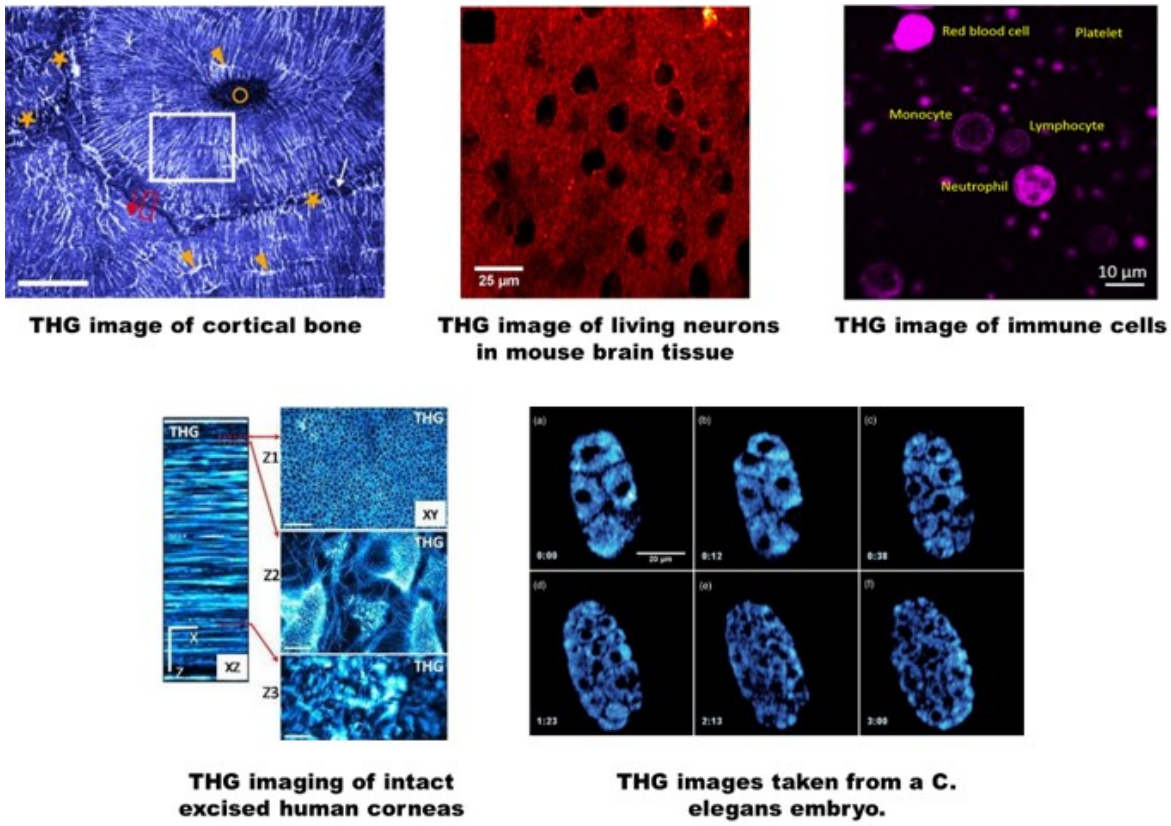

Figure 2.13: THG optical microscopy applied in different biological models.

THG microscopy has been tested to date on a variety of biological specimens (Figure 2.13). Many studies are showing that THG microscopy yields detailed images of multi-cellular and single cell specimens without any prior treatment, and with no observable damage.

2.5 Multi-contrast non-linear optical microscopes

Non-linear microscopy has made great advances during the past few years. Owing to their similarities and differences, two photon excitation fluorescence(TPEF), second and third harmonic generation (SHG and THG) imaging microscopy techniques have the potential to provide complementary information about functions and processes of several biological systems in vivo [57–59].

Multi-photon excitation fluorescence (MPEF), SHG and THG signals can be generated simultaneously from the focal spot of the biological sample providing complementary information. The development of compact, user-friendly, push-button, long term stable femtosecond laser sources, not requiring highly trained laser operators and extreme technical support, facilitates the widespread adoption of non-linear imaging microscopy for biological research. Multi-photon microscopes are now commercially available and can be easily upgraded for the detection of additional non-linear signals (SHG, THG). These optimized microscopes are flexible and easy to use systems. A single femtosecond laser beam is required for the realization of the non-linear measurements (MPEF, SHG, and THG), in contrast to other more complicated label free microscopy techniques such as CARS (two synchronized

picosecond sources, four wave mixing modality).

Recently, researchers have established intravital non-linearimaging for elucidating pathways in biological processes [50, 53, 60, 61]. The versatility of non-linear microscopy for tracking cellular events in vivo and detecting structural changes of tissues is a major enabling advance for clinical applications. Figure 2.14 depicts some applications that proved the complementarity of the different non- linear imaging modalities in various biological samples.

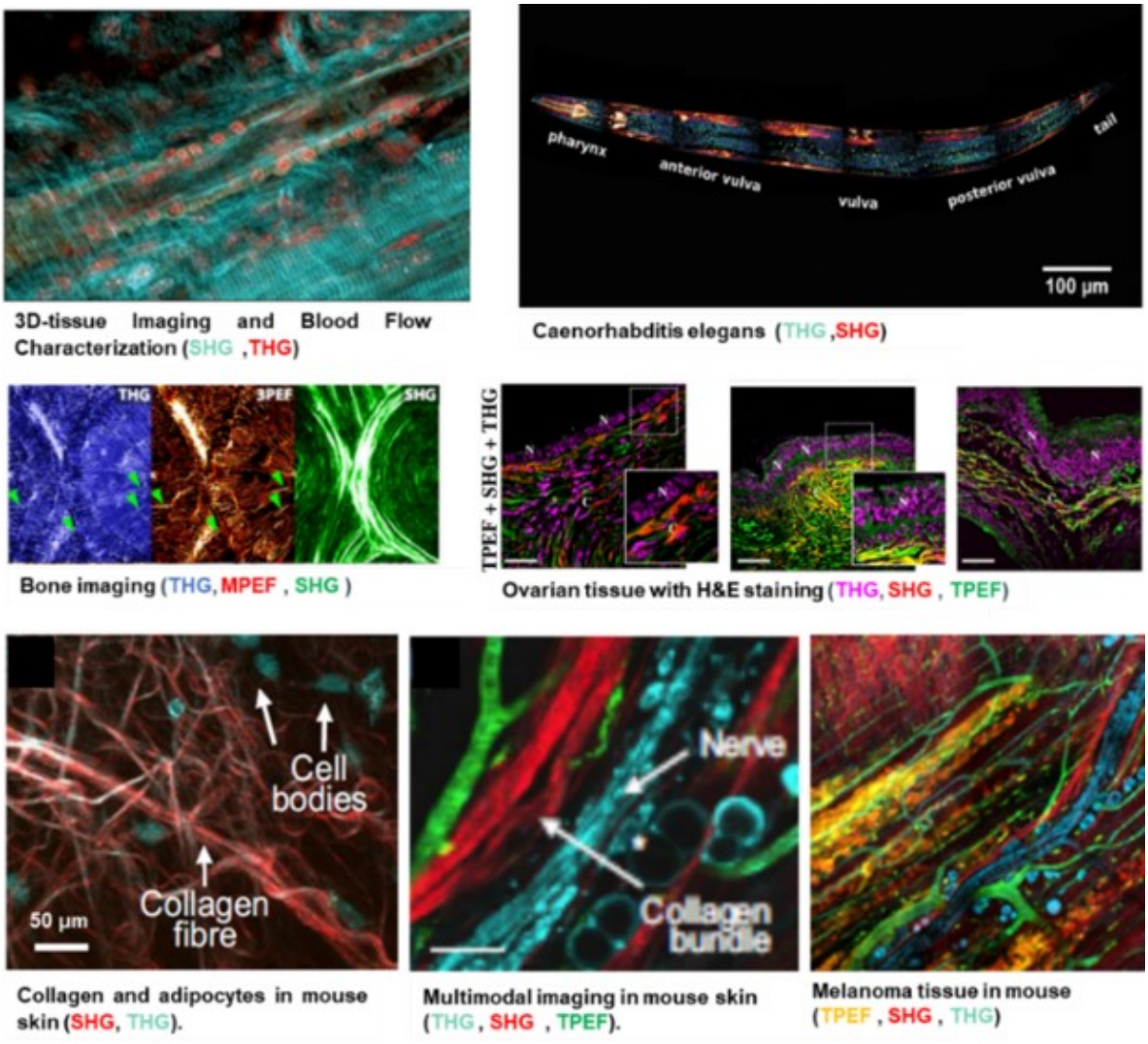

Figure 2.14: Multi-contrast non-linear imaging modalities (SHG, THG , TPEF) applied in different biological models.

Bibliography

[1] Robert W. Boyd. “Chapter 1 - The Nonlinear Optical Susceptibility”. In: *Nonlinear Optics (Third Edition)*. Ed. by Robert W. Boyd. Burlington: Academic Press, 2008, pp. 1–67. isbn: 978-0-12-369470-6. doi: https://doi.org/10.1016/B978-0-12-369470-6.00001-0. url: http://www.sciencedirect.com/science/article/pii/B9780123694706000010.

[2] Alberto Diaspro. *Optical fluorescence microscopy: from the spectral to the nano dimension*. Springer Science & Business Media, 2010. isbn: 3642151752.

[3] Karsten König. *Multiphoton Microscopy and Fluorescence Lifetime Imaging: Applications in Biology and Medicine*. Walter de Gruyter GmbH & Co KG, 2018. isbn: 3110429985.

[4] William W. Mantulin, Barry R. Masters, and Peter T. C. So. “Handbook of Biomedical Nonlinear Optical Microscopy”. In: vol. 14. SPIE, p. 3.

[5] Ramón Carriles et al. “Invited Review Article: Imaging techniques for harmonic and multiphoton absorption fluorescence microscopy”. In: *The Review of Scientific Instruments* 80.8 (2009). 002908RSI[PII] 19725639[pmid] Rev Sci Instrum, p. 081101. issn: 0034-6748 1089-7623. doi: 10.1063/1.3184828. url: http://www.ncbi.nlm.nih.gov/pmc/articles/PMC2736611/.

[6] W. Denk, J. H. Strickler, and W. W. Webb. “Two-photon laser scanning fluorescence microscopy”. In: *Science* 248.4951 (1990), pp. 73–6. issn: 0036-8075 (Print) 0036-8075.

[7] Peter So. “Two-photon Fluorescence Light Microscopy”. In: *eLS*. 2001. doi: doi:10.1038/npg.els.0002991. url: https://onlinelibrary.wiley.com/doi/abs/10.1038/npg.els.0002991.

[8] Fritjof Helmchen and Winfried Denk. “Deep tissue two-photon microscopy”. In: *Nature Methods* 2 (2005), p. 932. doi: 10.1038/nmeth818. url: http://dx.doi.org/10.1038/nmeth818.

[9] Warren R. Zipfel, Rebecca M. Williams, and Watt W. Webb. “Nonlinear magic: multiphoton microscopy in the biosciences”. In: *Nature Biotechnology* 21 (2003), p. 1369. doi: 10.1038/nbt899. url: http://dx.doi.org/10.1038/nbt899.

[10] CC BY-SA 3.0 Swk2118. Web Page. url: https://commons.wikimedia.org/w/index.php?curid=30010691.

[11] Shoufeng Lan et al. “Backward phase-matching for nonlinear optical generation in negative-index materials”. In: *Nature Materials* 14 (2015), p. 807. doi: 10.1038/nmat4324https://www.nature.com/articles/nmat4324#supplementary-information. url: http://dx.doi.org/10.1038/nmat4324.

[12] Paul Campagnola. “Second Harmonic Generation Imaging Microscopy: Applications to Diseases Diagnostics”. In: *Analytical chemistry* 83.9 (2011). 21446646[pmid] Anal Chem, pp. 3224–3231. issn: 0003-2700 1520-6882. doi: 10.1021/ac1032325. url: http://www.ncbi.nlm.nih.gov/pmc/articles/PMC3104727/.

[13] Edward Brown et al. “Dynamic imaging of collagen and its modulation in tumors in vivo using second-harmonic generation”. In: *Nature medicine* 6 (2003), p. 796. issn: 1546-170X.

[14] Guy C Cox et al. “Characterization of the second harmonic signal from collagen”. In: *Multiphoton Microscopy in the Biomedical Sciences III*. Vol. 4963. International Society for Optics and Photonics. 2003, pp. 32–41.

[15] Guy Cox. “Biological applications of second harmonic imaging”. In: *Biophysical Reviews* 3.3 (2011), p. 131. issn: 1867-2450 1867-2469. doi: 10.1007/s12551-011-0052-9. url: http://www.ncbi.nlm.nih.gov/pmc/articles/PMC5425668/.

[16] Isaac Freund, Moshe Deutsch, and Aaron Sprecher. “Connective tissue polarity. Optical second-harmonic microscopy, crossed-beam summation, and small-angle scattering in rat-tail tendon”. In: *Biophysical journal* 50.4 (1986), p. 693.

[17] Patrick Stoller et al. “Polarization-modulated second harmonic generation in collagen”. In: *Biophysical journal* 82.6 (2002), pp. 3330–3342. issn: 0006-3495.

[18] Rebecca M Williams, Warren R Zipfel, and Watt W Webb. “Interpreting second-harmonic generation images of collagen I fibrils”. In: *Biophysical journal* 88.2 (2005), pp. 1377–1386. issn: 0006-3495.

[19] Paul J Campagnola et al. “Three-dimensional high-resolution second-harmonic generation imaging of endogenous structural proteins in biological tissues”. In: *Biophysical journal* 82.1 (2002), pp. 493–508. issn: 0006-3495.

[20] Daniel A Dombeck et al. “Uniform polarity microtubule assemblies imaged in native brain tissue by second-harmonic generation microscopy”. In: *Proceedings of the National Academy of Sciences* 100.12 (2003), pp. 7081–7086. issn: 0027-8424.

[21] Alex C Kwan, Daniel A Dombeck, and Watt W Webb. “Polarized microtubule arrays in apical dendrites and axons”. In: *Proceedings of the National Academy of Sciences* 105.32 (2008), pp. 11370–11375. issn: 0027-8424.

[22] Sergey V Plotnikov et al. “Measurement of muscle disease by quantitative second-harmonic generation imaging”. In: *Journal of biomedical optics* 13.4 (2008), p. 044018. issn: 1083-3668.

[23] Sergey V Plotnikov et al. “Characterization of the myosin-based source for second-harmonic generation from muscle sarcomeres”. In: *Biophysical journal* 90.2 (2006), pp. 693–703. issn: 0006-3495.

[24] F Vanzi et al. “New techniques in linear and non-linear laser optics in muscle research”. In: *Journal of Muscle Research and Cell Motility* 27.5-7 (2006), pp. 469–479. issn: 0142-4319.

[25] V Nucciotti et al. “Probing myosin structural conformation in vivo by second-harmonic generation microscopy”. In: *Proceedings of the National Academy of Sciences* 107.17 (2010), pp. 7763–7768. issn: 0027-8424.

[26] Aikaterini Zoumi, Alvin Yeh, and Bruce J. Tromberg. “Imaging cells and extracellular matrix in vivo by using second-harmonic generation and two-photon excited fluorescence”. In: *Proceedings of the National Academy of Sciences of the United States of America* 99.17 (2002), pp. 11014–11019. doi: 10.1073/pnas.172368799. url: http://www.ncbi.nlm.nih.gov/pmc/articles/PMC123202/.

[27] Chien-Kuo Chen and Tzu-Ming Liu. “Imaging morphodynamics of human blood cells in vivo with video-rate third harmonic generation microscopy”. In: *Biomedical Optics Express* 3.11 (2012), pp. 2860–2865. issn: 2156-7085. doi: 10.1364/BOE.3.002860. url: http://www.ncbi.nlm.nih.gov/pmc/articles/PMC3493243/.

[28] V. A. Hovhannisyan et al. “Spatial orientation mapping of fibers using polarization-sensitive second harmonic generation microscopy”. In: *J Biophotonics* 5.10 (2012), pp. 768–76. issn: 1864-063x. doi: 10.1002/jbio.201100123.

[29] V. H. Le et al. “Correlation between polarization sensitive optical coherence tomography and second harmonic generation microscopy in skin”. In: *Biomed Opt Express* 6.7 (2015), pp. 2542–51. doi: 10.1364/boe.6.002542.

[30] Sotiris Psilodimitrakopoulos et al. “Polarization Second Harmonic Generation Discriminates Between Fresh and Aged Starch-Based Adhesives Used in Cultural Heritage”. In: *Microsc Microanal* 22.5 (2016), pp. 1072–1083. issn: 1431-9276. doi: 10.1017/s1431927616011570.

[31] Peter Török and Fu-Jen Kao. *Optical imaging and microscopy: techniques and advanced systems*. Vol. 87. Springer, 2007. isbn: 3540695656.

[32] Jeff A Squier et al. “Third harmonic generation microscopy”. In: *Optics express* 3.9 (1998), pp. 315–324.

[33] Max Born and Emil Wolf. *Principles of optics: electromagnetic theory of propagation, interference and diffraction of light*. Elsevier, 2013. isbn: 148310320X.

[34] Ji-Xin Cheng and X. Sunney Xie. “Green’s function formulation for third-harmonic generation microscopy”. In: *Journal of the Optical Society of America B* 19.7 (2002), pp. 1604–1610. doi: 10.1364/JOSAB.19.001604. url: http://josab.osa.org/abstract.cfm?URI=josab-19-7-1604.

[35] George J. Tserevelakis et al. “Label-Free Imaging of Lipid Depositions in C. elegans Using Third-Harmonic Generation Microscopy”. In: *PLOS ONE* 9.1 (2014), e84431. doi: 10.1371/journal.pone.0084431. url: https://doi.org/10.1371/journal.pone.0084431.

[36] Barry R Masters and Peter So. *Handbook of biomedical nonlinear optical microscopy*. Oxford University Press, 2008. isbn: 0198036825.

[37] Delphine Débarre and Emmanuel Beaurepaire. “Quantitative Characterization of Biological Liquids for Third-Harmonic Generation Microscopy”. In: *Biophysical Journal* 92.2 (2007), pp. 603–612. doi: 10.1529/biophysj.106.094946. url: http://www.ncbi.nlm.nih.gov/pmc/articles/PMC1751398/.

[38] D. Debarre et al. “Imaging lipid bodies in cells and tissues using third-harmonic generation microscopy”. In: *Nat Methods* 3.1 (2006), pp. 47–53. doi: 10.1038/nmeth813.

[39] D. Yelin and Y. Silberberg. “Laser scanning third-harmonic-generation microscopy in biology”. In: *Optics Express* 5.8 (1999), pp. 169–175. doi: 10.1364/OE.5.000169. url: http://www.opticsexpress.org/abstract.cfm?URI=oe-5-8-169.

[40] Ilyas Saytashev et al. “Multiphoton excited hemoglobin fluorescence and third harmonic generation for non-invasive microscopy of stored blood”. In: *Biomedical Optics Express* 7.9 (2016), pp. 3449–3460. issn: 2156-7085. doi: 10.1364/BOE.7.003449. url: http://www.ncbi.nlm.nih.gov/pmc/articles/PMC5030023/.

[41] Richard D. Schaller, Justin C. Johnson, and Richard J. Saykally. “Nonlinear Chemical Imaging Microscopy: Near-Field Third Harmonic Generation Imaging of Human Red Blood Cells”. In: *Analytical Chemistry* 72.21 (2000), pp. 5361–5364. issn: 0003-2700. doi: 10.1021/ac000699r. url: https://doi.org/10.1021/ac000699r.

[42] C. S. Hsieh et al. “Higher harmonic generation microscopy of in vitro cultured mammal oocytes and embryos”. In: *Opt Express* 16.15 (2008), pp. 11574–88. issn: 1094-4087.

[43] Chi-Kuang Sun et al. “Higher harmonic generation microscopy for developmental biology”. In: *Journal of Structural Biology* 147.1 (2004), pp. 19–30. issn: 1047-8477. doi: https://doi.org/10.1016/j.jsb.2003.10.017. url: http://www.sciencedirect.com/science/article/pii/S104784770300220X.

[44] Delphine Débarre, Willy Supatto, and Emmanuel Beaurepaire. "Structure sensitivity in third-harmonic generation microscopy". In: *Optics Letters* 30.16 (2005), pp. 2134–2136. doi: 10.1364/OL.30.002134. url: http://ol.osa.org/abstract.cfm?URI=ol-30-16-2134.

[45] G. J. Tserevelakis et al. "Cell tracking in live Caenorhabditis elegans embryos via third harmonic generation imaging microscopy measurements". In: *J Biomed Opt* 16.4 (2011), p. 046019. issn: 1083-3668. doi: 10.1117/1.3569615.

[46] Stefan Witte et al. "Label-free live brain imaging and targeted patching with third-harmonic generation microscopy". In: *Proceedings of the National Academy of Sciences of the United States of America* 108.15 (2011), pp. 5970–5975. doi: 10.1073/pnas.1018743108. url: http://www.ncbi.nlm.nih.gov/pmc/articles/PMC3076839/.

[47] S. Chen et al. "Virtual Biopsy of Human Skin by Using Noninvasive Higher Harmonic Generation Microscopy". In: *IEEE Journal of Selected Topics in Quantum Electronics* 16.3 (2010), pp. 478–492. issn: 1077-260X. doi: 10.1109/JSTQE.2009.2031987.

[48] S. Y. Chen, H. Y. Wu, and C. K. Sun. "In vivo harmonic generation biopsy of human skin". In: *J Biomed Opt* 14.6 (2009), p. 060505. issn: 1083-3668. doi: 10.1117/1.3269676.

[49] Markus Rehberg et al. "Label-Free 3D Visualization of Cellular and Tissue Structures in Intact Muscle with Second and Third Harmonic Generation Microscopy". In: *PLOS ONE* 6.11 (2011), e28237. doi: 10.1371/journal.pone.0028237. url: https://doi.org/10.1371/journal.pone.0028237.

[50] Bettina Weigelin, Gert-Jan Bakker, and Peter Friedl. "Intravital third harmonic generation microscopy of collective melanoma cell invasion". In: *IntraVital* 1.1 (2012), pp. 32–43. issn: null. doi: 10.4161/intv.21223. url: https://doi.org/10.4161/intv.21223.

[51] C. Kyvelidou et al. "Following the course of pre-implantation embryo patterning by non-linear microscopy". In: *J Struct Biol* 176.3 (2011), pp. 379–86. issn: 1047-8477. doi: 10.1016/j.jsb.2011.09.007.

[52] Rachel Genthial et al. "Label-free imaging of bone multiscale porosity and interfaces using third-harmonic generation microscopy". In: *Scientific Reports* 7.1 (2017), p. 3419. issn: 2045-2322. doi: 10.1038/s41598-017-03548-5. url: https://doi.org/10.1038/s41598-017-03548-5.

[53] Danielle Tokarz et al. "Intravital imaging of osteocytes in mouse calvaria using third harmonic generation microscopy". In: *PLOS ONE* 12.10 (2017), e0186846. doi: 10.1371/journal.pone.0186846. url: https://doi.org/10.1371/journal.pone.0186846.

[54] J. Adur et al. "Recognition of serous ovarian tumors in human samples by multimodal nonlinear optical microscopy". In: *J Biomed Opt* 16.9 (2011), p. 096017. issn: 1083-3668. doi: 10.1117/1.3626575.

[55] Javier Adur et al. "Optical Biomarkers of Serous and Mucinous Human Ovarian Tumor Assessed with Nonlinear Optics Microscopies". In: *PLOS ONE* 7.10 (2012), e47007. doi: 10.1371/journal.pone.0047007. url: https://doi.org/10.1371/journal.pone.0047007.

[56] Nicolas Olivier et al. "Harmonic microscopy of isotropic and anisotropic microstructure of the human cornea". In: *Optics Express* 18.5 (2010), pp. 5028–5040. doi: 10.1364/OE.18.005028. url: http://www.opticsexpress.org/abstract.cfm?URI=oe-18-5-5028.

[57] P. Friedl et al. "Biological second and third harmonic generation microscopy". In: *Curr Protoc Cell Biol* Chapter 4 (2007), Unit 4.15. issn: 1934-2616. doi: 10.1002/0471143030.cb0415s34.

[58] V. B. Pelegati et al. "Harmonic optical microscopy and fluorescence lifetime imaging platform for multimodal imaging". In: *Microsc Res Tech* 75.10 (2012), pp. 1383–94. issn: 1059-910x. doi: 10.1002/jemt.22078.

[59] Rui Li et al. “Advances in nonlinear optical microscopy for biophotonics”. In: vol. 12. SPIE, p. 13.

[60] Sixian You et al. “Intravital imaging by simultaneous label-free autofluorescence-multiharmonic microscopy”. In: *Nature Communications* 9.1 (2018), p. 2125. issn: 2041-1723. doi: 10.1038/s41467-018-04470-8. url: https://doi.org/10.1038/s41467-018-04470-8.

[61] Bettina Weigelin, Gert-Jan Bakker, and Peter Friedl. “Third harmonic generation microscopy of cells and tissue organization”. In: *Journal of Cell Science* 129.2 (2016), pp. 245–255. doi: 10.1242/jcs.152272. url: http://jcs.biologists.org/content/joces/129/2/245.full.pdf.

Chapter 3

Vibrational Spectroscopy

Spectroscopy is the study of the interaction of electromagnetic radiation with matter. When matter is energized (excited) by the application of thermal, electrical, nuclear or radiant energy, electromagnetic radiation is often emitted as the matter relaxes back to its original (ground) state. The spectrum of radiation emitted by a substance that has absorbed energy is called an emission spectrum, and the science dealing with such phenomena is appropriately called emission spectroscopy. Fluorescence spectroscopy (one or multi photon excitation) was discussed in a previous chapter.

Vibrational spectroscopy is the collective term to describe two analytical techniques: infrared (IR) and Raman spectroscopy. IR and Raman spectroscopy are non invasive tools that provide information about the molecular composition, structure and interactions within a sample. The sample spectrum is unique, like a fingerprint, and vibration spectroscopy is used for identification, characterization of structure, reaction monitoring as well as quality control and quality assurance matters [1, 2].

Due to its unique fingerprinting capability, vibrational spectroscopy plays a significant role in providing structural and mechanistic information. At present, vibrational spectroscopy is undergoing a renaissance stimulated by many new developments in infrared and Raman instrumentation, such as high sensitive low noise detectors, laser excitation sources, array detectors, step-scan technique, fiber optics, mapping and imaging in the field of microscopy, time resolved and surface enhanced methods - in order to mention some of these significant improvements. Of course this progress in vibrational spectroscopy is closely connected with the enormous development in computer science. These developments have created novel applications of IR and Raman spectroscopy in various scientific disciplines ranging from chemistry and physics to bioscience and medicine [3].

Nowadays, many analytical laboratories are equipped with an infrared (IR) and a Raman spectrometer. Raman and IR spectra provide images of molecular vibrations that complement each other and thus both spectroscopic techniques together are also known as vibrational spectroscopy. The dipole moment μ of the molecule changes as the molecule vibrates in case of IR, whereas in case of Raman active sample, the polarizability α of the molecule must change during vibration. Thus IR and Raman spectroscopies provide unique complementary information. Vibrational spectroscopy (IR and Raman) offers certain advantages over other spectroscopic techniques and are used for the determination and identification of molecular structures.

Infrared and Raman spectroscopy involve the study of the interaction of radiation with molecular

vibrations, but differ in the manner in which photon energy is transferred to the molecule by changing its vibrational state. IR spectroscopy measures transitions between molecular vibrational energy levels as a result of the absorption of mid-IR radiation. This interaction between light and matter is a resonance condition involving the electric dipole mediated transition between the vibrational energy levels. Raman spectroscopy is a two-photon inelastic light-scattering event. Here, the incident photon is of much greater energy than the vibrational quantum energy, and loses part of its energy to the molecular vibration, with the remaining energy scattered as a photon with reduced frequency. In the case of Raman spectroscopy, the interaction between light and matter is an off-resonance condition involving the Raman polarizability of the molecule. This elemental difference is shown in Figure 3.1.

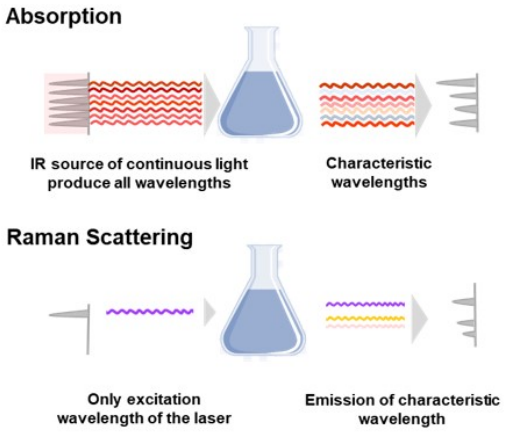

Figure 3.1: Illustration of the different vibrational methods; absorption and Raman scattering [4].

Atoms within a molecule are constrained by molecular bonds to move together in certain specified ways, called degrees of freedom that can be: electronic, translational, rotational and vibrational. In electronic motion, the electrons change energy levels or directions of spins. The translational motion is characterized by a shift of an entire molecule to a new position. The rotational motion is described as a rotation of the molecule around its center of mass. When the individual atoms within a molecule change their relative position, then we say that the molecule vibrates.

The easiest way of modelling molecular vibrations is to imagine the atoms in a molecule as spheres, and the chemical bonds connecting them as massless springs. Molecular vibrations can be excited via two physical mechanisms: the absorption of light quanta and the inelastic scattering of photons (Herzberg 1945). Direct absorption of photons is achieved by irradiation of molecules with polychromatic light that includes photons of energy, matching the energy difference h ν_k between two vibrational energy levels, the initial (i, e.g., ground state) and the final (f, e.g., first excited state) vibrational state.

$$h\nu_k = h\nu_f - h\nu_i \tag{3.1}$$

As these energy differences are in the order of 0.5 and 0.005 eV, light with wavelengths longer than 2.5 mm, that is infrared (IR) light, is sufficient to induce the vibrational transitions. Thus, vibrational spectroscopy that is based on the direct absorption of light, quanta is denoted as IR absorption or IR

spectroscopy.

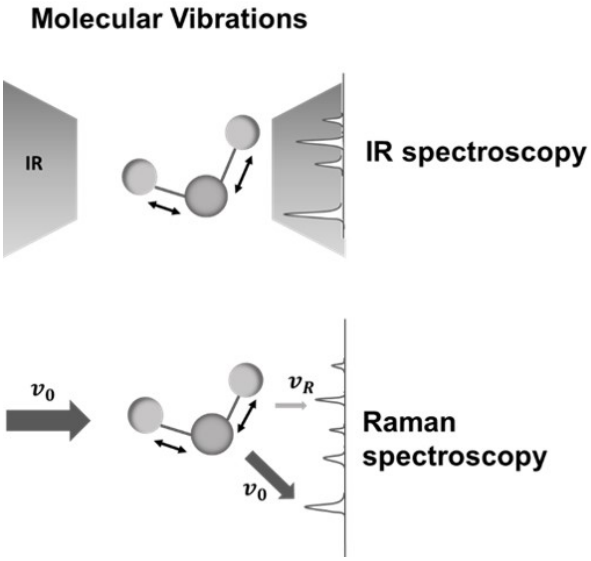

Figure 3.2: Illustration of the excitation of molecular vibrations in IR and Raman spectroscopy. In IR spectroscopy, the vibrational transitions are induced by absorption of light quanta from a continuous light source in IR spectral region. Vibrational Raman transitions correspond to inelastic scattering (ν_R scattering (ν_0) is represented by thick arrow. This is an example of SO_2 which is both IR and Raman active molecule.

In contrast to IR spectroscopy, the scattering (Raman) mechanism for exciting molecular vibrations requires monochromatic irradiation. A portion of the incident photons is scattered inelastically such that the energy of the scattered photons ($h\nu_R$) differs from that of the incident photons ($h\nu_0$). According to the law of conversation of energy, the energy difference corresponds to the energy change of the molecule, which refers to the transition between two vibrational states. Thus, the energy differences

$$h\nu_0 - h\nu_R = h\nu_f - h\nu_i \tag{3.2}$$

where $h\nu_i$ is the initial and $h\nu_f$ the final vibrational state, lie in the same range as the transitions probed by the direct absorption of mid-IR quanta, although photons of UV, visible, or near-infrared light are used to induce scattering. This inelastic scattering of photons was first discovered by the Indian scientist C. V. Raman in 1928 and is thus denoted as the Raman Effect.

The IR and Raman vibrational bands are characterized by their frequency (energy), intensity (polar character or polarizability), and band shape (environment of bonds). The frequencies of these molecular vibrations depend on the masses of the atoms, their geometric arrangement, and the strength of their chemical bonds. The spectra provide information on molecular structure, dynamics, and environment. Despite Raman and IR spectroscopy can be combined to provide complementary information of molecular vibrations, these are generally different techniques with different operations, and for this reason they will be further discussed separately in the following section.

Depending on the molecule, the same or different vibrational transitions are probed in IR and Raman spectroscopy and both techniques provide complementary information in many instances (Figure

3.2). Hence, IR and Raman spectra are usually plotted in an analogous way to facilitate comparison. The ordinate (y axis) refers to the extent of the absorbed (IR) or scattered (Raman) light. In IR absorption spectroscopy, the amount of absorbed light is expressed in units of absorbance. In contrast, Raman intensities are measured in terms of counts per second, i.e., of photons detected per second. As this value depends on many apparatus-specific parameters, in most instances only relative intensities represent physically meaningful quantities. Thus, the Raman intensity scale is typically expressed in terms of arbitrary units. The energy of the vibrational transition, expressed in terms of wavenumbers (cm^{-1}), is given on the abscissa (x axis), corresponding to the frequency of the absorbed light nabs in IR spectroscopy and to the frequency difference between the exciting and scattered light, ν_0-ν_R, in Raman spectroscopy.

The applications of vibrational spectroscopy are extremely diverse and the techniques are making a contribution to many areas of science. Perhaps the most interesting areas are in materials science and in biomedical research where the early detection of cancer is the primary goal [5]. Since various vibrational spectroscopic techniques were used for the present thesis, the basic principles of FT-IR and Raman techniques are discussed in the next section.

3.1 FT-IR spectroscopy

There is a rapid expansion in the development of new spectroscopic techniques satisfying the requirements of the increasingly more diverse studies. Infrared spectroscopy and specifically Fourier Transform Infrared (FT-IR) spectroscopy is one of the most widely used analytical technique in a whole range of fields, from biological samples to tough minerals. Today, there are large numbers of commercial FT-IR spectrometers on the market that are used for different applications of FT-IR spectroscopy, such as: quantitative analysis of complex mixtures in liquid, solid or gaseous state, determination of the quality of a sample, biological and biomedical spectroscopy etc.

A major breakthrough in IR spectroscopy was the introduction of FT-IR spectrometers, which used an instrument called interferometer that was discovered almost a century ago by Albert Michelson. At the time of the construction of the Michelson interferometer (1891), Lord Rayleigh recognized that the output from an interferometer could be converted to a spectrum using a mathematical operation that was developed by the French mathematician Fourier in the 1820s. The combination of those discoveries led to the development of a whole new technology for measuring and calculating the IR spectrum which was used in FT-IR spectrometers [6, 7].

A typical setup of Michelson interferometer requires two mirrors, an infrared light source, an infrared detector and a beamsplitter. The beamsplitter reflects about half of incident light beam while simultaneously transmitting the remaining half. One half of this split light beam travels to the interferometer's moving mirror, while the other half travels to the interferometer's stationary mirror. The two mirrors reflect both beams back to the beamsplitter, where each of the two beams is again half reflected and half transmitted. Two output beams result: one travels to the detector as the other travels to the source. When the two beams return to the beamsplitter, an interference pattern, or interferogram, is generated. This interference pattern varies with the displacement of the moving mirror, that is, with the difference in path length in the two arms of the interferometer. The interference pattern, detected

by the infrared detector as variations in the infrared energy level, is what ultimately yields spectral information (Figure 3.3).

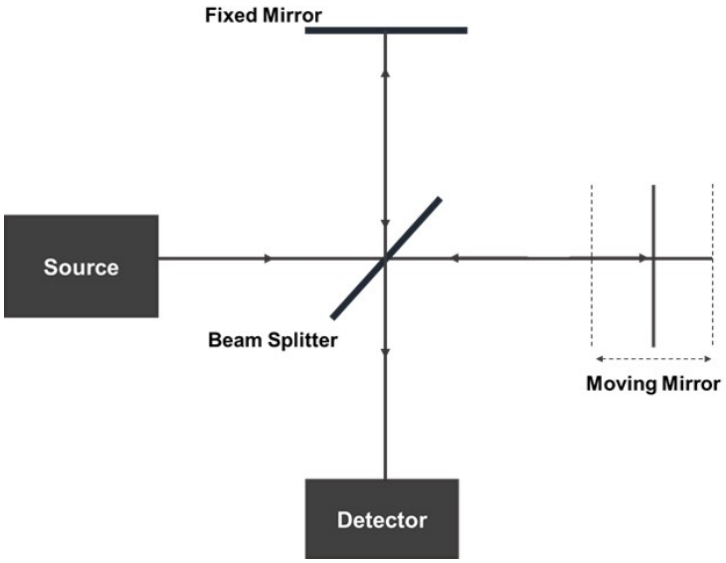

Figure 3.3: Schematic diagram of Michelson Interferometer

In contrast to Michelson interferometer that uses monochromatic source, FT-IR has infrared light source that consists of different frequency components. Each individual component contributes to the interferogram a wave with frequency inversely proportional to its wavelength. For this type of measurements it is convenient to introduce a wavenumber ν $[cm^{-1}]$ that represents the number of full waves of a particular wavelength per cm of length. When the interferogram is measured, it must be assured that the sampling intervals Δx are of equal size. For that purpose, the interference pattern of the monochromatic light of a He-Ne laser measured simultaneously with the IR interferogram is used to control the change of the retardation. The interferogram measurement starts from the point at zero retardation, where the signal has its maximum intensity and is sampled precisely at the zero crossings of the laser interferogram. In that way the accuracy of the sample spacing Δx is determined only by the precision of the laser wavelength. Once the interferogram is measured, it is transformed into a spectrum with the use of the mathematical operation known as Fourier Transform (short FT) which decomposes the measured signal (interferogram) into the frequencies that make it up.

Fourier transform infrared spectroscopy (FT-IR) is a technique that has been used over the years in chemical analysis for the identification of a variety of substances and it is now one of the techniques that may be applied to their characterization. There are many different methods of FT-IR spectrometers transmission, including attenuated total reflectance (ATR), diffuse reflectance (DRIFTs) and specular reflectance.

FT-IR spectroscopy measures absorption of IR radiation, which is related to the changes of the vibrational energy states of molecules. For a molecule to be IR active there must be a change in dipole moment μ as result of the vibration that occurs when IR radiation is absorbed. Dipole moment is a vector quantity and depends on the orientation of the molecule and the photon electric vector. The dipole moment changes as the bond expands and contracts. Absorption occurs for the vibrations that

displace the dipole along z. Dipole moment in a heteronuclear diatomic molecule can be described as uneven distribution of electron density between the atoms. One atom is more electronegative that the other and has a negative charge.

The dipole moment can be expressed as

$$\mu = er \tag{3.3}$$

The relationship between IR intensity and dipole moment is given as

$$I_R \propto (\frac{d\mu}{dQ})^2 \tag{3.4}$$

I_R is the intensity of the IR radiation, μ is the dipole moment and Q is the vibrational coordinate.

In this study, transmission and attenuated total reflectance (ATR) spectroscopy methods were used, and their brief description is following respectively. Moreover FTIR microspectroscopy was used to focus in specific areas of samples and offered high spatial resolution spectra in transmission mode.

In case of transmission methods, the measurement of radiation is expressed as transmittance or it can be easily expressed as absorbance. From the Beer- Lamperts law, transmittance (T) is the ratio of radiant power (I) transmitted by the sample to the radiant power (I_0) incident on the sample. Absorbance is the logarithm to the base 10 of the reciprocal of the transmittance.

$$A = \log_{10}(\frac{1}{T}) = -\log_{10}(T) = -\log_{10}(\frac{I}{I_0}) \tag{3.5}$$

In the reflection method the measurement of the radiation reflected from sample is

$$I = I_0 e^{-\frac{z}{d_p}} \tag{3.6}$$

where z is the distance to the optical interface and d_p is the penetration depth. The penetration depth is proportional to the wavelength and inversely proportional to the refractive index of the sample. A typical value is $d_p < 10\ \mu$m.

3.1.1 Transmission method

Transmission spectroscopy is the oldest and most straightforward infrared method. This technique is based upon the absorption of infrared radiation at specific wavelengths as it passes through a sample. It is possible to analyze samples in the liquid, solid or gaseous forms, when using this approach (Figure 3.4). An important consideration in the choice of infrared cells, where the sample is deposited, is the type of window material. The latter must be transparent to the incident infrared radiation and alkali halides are normally used in transmission methods. In our study we used KBr that is soluble in water and BaF_2 slide respectively.

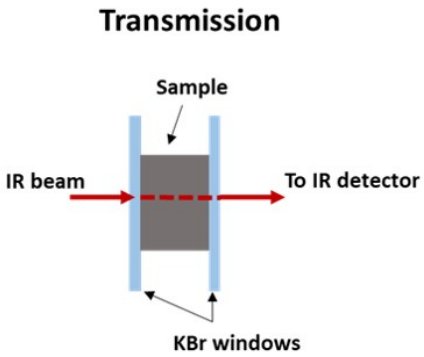

Figure 3.4: Demonstration of FT-IR spectrometers in transmission method.

3.1.2 Reflectance method ATR

Reflectance techniques may be used for samples that are difficult to analyze by the conventional transmittance methods. The most common reflectance method is an attenuated total reflectance cell in contact with the sample.

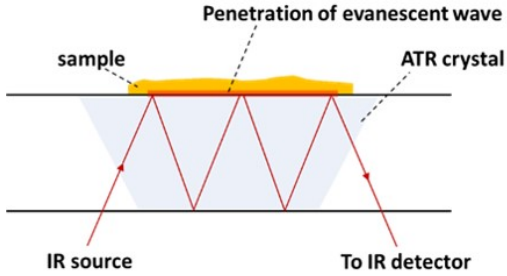

Figure 3.5: Schematic of a typical attenuated total reflectance cell. The diagram shows how the infrared light is directed into the ATR crystal, where it is totally internally reflected before passing to the detector. The sample is placed directly on top of the crystal as shown.

Attenuated total reflectance (ATR) spectroscopy utilizes the phenomenon of total internal reflection (Figure 3.5). A beam of radiation entering a crystal will undergo total internal reflection, when the angle of incidence at the interface between the sample and crystal is greater than the critical angle, where the latter is a function of the refractive indices of the two surfaces. The beam penetrates a fraction of a wavelength beyond the reflecting surface and when a material that selectively absorbs radiation is in close contact with the reflecting surface, the beam loses energy at the wavelength where the material absorbs. The resultant attenuated radiation is measured and plotted as a function of wavelength by the spectrometer and gives rise to the absorption spectral characteristics of the surface of the sample [8].

3.1.3 FT-IR microspectroscopy

FT-IR microspectroscopy combines chemical imaging with high spatial resolution and can either be mapping or imaging; mapping experiments take individual spectra sequentially across a defined region

of the sample, whilst in imaging experiments a focal plane array (FPA) detector is used to simultaneously record multiple spectra across the imaging area. High spatial resolution of 5 – 10 μm can be achieved, allowing imaging of individual cells or even organelles.

3.2 Raman spectroscopy

An alternative and complementary form of vibrational spectroscopy to IR is Raman. Raman spectroscopy is based on scattering, rather than absorption, of photons as is the case for IR spectroscopy. Raman scattering is inelastic scattering. The phenomenon of inelastic scattering of light was first postulated by Smekal in 1923 and first observed experimentally in 1928 by Raman and Krishnan. Since then, the phenomenon has been referred to as Raman spectroscopy. In the original experiment, sunlight was focused by a telescope onto a sample which was either a purified liquid or a dust-free vapor. A second lens was placed by the sample to collect the scattered radiation. A system of optical filters was used to show the existence of scattered radiation with an altered frequency from the incident light – the basic characteristic of Raman spectroscopy [9–12].

Raman spectroscopy differs principally from IR spectroscopy in that it is based on the scattering of photons by molecules, rather than on the absorption of photons. When a molecule is positioned in a electric field $\vec{E}$ an electric dipole is induced

$$\vec{p} = \alpha\vec{E} \tag{3.7}$$

where α is the polarizability. This quantity, which is actually α tensor, varies with time as it describes the response of the electron distribution to the movements of the nuclei that oscillate with the normal mode frequency ν. Polarizability indicates how easily the charge distribution of a molecule can be distorted.

If a molecule is interacting with an electromagnetic wave with the electric field vector oscillating with the frequency ν_0

$$\vec{E} = \vec{E}_0 \cos(2\pi\nu_0 t) \tag{3.8}$$

The oscillating electric field can induce a dipole in the molecule, and equation 3.7 can be simply expressed as

$$\vec{p}(\nu) = \vec{p}_1(\nu_0) + \vec{p}_2(\nu_0 - \nu) + \vec{p}_3(\nu + \nu_0) \tag{3.9}$$

The sum on the right side includes three terms corresponding to polarizabilities that depend on different frequencies, which are the frequency of the incident radiation ν0 and the frequencies (ν_0-ν) and (ν+ν_0) that differ from (ν_0) by the frequency on the normal mode. Scattering that leaves the frequency of the incident light unchanged is referred to as elastic or Rayleigh scattering, whereas the frequency shifted (inelastic) scattering is referred to as Raman scattering (Figure 3.6). When the frequency of the scattered light is lower than (ν_0), the molecule remains in a higher vibrationally excited state m > n for the transition n → m. This process is denoted as Stokes scattering, whereas anti-Stokes

scattering refers to ($\nu+\nu_0$) and thus to m < n. At ambient temperature, thermal energy is lower than the energies of most of the normal modes, such that molecules predominantly exist in the vibrational ground state and Stokes scattering represents the most important case of Raman scattering [13].

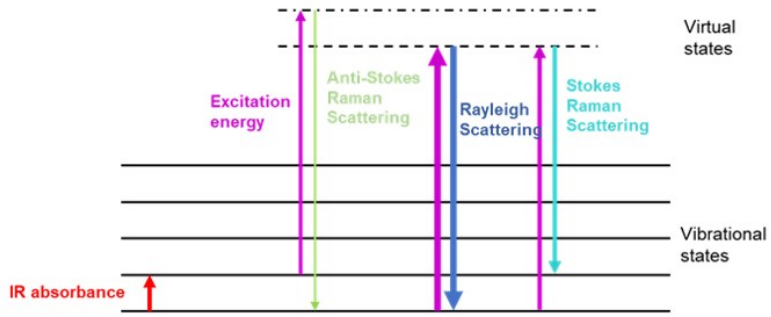

Figure 3.6: Energy diagram representing the elastic Rayleigh scattering and the inelastic anti-Stokes and Stokes Raman scattering.

Incident light interacts with molecules causing transitions to higher virtual energy levels. In non-resonant Raman, the frequency of the excitation light is such that a molecule is excited to an unstable virtual energy level and quickly re-emits the photon. Resonant Raman is a special case in which the excitation frequency is much closer to that of a molecular electronic transition. Relaxation occurs by emission of light of the same frequency as the incident light (elastic scattering), or of higher or lower frequency (inelastic scattering). If the light emitted is of a lower frequency the molecule returns to a higher energy level than the initial state, this is Stokes scattering. Anti-Stokes scattering occurs when the emitted light is higher frequency than the incident light, because the molecule returns to a lower energy level than the initial state.

Although the basis of Raman spectroscopy has similarities to IR spectroscopy, the information produced is complementary due to different selection rules. This often results in normal vibrations that are strong in Raman being weak in IR, and vice versa.

Incident light in Raman spectroscopy is typically laser light in the visible, UV or near-IR region. The use of near-IR wavelengths reduces the inherent fluorescence that is usually present and can mask the weak Raman signals of interest. The light source of a Raman spectrometer is in general a laser with a specific wavelength. The laser's wavelength can range from the ultraviolet to the visible and near-Infrared range depending on the application. The light beam is focused on a dichroic filter. The filter reflects the light beam to the sample at a right angle. The resulting Raman scattering is focused back to the dichroic filter. Usually, It serves as a band□stop filter whereby the incident light from the light source is nearly completely attenuated. Only light with a different wavelength, i.e. Raman scattered light can pass the filter unaltered. The measured light is redirected by mirrors to a monochromator, which uses grating to diffract the beam into a narrow band of wavelengths (analyze the light). The photo current from each wavelength section is then measured at the detector. In general, a sensitive CCD detector (charged-coupled device) is used to convert the measured photo current into electric current. Finally, the measured data can be saved and evaluated on a computer by using appropriate software (Figure 3.7).

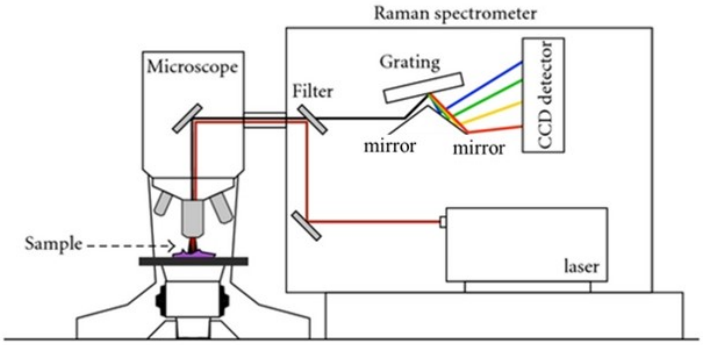

Figure 3.7: Typical setup for a Raman spectrometer with a laser attached to a microscope [14].

In Raman spectra, the intensity of measured Raman scattering is plotted versus the Raman shift. The Raman shift is defined as difference between the measured frequency of scattered light and incident light beam. Hence, Raman spectra are independent of the wavelength of the light source. However, instead of using the wavelength, the Raman shift is given as change of the wavenumber n (cm^{-1}) which is inversely proportional to the wavelength. Intensities of Raman spectra are $\backsim$0.001 % of laser intensity and therefore the detection of Raman spectra is more difficult than IR. Intensity of Raman peak depends on the polarizability of the molecule, the intensity of the laser and the concentration of the active group.

$$I_{Raman} \propto P_{laser} {\nu_0}^4 \alpha^2 \tag{3.10}$$

A major advantage of Raman in biology is that water is a poor scatterer and does not have a strong signal in Raman spectra, in contrast to its strong bands in IR spectra. However, inelastic light scattering in non-resonant Raman is a rare event so Raman signals are very weak in comparison to absorbance signals. Resonant Raman generally produces stronger signals than non-resonant Raman, but the interference from the simultaneously collected high fluorescence signals becomes more of a problem. Figure 8 depicts an example of Raman spectra of T cells.

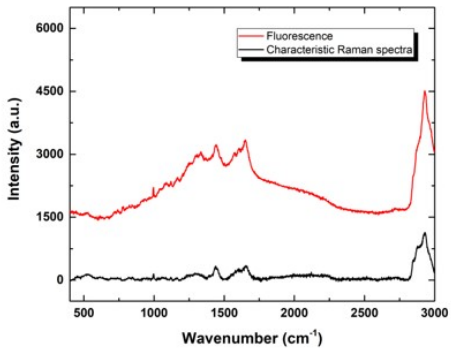

Figure 3.8: An example of Raman spectra of a sample where interfere fluorescence (red) and normal Raman spectra (black) are shown for comparison.

Bibliography

[1] Dixit N Sathyanarayana. *Vibrational spectroscopy: theory and applications*. New Age International, 2015. isbn: 8122415172.

[2] Edgar Bright Wilson, John Courtney Decius, and Paul C Cross. *Molecular vibrations: the theory of infrared and Raman vibrational spectra*. Courier Corporation, 1980. isbn: 048663941X.

[3] Alan Campion. "Infrared and Raman Spectroscopy of Biological Materials. Practical Spectroscopy Series. Volume 24 Edited by Hans-Ulrich Gremlich (Novartis Pharma AG, Basel, Switzerland) and Bing Yan (ChemRx Advanced Technologies, Inc., South San Francisco, California). Marcel Dekker: New York and Basel. 2001. xii + 582 pp.195.00. ISBN 0-8247-0409-6". In: *Journal of the American Chemical Society* 123.42 (2001), pp. 10427–10427. issn: 0002-7863. doi: 10.1021/ja004845m. url: https://doi.org/10.1021/ja004845m.

[4] Hana VAŠKOVÁ. "A powerful tool for material identification: Raman spectroscopy." In: *International Journal of Mathematical Models and Methods in Applied Sciences* 5.7 (2011), pp. 1205–1212. issn: 1998-0140. url: http://www.naun.org/main/NAUN/ijmmas/17-120.pdf.

[5] Hans-Ulrich Gremlich and Bing Yan. *Infrared and Raman spectroscopy of biological materials*. CRC Press, 2000. isbn: 1482290057.

[6] Peter R Griffiths and James A De Haseth. *Fourier transform infrared spectrometry*. Vol. 171. John Wiley & Sons, 2007. isbn: 0470106298.

[7] Peter Larkin. *Infrared and Raman spectroscopy: principles and spectral interpretation*. Elsevier, 2017. isbn: 0128042095.

[8] Barbara Stuart. *Infrared spectroscopy : fundamentals and applications*. (Barbara H.) Includes bibliographical references (pages [205]-209) and index. Chichester, West Sussex, England ; Hoboken, NJ : J. Wiley, [2004] ©2004, 2004. url: https://search.library.wisc.edu/catalog/999974109102121.

[9] Norman Colthup. *Introduction to infrared and Raman spectroscopy*. Elsevier, 2012.

[10] Richard C Lord. "Introduction to Infrared and Raman Spectroscopy". In: *Journal of the American Chemical Society* 87.5 (1965), pp. 1155–1156. issn: 0002-7863.

[11] Ewen Smith and Geoffrey Dent. *Modern Raman spectroscopy: a practical approach*. John Wiley & Sons, 2013. isbn: 1118681320.

[12] John R Ferraro. *Introductory raman spectroscopy*. Elsevier, 2003. isbn: 0080509126.

[13] Peter Hildebrandt F. Siebert. "Theory of Infrared Absorption and Raman Spectroscopy". In: *Vibrational Spectroscopy in Life Science*. 2008. url: https://onlinelibrary.wiley.com/doi/abs/10.1002/9783527621347.ch2.

[14] Michael B. Fenn et al. "Raman Spectroscopy for Clinical Oncology". In: *Advances in Optical Technologies* 2011 (2011), p. 20. doi: 10.1155/2011/213783. url: http://dx.doi.org/10.1155/2011/213783.

Chapter 4

Methods

This chapter presents the methods used within this thesis and describes the biological sample preparation and the different experimental setups. This thesis accomplished an interdisciplinary study of chemistry, biology, medicine and physics. Specifically this essay focused on the application of non-linear microscopy techniques, such as THG, SHG and MPEF in biomedicine. Moreover, various spectroscopic techniques such as FTIR and Raman spectroscopy were combined with non-linear signals for additional chemical information. This study examined different type of cells, such as breast cancer cell lines and T cells and breast tissues as well.

4.1 Biological sample preparation

4.1.1 T cells

The biological sample was prepared in the immunology lab of Prof. Irene Athanassakis in the Biology Department at the University of Crete. The samples were prepared and provided from Dr. Ioanna Zerva. In this research, the activation of mouse T-cells was achieved either with the use of Concanavalin-A (Con-A), or with human serum antigen (HSA). Concanavalin-A was used a mitogen, while HSA was used as specific antigen. The T-cells were stained with the selected antibodies and either activated with Con-A, or placed in co-culture with macrophages activated with HSA.

However, the problem that had to be faced in this set of experiments was the morphological similarity between T-and B-cells, which are both present in the spleen cell preparation used in these studies. Normally, flow cytometry testing is used for specific lymphocyte population counts. For this reason, a fluorescence staining procedure was used for the distinction-isolation of the two cell types (Figure 4.1).

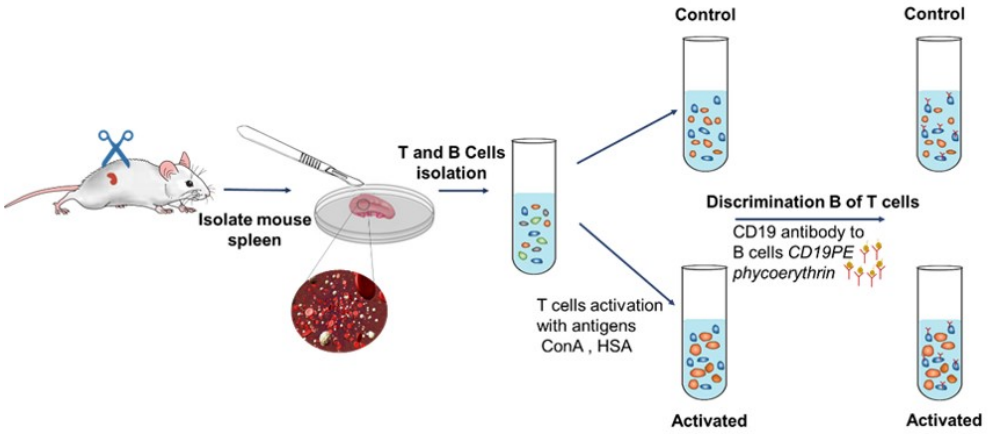

Figure 4.1: Cells preparation for the performance of the non-linear imaging measurements.

Animals BALB/c inbred mice were purchased from Charles River (Milan, Italy) and bred in the animal facility of the Department of Biology at the University of Crete (Crete, Greece, EL91-BIObr-09) under standard conditions of temperature (18-25 °C), humidity (45-50%) and photoperiod of 12h light and 12h dark. Males and females 4-8 weeks of age were handled according to the international and national bioethical rules and conformed to the bioethics regulations following the EU Directive 2010/63/EU for animal experiments. Mice were sacrificed by cervical dislocation and spleens were removed under antiseptic conditions.

Cell cultures Spleen cells were cultured for 24 h in 10 mm petri dishes (Sarstedt, Numbrecht, Germany) at the concentration of 1x106 cells/ ml in DMEM culture medium (Biosera, Kansas City, USA) supplemented with 10% fetal bovine serum (FBS, Biosera) at a final volume of 10 ml. Upon elimination of adherent cells, the remaining cells were washed twice in HBSS (Biosera) and submitted to a mitogenic or antigenic stimulus. For the mitogenic stimulus, non-adherent cells were re- plated at the concentration of 1×10^6 cells/ ml in DMEM-FCS culture medium in the presence of 10 μg/ml concanavalin-A (Con A, Sigma, Germany). For the antigenic stimulus, non-adherent cells were co-cultured with antigen activated macrophages. To this extend, macrophages were incubated with 1 μg/ml human serum antigen (HSA, Sigma) for 24 h, and after antigen elimination and washing with DMEM-FCS, 1×10^6 lymphocytes/ ml were added to the cultures.

T cell processing Two days after culture or co-culture initiation the non-adherent cells consisting of B and T lymphocytes were submitted to immunostaining or purification procedures in order to be able to distinguish T from B lymphocytes for application in the non-linear optical microscopy or isolate T cells for Raman spectroscopy, respectively. Thus, upon culture termination, the cells were fixed with 4% paraformaldehyde, washed and reacted with anti-mouse CD19-PE conjugated monoclonal antibody (Immunotools, Friesoythe, Germany), which specifically recognizes B lymphocytes and can be easily detected by TPEF measurements. In another set of experiments, upon culture termination, T cells were magnetically isolated by negative selection using a rat anti-mouse CD45R antibody. Thus, the cells were reacted with 1 μg/ml rat anti-mouse CD45R (surface marker of B cells, EurobioSciences,

Germany) in PBS-BSA 0.1% for 40min. After washing the cells were incubated with Dynabeads M-280 Sheep anti-Rat IgG (Invitrogen, Life Technologies AS, Norway) for 30min with gentle stirring and applied to a magnet for negative T cell selection and processing for Raman spectroscopy.

4.1.2 Breast cancer cell lines

The biological sample was prepared in the laboratory of Translational Oncology at medical school of University of Crete, cooperating with Prof. Agelaki Sofia and Prof. Vassilils Georgoulias. The preparation of cells was accomplished by Mrs. Haris Markomanolaki. Luminal (T47D, MCF7), Her2+ (BT474, SKBR3) and triple negative (MDA-MB231, Hs578t) human breast cancer cell lines were purchased from ATCC (Rockville, Maryland, USA) and maintained at 37 °C in a humidified atmosphere of 5% CO_2 in air. MDA-MB231 and Hs578t cell lines were cultured in DMEM medium (GIBCO 61965-026, Grand Island, NY) supplemented with 10% FBS (GIBCO-BRL) and 50 μg/mL penicillin/streptomycin (GIBCO-BRL). For MCF7 and T47D cell cultures, the above medium was supplemented with 16 ng/mL and 11ng/mL insulin, respectively. SKBR3 cells were cultured in McCoy's medium (GIBCO-BRL) supplemented with 10% FBS and 50mg/mL penicillin/ streptomycin. BT474 cells were cultured in DMEM/Ham's F12 medium (GIBCO-BRL) supplemented with 10% FBS, 2mM L-glutamine (GIBCO-BRL), 1mM sodium pyruvate (GIBCO-BRL) and 50mg/mL penicillin/streptomycin. For sub-cultivation cells were detached using 0.25% trypsin and 5mmol/L EDTA (GIBCO-BRL). All experiments were carried out during the logarithmic growth phase. The passage number remained stable for all cell lines. Non- tumorigenic MCF10a human breast cells were cultured in DMEM/Ham's F12 medium supplemented with 5% horse serum (GIBCO), 50mg/mL penicillin/ streptomycin, 100μL EGF, 250μl hydrocortisone, 50 μl cholera toxin, and 16ng/mL insulin.

Peripheral blood mononuclear cells (PBMCs) were isolated from healthy blood donors (n=3). Peripheral blood (10 ml) was placed on a Ficoll-Hypaque density gradient (d = 1,077 g/mol) and upon centrifugation at 1800 rpm for 30 minutes, PBMCs were collected from the interface and washed three times with PBS by centrifugation at 1500 rpm for 10 minutes.

For lipid droplet staining, cells were fixed with PFA 4% (Sigma- Aldrich Co., MO, USA, 158127), permeabilized with PBS-Triton X-100 0.025% (Sigma, X100) and stained with Nile Red (10μg/ml, Sigma, N3013).

SEM analysis SEM images obtained with the kindly help Mrs. A. Siakouli at Biology Department of UOC. Upon culture termination, samples were washed with 0.1 M sodium cacodylate buffer (SCB) and then incubated in the same solution for 15 min, twice. Samples were fixed using a 2% glutaraldehyde, 2% formaldehyde in SCB fixative buffer for 1 h at 4 °C. All surfaces were then washed twice (from 15 min per time) with SCB 0.1M at 4 °C, dehydrated using serially graded ethanol immersions (from 30, 50, 70, 90 to 100%) and incubated for 15 min in dry 100% ethanol twice. The samples were then critical point dried (Bal-Tec CPD 030). Prior to electron microscopy examination the samples were mounted on appropriate stubs and sputter coated (Bal-Tec SCD 050) with a 10 nm gold layer. SEM analysis was processed with a JEOL JSM 6390LV Scanning Electron Microscope operated at 15KV and for high definition analysis a JEOL FESEM 7000F field emission scanning electron microscope

with an acceleration voltage of 15 kV.

4.1.3 Breast Tissues

Tissue samples were prepared by Prof. Maria Tzardi group in the pathological anatomy lab of medical school of University of Crete.

Patients Control healthy and cancerous tissues were obtained from different patients (Table 4.2). The number of patients was 15. Tissue cancer C3 and control 1 was from the same patient, a normal and cancerous region of breast tissue. Moreover, cancer A4 and B3 were from the same patient with different grades of tumor. All tissues tested herein were provided from the University Hospital at Heraklion, Crete and their use was approved by the Ethical Committee of the Institution.

Breast Tissue		
Name	**Subtype**	**Grade**
Cancer A1	ER(+)/PR(+)	Grade I
Cancer A2	ER(+)/PR(+)	
Cancer A3	ER(+)/PR(+)	
Cancer A4	ER(+)/PR(+)	
Cancer B1	ER(+)/PR(-)	Grade II
Cancer B2	ER(+)/PR(-)	
Cancer B3	ER(+)/PR(-)	
Cancer B4	ER(+)/PR(+)	
Cancer B5	ER(+)/PR(+)	
Cancer C1	ER(+)/PR(+)	Grade III
Cancer C2	ER(+)/PR(+)	
Cancer C3	ER(+)/PR(-)	
Cancer C4	ER(-)/PR(-)	
Control 1	-	Normal
Control 2	-	

Figure 4.2: Tissues included in the present research

Tissue processing Tissue samples were embedded in paraffin, sliced in 5 μm-thick histological sections and routinely stained with hematoxylin and eosin (H&E) for optical microscopy examination. For THG imaging, serial tissue slices were placed on special very thin (0.07mm) round glass microscope

slides of 3.5cm diameter to provide a flat sample surface.

4.2 Experimental Setups

This thesis was performed in the nonlinear microscopy lab (NLM) of Dr. George Filippidis at IESL-FORTH. A custom-made nonlinear optical microscope was used as the main setup in this thesis and was coupled with spectrometers (Raman, FT-IR in Dr George Kenanakis's lab) to obtain complementary information of the samples. Raman spectroscopy was used for additional information during T cell measurements, while FT-IR spectroscopy was used for breast cancer cell lines and breast tissues, respectively.

4.2.1 Nonlinear Microscope

The experimental apparatus consisted of an Yb-based femtosecond (fs) laser oscillator emitting at a central wavelength of 1028nm (Amplitude Systemes, t-pulse, 200fs, 50MHz, 1Watt) combined with a modified upright microscope (Nikon Eclipse ME600D) (Figure 4.3).

Adjustable neutral density filters (New Focus) were utilized to control the power at the sample plane. The laser beam passes through mirrors and is directed on a pair of galvanometric mirrors (Cambridge Technologies). Galvanometric mirrors were employed in order to perform the fast raster scanning in the selected xy plane of the sample. The focal plane was adjusted by using a motorized translation stage (Standa Ltd. 1μm minimum step). A telescope system was used to expand the beam diameter in order to fill the back aperture of the objective lens. The beam was tightly focused on the sample by employing a high Numerical Aperture (NA) objective lens (Carl Zeiss, C-Achroplan 32x, NA 0.85, water immersion). By employing diffraction limited focused fs laser beams, nonlinear phenomena at the sample plane of the biological specimens could be created. Using such setup it was possible to collect simultaneously two different nonlinear signals, one in the transmission (THG) and the other in the reflection mode (TPEF) or (SHG) by adjusting the suitable filter, providing thus the opportunity to perform co-localization measurements. On the transmission mode THG signal was recorded, after passing through a condenser lens (Carl Zeiss, PlanNeofluar, 40x, 0.75 NA, air immersion) and a coloured glass filter (U 340-Hoya), from a photo multiplier tube (PMT, Hamamatsu H9305-04). On the reflection mode, TPEF or SHG signals were detected by using a second PMT (Hamamatsu, R4220) by employing an appropriate short pass filter ,(SPF 700nm, CVI) or bandpass interference filter (CVI 514 nm) respectively.

A computer controlled both scanning and data acquisition procedures. The samples were placed between two very thin round glasses (70 μm, Marienfeld) separated by a copper spacer (100 μm thickness) to avoid damage the cells. A CCD camera (PixeLINK) was used for the optical observation of our specimens.

The alignment and the optimization of the system performed via the collection of the maximum THG signals from the air/glass and glass/air interfaces from a coverslip. The maximum intensity of the THG signals emitted from the cells were always one order of magnitude lower in comparison with the ones detected from the glass/air interface of the second coverslip, which used to hold the sample.

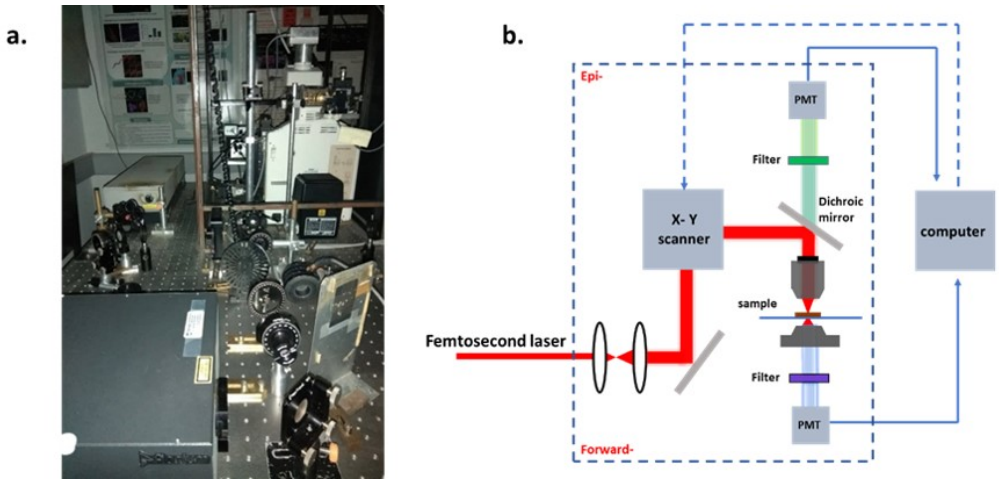

Figure 4.3: Nonlinear optical setup photograph (a) and the schematic diagram (b)

For all the studies presented herein, the laser power on the sample plane was adjusted at 38 mW. The described setup scanned 500x500 pixels THG and TPEF or SHG image around in one (1) second. The lateral (radial) resolution of this system was almost $\sim 0.6 \mu$m and the axial resolution was around 2 μm. A critical component to create nonlinear phenomena at the focal plane was to achieve high intensities by employing tightly focused fs laser beams. The energy per pulse is the average power divided by the repetition rate and was calculated to be around 0.77 nJ. The peak power is the energy per pulse divided by the pulse width and in the experiments presened here, it was around 4kW. Moreover, the peak intensity at focal plane was around 242 GW/cm^2, the power density 2.3 MW/cm^2 and the fluence 46mJ/cm^2. In case of breast cancer cell lines and breast tissues studies the images had resolution 11.111 pixels/μm. For imaging T cells, which represented a smaller sample for observation, the resolution was adjusted to 18.52 pixels/μm. To improve the signal to noise ratio (SNR), 20 scans were averaged for each final image. To further improve image quality, a series of 2D optical sections were obtained at 1μm intervals (z stack) and projected (maximum intensity projection) onto a single plane. Image J software was used for data viewing and processing (NIH,).

4.2.2 Raman Spectrometer

Raman measurements were performed at room temperature using a commercial Horiba LabRAM HR Evolution confocal micro-spectrometer, in backscattering geometry (180 °), equipped with an air-cooled solid state laser operating at 532 nm with 100mW output power (Figure 4.4). The laser beam was focused on the samples using a 50x Olympus microscope objective (NA= 0.50), providing a $\sim$18mW power on each sample. Raman spectra over the 300-3200 cm^{-1} wavenumber range (with an exposure time of 20 sec and 5 accumulations) were collected by a Peltier cooled CCD (1024 x 256 pixels) detector at -60 °C, with a resolution better than 1 cm^{-1}, achieved using a 600 grooves/mm grating and an 800 mm focal length.

Figure 4.4: Horiba LabRAM HR Raman setup

Test measurements were carried out using different optical configurations, exposure timings, beam power and accumulations, in order to obtain sufficiently informative spectra using a confocal hole of 100μm, but ensuring to avoid alteration of the biological sample. The high spatial resolution of the system allowed us to carefully verify that cells remained intact after irradiation. The Raman shift was calibrated automatically using LabSpec 6 software (Horiba) using zero order line and Si line of a Si reference sample (520.7 cm^{-1}). The acquired spectra were compared with scientific published data and reference databases, such as Horiba LabSpec 6 (Horiba). For observation, T cells were mounted on CaF_2 coverslips. To remove the autofluorescence, baseline correction was implemented to the recorded spectra.

4.2.3 FTIR spectrometer

Breast cancer cells were deposited on IR transparent KBr windows (approximately 20 μl with 10^4-10^5 cells). FTIR experiments were carried out using a Bruker Vertex 70v commercial spectrometer equipped with a KBr beamsplitter and a room temperature broad band triglycine sulfate (DTGS) detector in absorption mode (Fig4.5). Interferograms were collected at 4 cm^{-1} resolution (8 scans), apodized with a Blackman-Harris function, and Fourier transformed with two levels of zero filling, in order to yield spectra encoded at 2 cm^{-1} intervals. Before scanning, KBr background was recorded and each sample spectrum was obtained by automatic subtraction of the background.

Correspondingly, breast tissues were mounted on BaF_2 coverslips, bearing a width of 1cm. The collected spectra were set at region 3500-750 cm^{-1} wavenumbers. For the breast tissue study, FT-IR microspectroscopy in absorption mode, Attenuated Total Reflectance (ATR) spectroscopy and FTIR analysis in absorption mode was used. FTIR microspectroscpy was utilized in absorption mode, where the beam was focused with objective lens (15x, N.A 1.2) and N_2 was used for the detectors. In ATR spectroscopy, crystal was adjusted to be in touch with the tissue and collect surface chemical information at room temperature. Moreover, for each tissue, FTIR measurements in transmission mode were performed at room temperature and covered the whole tissue region. However, the obtained information of this utility was limited.

Figure 4.5: FT-IR experimental setup - Bruker Vertex 70v spectrometer

The spectra were processed by using the software supplied by the instrument manufacturer (OPUS software package; Bruker Optics, Germany). The FTIR spectra along with their first and second derivative curves were used to highlight the components of different spectral regions and to determine the approximate values of the peak positions of the components. This data processing allowed the estimation of the concentration of the corresponding chemical bonds.

4.3 Data analysis

4.3.1 Signal's mean total area calculation

All the samples were imaged under constant irradiation conditions (mean energy per pulse, linear polarization of the incident beam at the sample plane, dimensions of the scanning region, number of pixels, amplification of the PMT units). THG intensity values were collected from the photomultipliers' tubes (PMTs), stored in 2D 500 by 500 matrices and represented a single slice image of the sample. Image J software was used for image processing and thresholding. THG signal quantification was performed by setting a constant threshold in the obtained normalized 8-bit slice images, so that regions generating high levels of nonlinear signal were solely detected and isolated. The threshold was set to allow only the percentage of the THG signal of the sample area to be analyzed and measured. The obtained calculated area corresponded mainly to the cellular membrane, the nucleus membrane and the lipid droplets of each cell.

4.3.2 Signal's intensity calculation

For the quantification of the mean THG intensity, the values of a number of N cells were firstly normalized to a standard THG intensity value. Then the values were quantified by setting again a constant threshold, so that only the regions that provide high THG signals could be examined (mainly intra cellular lipid droplets, cellular and nucleus membranes). An algorithm designed and programmed in MATLAB environment was employed for the selection of representative cell areas of each slice and

estimation of their mean pixel value. The integrated THG intensity over the total pixel area for each slice of a sample was calculated by multiplying the representative area with the mean intensity value of the corresponding pixels. The weighted mean pixel value of each specimen was obtained by repeating this procedure for the representative slices of each sample.

4.3.3 Statistical analysis

For multi group comparisons, one-way analysis of variance (ANOVA) with a post hoc Tukey test was used. Data were analyzed with SPSS 16.0 software.

Chapter 5

Distinction between breast cancer cell subtypes using third harmonic generation microscopy

The objective of this chapter focuses on THG modality and it‘s capability to non-invasive, label-free, visualization of the lipid profiles of various breast cancer cells. The collected THG signal arises mostly from the lipid droplets and the membrane lipid bilayer. A quantitative approach of THG modality was employed to offer additional information of the constitution of the specimen. Quantification of THG signal indicated that it can accurately distinguish cancer from normal cells. Further analysis using Fourier transform infrared (FTIR) spectra was performed correlating THG imaging to chemical information.

5.1 Breast cancer

Cancer refers to any one of a large number of diseases characterized by the development of abnormal cells that divide uncontrollably and have the ability to infiltrate and destroy normal body tissue. Cancer is caused by changes (mutations) to the DNA within cells. DNA is packaged into a large number of individual genes, each of which contains a set of instructions telling the cell what functions to perform, as well as how to grow and divide. Errors in the instructions can cause the cell to stop its normal function and may allow a cell to become cancerous. Cancer is one of the leading causes of death worldwide. But survival rates are improving for many types of cancer, thanks to improvements in cancer screening and cancer treatment.

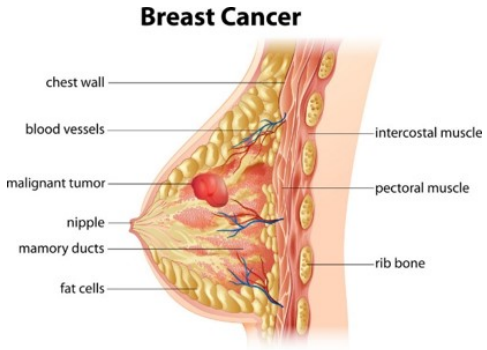

Figure 5.1: Illustration of the different vibrational methods; absorption and Raman scattering [1].

Breast cancer (Figure 5.1) is now the leading cause of cancer in women worldwide and the most common cause of cancer-related deaths. It occurs when cells in the breast start to grow out of proportion and invade neighboring tissues or spread throughout the body. According to the world health organization (WHO) more than 1.6 million women per year are diagnosed with breast cancer. It is estimated that 1 in 8 women worldwide will be diagnosed with breast cancer at some point in their life. Specifically, in Greece 6000 new cases are reported with breast cancer each year.

Breast cancer is not a modern illness. To the contrary this type of cancer has probably been around as long as the human race. It is not surprising that written records and illustrations of breast cancer date back to antiquity, since the location of the organ permitted easy identification. The Edwin Smith Surgical Papyrus, dating back to 3,000–2,500 B.C., and possibly attributable to Imhotep (the Egyptian physician-architect), provides authentic accounts of breast cancer. A case was deemed incurable, if the disease was “cool to touch, bulging and spread all over the breast”. In ancient Greece, a divinity was exhorted to offer relief from breast maladies, as evidenced by votive offerings in the shape of breasts in Greek temples that housed Asclepius, the god of medicine. Carcinoma (karkinoma), scirrhous (hard, Greek skirros) and cacoethes (malignant disease, Greek kakoethes) in the medical lexicon owe their origins to Hellenistic writings. Hippocrates’ theory in c. 400 B.C. of the imbalance of humours (blood, phlegm, and yellow and black bile) as a cause of disease, and his classic descriptions of the progressive stages of breast cancer, represent early hypotheses on the cause of cancer [2].

Until now, breast cancer affects a large portion of the global population and constitutes a substantial public health burden, for this reason it has generated a considerable amount of research interest. Breast cancer often characterized by a lack of early symptoms, which results in late detection of the disease. Detection at advanced stages of the disease implies that the treatment is more difficult and uncertain. The appropriate screening methods could help for significant early breast cancer detection.

As with most cancers, early diagnosis of the disease radically increases survivorship. Consequently, researchers have had the laborious task of increasing the accuracy and precision of their diagnoses. The last two decades have witnessed significant developments in breast cancer detection and diagnosis. Imaging plays a major role in the diagnosis, treatment, and follow-up of breast cancer. While imaging tests, such as X-rays, are helpful in detecting masses or areas of abnormality, they alone can’t differentiate cancerous cells from noncancerous cells. For the majority of cancers, the only way to make a definitive diagnosis is to perform a biopsy to collect cells for closer examination.

Breast cancer is a heterogeneous disease with multiple subtypes, variable size, grade, metastatic potential and with varying prognosis. Hence, the choice of therapy for patients with breast cancer is to some extent defined by information provided by the pathological assessment. Diagnostic testing involves tests and procedures to confirm the presence of disease and identify the correct tumor type, location, extent and stage. The examination of the standard haematoxylin and eosin (H&E)-stained section is still an efficient, cost-effective and powerful mode of providing information to inform classification and hence clinical management . The pathological subtype (e.g. tubular versus metaplastic), grade (1 versus 3), size, vascular permeation and nodal status will provide informative data to define the likeliest outcome for patients with breast cancer and the need for adjuvant systemic therapies. Nonetheless, developments in our understanding of the molecular and cellular basis of cancer initiation and progression are providing tools for refining the taxonomy of breast cancer and opening up new avenues for the classification and treatment of breast cancer.

However, the standard histopathology of breast tissue, the primary means of disease diagnosis, involves manual microscopic examination of stained tissue by a pathologist. Because this method relies on qualitative information, it can result in inter-observer variation. Furthermore, for difficult cases the pathologist often needs additional markers of malignancy to help in making a diagnosis. A wide variety of tumor markers viz. uPA, BRCA1 & 2, Ki76, ER, PR, HER etc. are used for establishing the type of breast carcinoma. However, each marker has its own prognostic value and not all breast cancer patients have the same clinical picture. Though proposed, only few markers are used in clinical practice and research studies are still ongoing to identify and establish new biochemical parameters/ markers. However, these biomarkers for disease detection and monitoring are time-consuming and complicated processes. In this thesis, we proposed nonlinear imaging modalities as a new label free non-invasive method for detection of breast cancer.

The majority of breast cancer research is conducted using established breast cancer cell lines as in vitro models. Breast cancer cell lines are likely to reflect, to a large extend, the features of cancer in vivo. As will be presented in the present thesis, the application of nonlinear microscopy modality may be used for the accurate distinction between cancer and control cells.

5.2 THG microscopy as diagnostic tool for breast cancer cell lines

Early detection is one of the most important strategies to improve survival of breast cancer patients. New techniques in imaging, tissue diagnosis and cytobiological assessments are being developed, and promise to improve early detection and identify potentially high risk women suffering from the disease [3]. Emerging techniques using the analysis of tumor cells show promising results in predicting and identifying breast cancer in patients. Specifically, the establishment of robust detection techniques the last years shifted the interest towards the circulating tumor cells that are detected in blood of breast cancer patients. During metastasis, the first step is the dissemination of cancer cells in the blood (when cancer cells detach from the primary tumor and intravasate), while micrometastasis in a distant organ, like the bone marrow, reflects a more advanced stage. The early detection of circulating breast cancer cells by morphologic methods is currently being challenged by multiple methods [4, 5]. Molecular detection methods suggested a prognostic impact of circulating cancer cells in early breast cancer pa-

tients. Moreover, researchers employed cytological approaches (e.g. CellSearch) to detect circulating cancer cells but did not report a significant prognostic impact [6].

In this essay, we proposed nonlinear microscopy modalities as a first approach for detection and discrimination of cancer cells during breast cancer. To achieve that, we employed human breast cancer cell lines and compared them to human peripheral blood mononuclear cells (PBMCs) .

Non linear optical imaging has taken a rapid progress in the biomedical field. The past decade non linear imaging techniques proved relevant in the research of life sciences studies, revealing valuable and complementary information about the specimen under investigation [7–14]. The efficiency to investigate in vivo cellular and subcellular activities, without any damage of the biological specimen, and provide valuable information have made non linear imaging techniques a perfect tool for early diagnosis and treatment of several diseases.

These techniques are increasingly promising for clinical diagnostics and the monitoring of serious diseases, as they can probe the biological sample with high resolution. During the last decade non linear optical techniques have been used as diagnostic tools for cancer research. Chang et al., developed lipid-enclosed CdSE quantum dots (LEQDs) and linked them with anti- Her 2 antibodies, as a new type of contrast in THG microscopy in breast cancer [15]. Later on, the same research group studied blood oxygen by measuring the THG spectra of oxy- and deoxyhemoglobin in order to detect tumor growth at early stages [16]. Adur et al., demonstrated that multi-contrast non linear optics microscopy can detect pathological changes of tissue associated with ovarian cancer [17]. Tsai et al., studied complex immune responses among different types of leukocytes by using label free THG imaging [12]. Wu et al. used multiphoton microscopy to distinguish breast cancers from normal tissues and benign lesions [18]. Moreover, Wu et al., quantified the structural changes of collagen in melanoma within a mouse utilizing SHG and THG microscopy [19]. Recently, Weigelin et al. monitor tumor cells during apoptosis by using THG modality (Figure 5.2) [20].

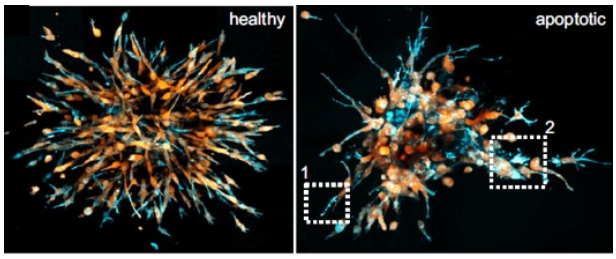

Figure 5.2: Cellular morphologic changes upon apoptosis inductions in tumor cells. MPEF in orange and THG in cyan [20].

For use in life sciences, THG signal can be enhanced by the presence of a multilayered structure as found in membranes and the lipid bodies. Recent evidence indicate that in THG images, the primary sub-cellular source of contrast are lipid bodies (LBs) [21, 22]. The advantage of this approach is that it can be used to study lipid bodies in complex environments.

Lipids bodies (LBs), also named lipid droplets (LD) or adiposomes, are cytoplasmic organelles involved in lipid storage and metabolism, cell signaling and inflammation. Although LBs are largely associated with lipid storage, during the last years they are recognized as dynamic and functionally

active organelles, involved in a variety of functions such as lipid metabolism, cell signaling, and inflammation [23–25]. Increased cytoplasmic lipid accumulation in cells has been observed in a number of clinical and experimental metabolic diseases [23, 26–28]. The shape and the localization of the LBs appear to correlate with the development of metabolic disorders [29].

Nowadays, there is a general consensus that cancer cells display metabolic reprogramming compared to healthy cells, related not only to mechanisms of ATP synthesis through glycolysis (Warburg effect) but also to *de novo* lipid synthesis, with fatty acid synthase and sterol regulatory element-binding protein family as key players in many human cancers. Under physiological conditions, normal cells tend to maintain lipid levels under control, by regulating uptake, synthesis, and mobilization from internal storages. By contrast, tumor cells are able to uptake larger amount of lipids, as well as to enhance lipogenesis and CH production, and to increase fatty acid β -oxidation [26, 30, 31].

Many modern technologies, including mass spectrometry (MS), nuclear magnetic resonance (NMR) and microfluidic devices, are utilized to identify, quantify, and understand the structure and function of lipids in biological systems [29]. However these are complex techniques and the performance of LBs need the use of fluorophores and fixation. In contrast, THG modality can distinguish LBs without any labelling and can give much information about their structure and their position, which are distinct advantages over other techniques. This capability of THG imaging is enabling label free examination of the samples, minimizing photobleaching and photoxicity phenomena.

The need for greatly improved new diagnostic tools in biomedical studies has driven demand for non linear microscopy. THG is successfully applied to diverse biological questions with the goal of reaching a comprehensive description of biological processes. THG microscopy is a relatively simple non linear imaging technique, since it requires a single fs laser beam as excitation source. Only a few seconds of exposure are needed to collect different non linear signals that provide complementary information for the biological sample. Third harmonic generation does not involve energy deposition to the sample and therefore biological specimens do not suffer from side effects (e.g. photobleaching). A benefit of THG microscopy over conventional techniques is that it provides 3D imaging and deeper penetration in scattering samples.

The application of THG imaging quantification analysis based on lipid profiles has been used in a variety of biological samples from our group [32–34]. THG imaging via lipid profile assays enables this process as an ideal tool for examination of many biological issues.

Application of this technology has been successfully extrapolated to BV2 cells [22]. BV-2 cells are resident glial cells that play a significant role in Central Nervous System (CNS) and are connected to many pathological conditions. The activation of these cells is connected to many serious CNS inflammations such as Alzheimer's, Parkinson's, Huntington's and schizophrenia. BV2 cell activation was performed by using lipopolysaccharide (LPS).

In this research, the THG technique was used in order to visualize and quantify the intracellular structures of glia cells. Firstly, THG technique was employed as a tool to delineate and quantify the structures. TPEF and THG signals were collected simultaneously to identify the subcellular structures by using fluorescent dyes for staining lipid bodies, mitochondria and endosomes (Figure 5.3). For the quantitative evaluation of co-localization between the stained structures and THG signals, a Pearson Correlation Coefficient (PCC)-based analysis has been performed (Figure 5.4). This procedure has

been implemented for all three different staining dyes for control and activated BV-2 cells. The analysis showed, a strong correlation (45–65%) of lipid droplets with high THG signal (Figure 5.4a), a very weak correlation (4 - 8%) for mitochondria (Figure 5.4b), while in the case of late endosomes, no co-localization was detected ($\sim$1% very weak positive correlation, Figure 5.4c) in both resting and activated cells. The obtained results are in perfect agreement with previous studies, which have shown that lipid droplets are the main contributors of THG signals from biological samples [21].

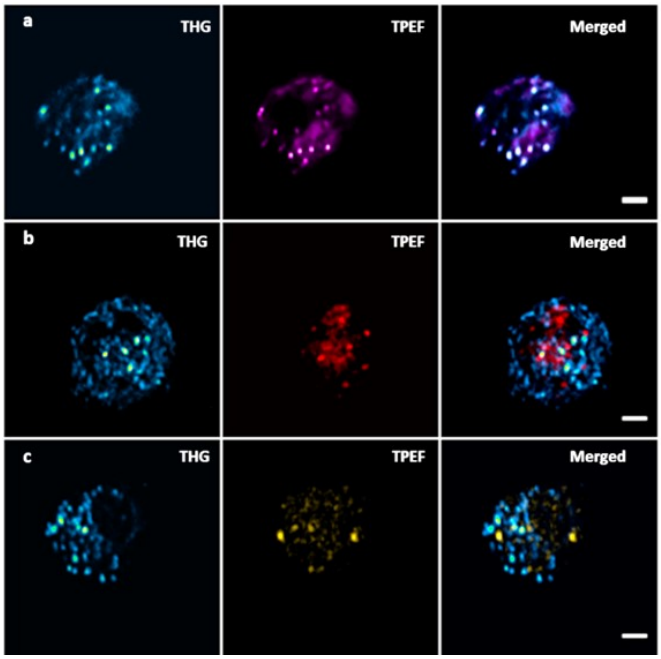

Figure 5.3: Identification of sub-cellular organelles of BV-2 cells that produce high THG signals. THG and TPEF images were collected simultaneously. (a) 2D image (500 x 500 pixels) of a BV-2 cell stained with nile red (THG in blue-green, TPEF in magenta, (b) 2D image of a BV-2 cell stained with Mitotracker red fm (THG in blue-green, TPEF in red), (c) 2D image of a BV-2 cell stained with Alexa 488 (THG in blue-green, TPEF in yellow). Scale bars denote 5 μm.

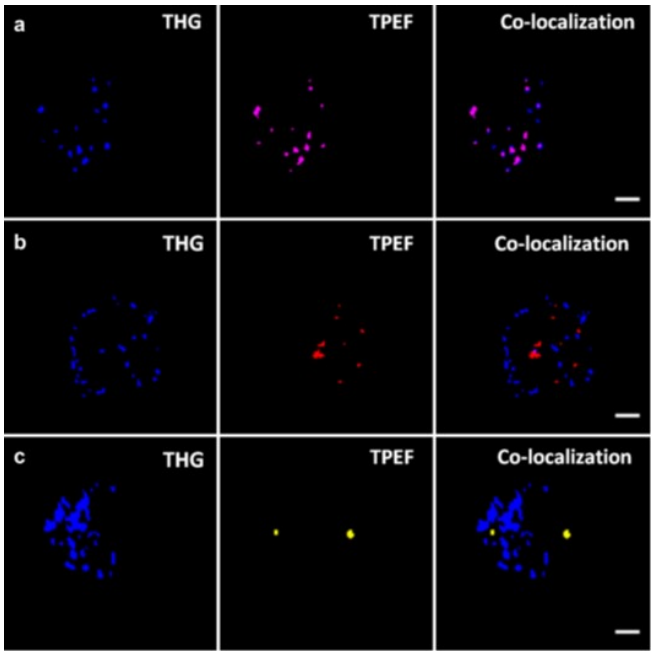

Figure 5.4: Quantitative correlation of TPEF and THG threshold images based on PCC analysis. The same stained control BV-2 cells as in Fig. 3 were implemented. (a) Nile red (lipid droplets, 53% correlation), (b) Mitotracker (mitochondria, 8% correlation), (c) Alexa 488 (late endosomes 0.4% correlation). Scale bars denote 5 μm.

Except from the qualitative information of THG imaging, THG quantification of the intracellular structures – mostly lipid bodies was achieved. By using THG microscopy, it was possible to evaluate the difference between control and activated cells. It was shown that through THG images it could be easily observed that the amount of lipid bodies during cell activation was greater than these of the control cells (Figure 5.5). The quantification of the recorded signals was shown that the mean total area of THG values of the cells after activation was almost ten times bigger than these of non-activated cells. Therefore, the amount of lipid bodies during activation increased in BV2 cells. These results made THG microscopy technique to seem as the proper tool for the illustration and discrimination of BV2 glia cells during activation procedures [22].

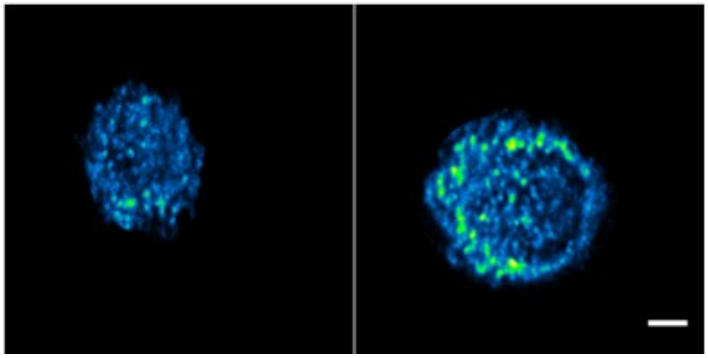

Figure 5.5: THG images of BV-2 cells (a) control (b) activated. The scale bar depicts 5 μm.

Although various studies have shown the potential of label free non linear imaging for cancer re-

search and inflammation, this is the first time in the present thesis that THG microscopy was employed for the accurate imaging and quantification of the lipid content in breast cancer cells.

Indeed, a considerable part of our knowledge on breast carcinomas is based on in vivo and in vitro studies performed with breast cancer cell lines. These provide an unlimited source of homogenous self-replicating material, free of contaminating stromal cells, and often easily cultured in simple standard media [35]. Tremendous advances in our understanding of the biology of breast cancer have been made over the past several decades using breast cancer cell lines [36]. Scientists study the behavior of isolated cells grown in the laboratory for insights into how cells function in the body in health and disease. Experiments using cell lines are useful in developing new diagnostic tests and new treatments for diseases. The first human cell line HeLa, named after Henrietta Lacks who had cervical carcinoma, was established 50 years ago .This breast cancer cell line paved the way for cell culture as we know it today, allowing its widespread development into an important experimental tool in cancer research. One of the major benefits of using cultured cell lines in cancer research is that they offer an infinite supply of a relatively homogeneous cell population that is capable of self-replication in standard cell culture medium [36].

Breast cancer cell lines are used as experimental models and put forward suggestions for improving their use in translational breast cancer research. Due to breast cancer heterogeneity, breast cancer cells are classified into at least five subtypes: Luminal A, Luminal B, Basal – like (triple negative), HER-2. Each subtype has different prognosis and treatment response.

Using representative cell lines corresponding to the different breast cancer subtypes, the aim of the present study was to evaluate whether THG imaging could detect qualitative and quantitative differences between the different subtypes of breast cancer cells and control cells. As aforementioned, THG imaging could distinguish between resting and activated microglia, where lipid bodies were shown to be the major signal emitting intracellular organelles [22]. Taking into consideration the activation state of cancer cells, the present work evaluated THG signaling from various breast cancer cell lines and upon quantification attempted to correlate signal levels to specific types of breast cancer.

THG imaging provides unique structural, anatomical and morphological information in various biological samples at cellular and sub-cellular level. Figure 5.6 depicts an example of THG image of a cancer cell. In THG imaging, one can easily detect nucleus, which is generally presented as a black area in the cell (no THG signal) due to the dense chromatin structure, the increased amount of intracellular signal (mainly arising from LDs) and cellular and nuclear membranes.

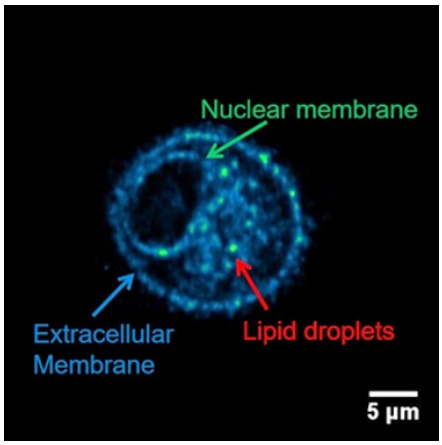

Figure 5.6: 2D THG image of a cancer cell. Scale bar depicts 5 μm.

In this essay, we used some of the widely used breast cancer cell lines (MCF-7, T-47D, BT-474, SK-BR-3, MDA-MB-231, Hs578T) as tumor models. This breast cancer cell line system that we used allowed the assessment of similarities and differences between the cell lines and primary human breast tumors. Breast cancer cell lines can be classified in terms of Luminal, HER2 positive and Basal like (triple negative) (Table 5.1). Luminal type cell lines, characterized by the expression of estrogen and/or progesterone receptors, and represented by MCF7 and T4TD cells showed intracellular and membrane THG signal. The HER2 positive breast cancer cells type of breast cancer, characterized by HER2 expression -positive cells and represented by the BT474 and SKBR3 cell lines cells showed mainly intracellular THG signal, while the triple negative cell type of breast cancer as represented by MDA-MB-231 and Hs578t cells showed mainly nuclear and cellular membrane signal (Figure 5.7).

Table 5.1: Molecular classification of breast cancer cell lines by using immunohistochemistry (IHC) markers. Ki67 nuclear protein, estrogen receptor (ER), progesterone receptor (PR) and human epidermal growth factor 2 (HER2) are markers used as prognostic parameters in breast cancer.

Classification	Immunoprofile	Other characteristics	Cell lines used
Luminal	$ER^+, PR^+, HER2^-$	Ki67 low	MCF-7, T47D
Basal like (Triple Negative)	$ER^-, PR^-, HER2^-$	Ki67 low	MDA-MB231, Hs578t
HER2	$ER^-, PR^-, HER2^+$	Ki67 high	SKBR3
	$ER^+, PR^{+/-}, HER2^+$		BT474

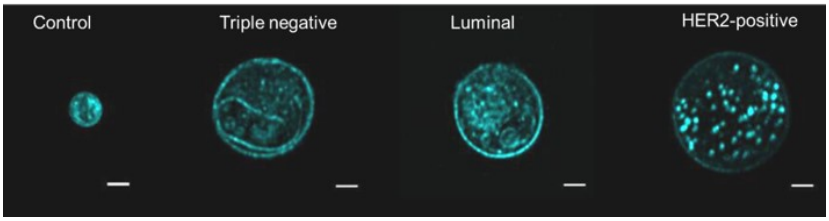

Figure 5.7: THG signal distribution (maximum z projections) of different cell types. Scale bar depicts 5 μm.

For comparison, peripheral blood mononuclear cells (PBMCs) from healthy donors and MCF10a, which represent non-tumorigenic breast epithelial cells, were exploited as controls. However, none of these two cell types can readily be considered as control of the malignant cancer cells. PBMCs have a different cell origin, while MCF10a, which represent non-tumorigenic breast epithelial cells, have been isolated from a Caucasian female with fibrocystic disease. Therefore, these cells were only used as benchmarks for comparison reasons.

Following this, six different breast cancer cell lines, classified as luminal, HER2 positive and triple negative [37], were cultured and submitted to THG imaging. Each cell line presented a specific THG signaling pattern. Thus, luminal cell lines (MCF7 and T47D) showed both intracellular and membrane THG signal, HER2 (BT474 and SKBR3) showed mainly intracellular signal, while triple negative (MDA-MB231 and Hs578T) cells showed mainly nuclear and cellular membrane signal. Non-tumorigenic MCF10a cells displayed both membrane and intracellular signal, while PBMCs displayed essentially intracellular THG signaling (Figure 5.8). In contrast to PBMCs, where nuclei were visualized as regular black areas in the cell due to the dense chromatin structure, cancer cells showed irregular nuclear shapes with enlarged nucleoli (Figure 5.8, arrows).

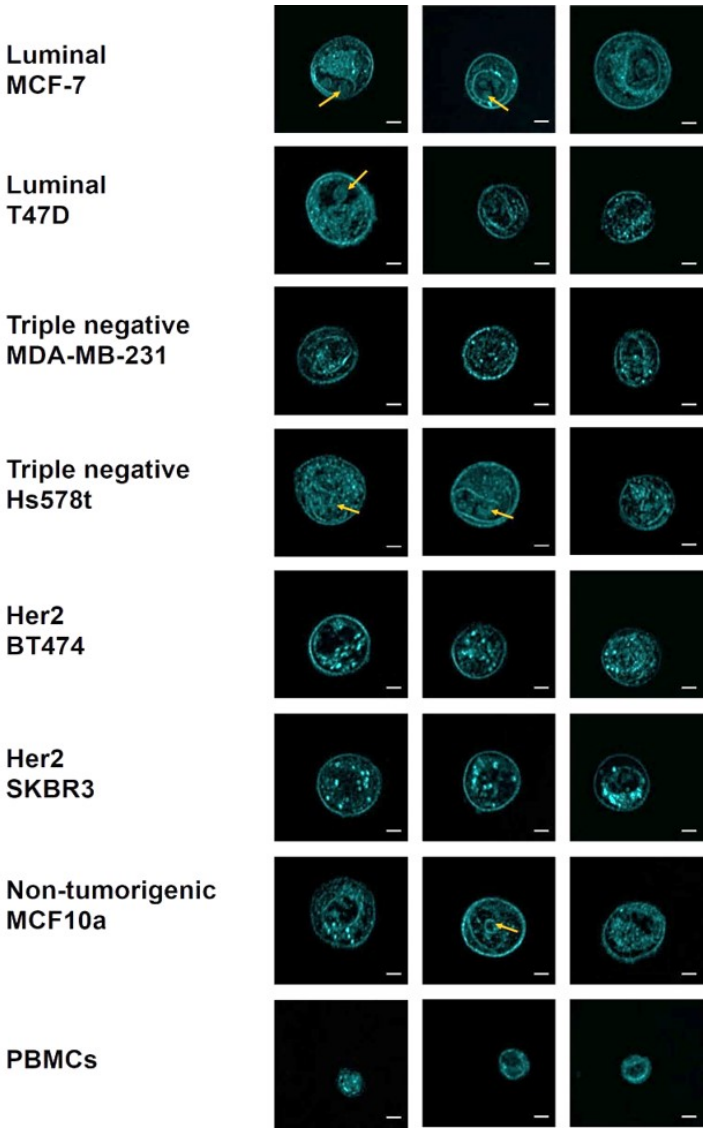

Figure 5.8: THG images (z-projection) of breast cancer cell lines and control cells. Luminal (MCF7 and T47D), HER2 positive (BT474 and SKBR3), triple negative (MDA-MB231 and Hs578T) cancer cell lines as well as non-tumorigenic MCF10a breast cells and control PBMCs were submitted to THG imaging as described in chapter methods The yellow arrows depict the amorphous nucleus and the enclosed nucleolus of cells. Scale bar depicts 5 μm.

Interestingly, membrane signalling was specifically observed in the most aggressive MDA-MB-231 and Hs5787 cells. Indeed, previous studies have indicated that membranes play a crucial role in tumour cell dissemination and metastasis [38–40]. Similarly to the cell membrane, nuclear envelope also consists of a lipid bilayer and it has been shown that alterations in the nuclear membrane affect the behaviour and phenotype of tumour cells [41]. Membrane constitution has been considered to play an important role in breast cancer cell function. During cell activation, microdomains to the cell membrane cluster together proteins and specific lipids involved in the regulation of various cellular processes, many of which are altered in cancer cells. In addition, lipid rafts are influenced by nutrition [42]. It has been shown that fatty acid supplementation sensitises human mammary tumour cells to

the cytotoxic effects of anti-cancer agents [43]. Thus, lipid rafts have been considered to play a role in cancer initiation, progression and cell migration [44]. Additional information as to the breast cancer cells studied here was provided by the nuclear shape. In THG imaging, nucleus is generally presented as a black area in the cell, due to the dense chromatin structure which does not allow the nonlinear light scattering. All cancer cells studied here were characterized by irregular size and shape, enlarged nucleus and nucleolus, which are in agreement with previous studies (Figure 5.8) [45–49].

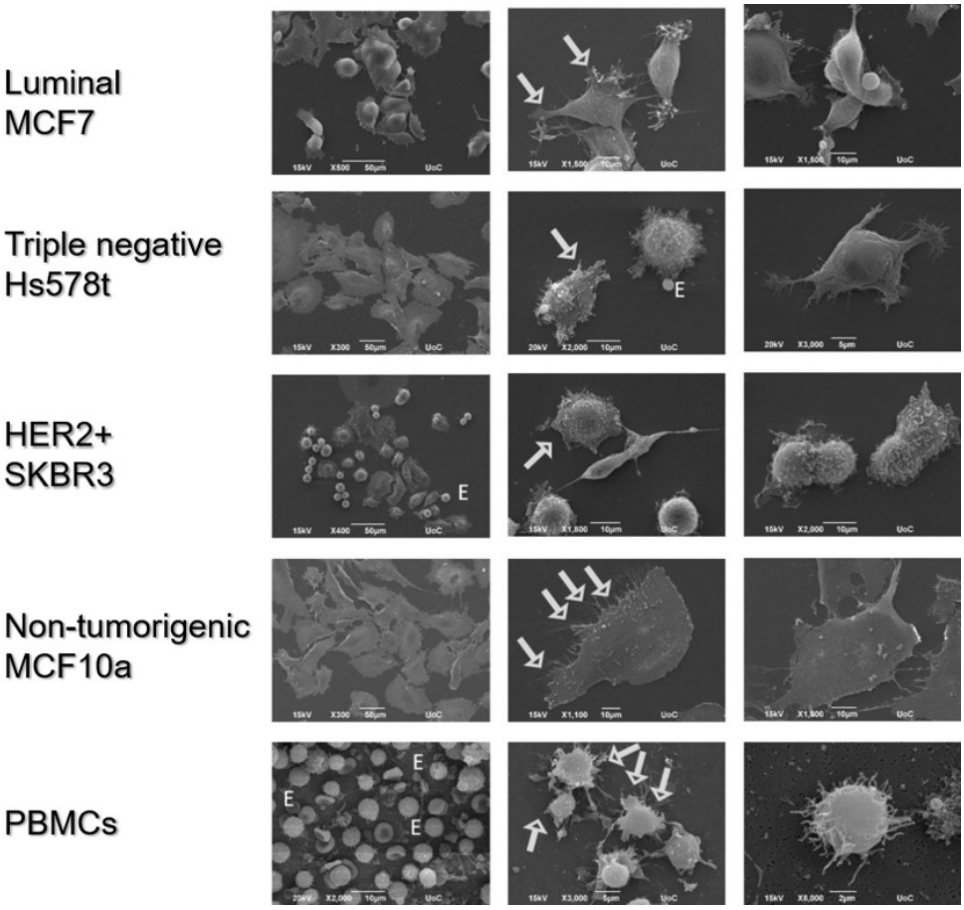

Figure 5.9: SEM images of characteristics cells

Complementary information as to the morphology of cancer cell lines was obtained through scanning electron microscopy (SEM) measurements. Cells were let to adhere for 24 hours on glass cover slips and processed to SEM analysis, thereafter. An expected observation was that none of the cell lines tested comprised homogeneous cell populations. Interestingly, most cells within cancer cell lines showed limited membrane irregularity as compared to controls and limited numbers of adhesion points (arrows Figure 5.9). Such observation could be in accordance with the metastatic ability of these cells. Indeed, SKBR3 cells, which represent the most aggressive line tested here, showed the smallest number of adhesion points as compared to the other cancer cell lines. In addition, after the 24-hour culture, cancer cells showed only limited number of exosomes as compared to controls. Although this was an expected observation because of the lack of additional stimulus, it was important for the evaluation of THG signal, which under these circumstances could not originate from extra-cellular exosomal

structures.

In order to evaluate the lipid droplet origin of the intracellular high THG signal, the cells were stained with Nile red (lipid droplet staining) and THG and TPEF signals were recorded simultaneously (Figure 5.10). The multimodal merged images revealed significant co-localization of THG signal and lipid droplet staining, confirming that lipid droplets were the main sub-cellular structures generating high THG signals. These results endorse the findings in the literature that main intrinsic signal in cells originates from LDs [21].

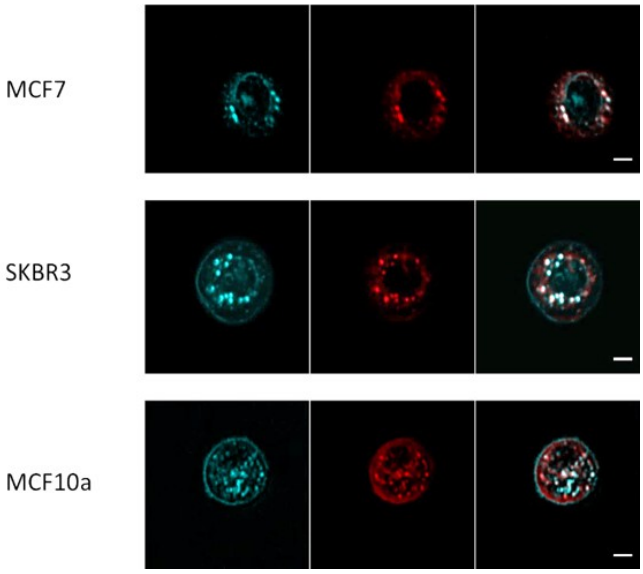

Figure 5.10: 2D THG images of MCF-7, SKBR3 and MCF10a cells (cyan) and 2D TPEF images of the same cells stained with Nile-Red (red). In the merged images (third column), the co-localization of THG-TPEF signals is presented in white color. The scale bar depicts 5 μm.

5.3 Quantification of THG signaling in breast cancer cell lines

In this essay, it was possible to further utilize the THG modality for getting quantitative information. In an attempt to quantify THG signaling, THG intensity values were collected, stored and processed using the Image J software (see Chapter 4).

THG signal quantification was performed by setting a constant threshold, so that regions generating high levels of nonlinear signal were exclusively detected (Figure 5.11). The threshold was set to allow only 30% of the THG signal of the cell area to be analyzed and measured. The quantification of mean THG area was calculated from the 10 central sequential z slices of each cell. For this quantification analysis, forty (40) cells were tested in each case. Significance levels were set at the $p<0.005$ levels using the ANOVA test. Data statistical analysis was performed using SPSS 16.0 software.

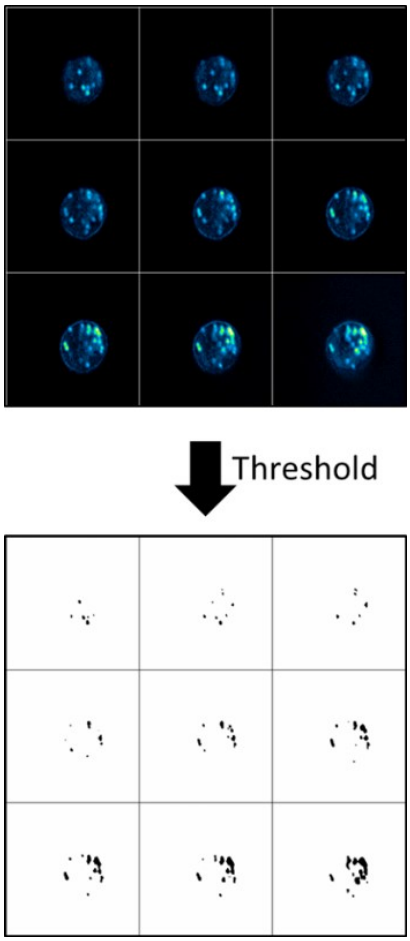

Figure 5.11: Quantification of THG signals using threshold images: (a) sequential 2D THG images of a cancer cell and below their threshold image respectively.

Figure 5.12 a provides the intercorrelations of THG area among the eight different cell types. From the graph below, we can see that the mean total area (mean number of pixels above an intensity threshold) of THG values of PBMCs reported significantly lower THG area ($p<0.05$) than the cancer cells. In addition both HER2-positive BT474 and SKBR3 breast cancer exhibited significantly higher values as compared to all other cells.

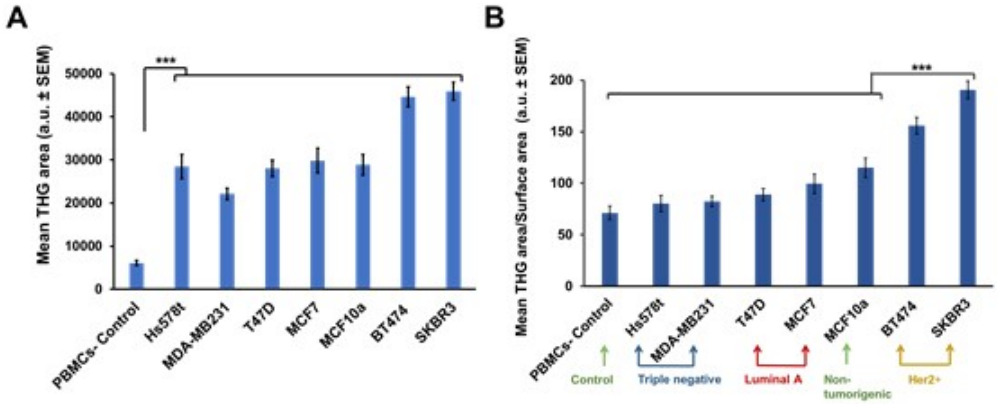

Figure 5.12: THG signal quantification depicted as (a) mean total area, (b) mean THG total area divided by the surface cell area. Data represent mean values ± S.E.M. (n=40 each case). The $***$ denotes $p<0.005$ statistical significance.

Taking into consideration the cell size (normalization by dividing the mean total area by the surface cell area of each cell type), HER2 positive cells were still demonstrating significantly increased levels of THG signal ($p<0.05$; Figure 5.12b). These results indicated that THG signal quantification could distinguish HER2 cells from the other types of breast cancer. This finding is in agreement with prior studies that denote the increased cytoplasmic lipid accumulation detected in cells during inflammation and infectious diseases [26, 27, 31].

Moreover, the division of THG area by the cell surface area revealed that cancer cells could be categorized as to their subtype. However, one should not normalize the results as to cell area, because size is an important feature of cancerous versus physiological cells.

Dissecting THG signal quantification into the different cellular compartments, while maintaining the same threshold, there was an attempt to isolate the THG signal acquired from the cell surface membrane, the intracellular compartments as well as the nuclear membrane (Figure 5.13). For the cell compartmental quantification, cellular, nuclear membrane and intracellular signaling were isolated manually and measured using Image J software.

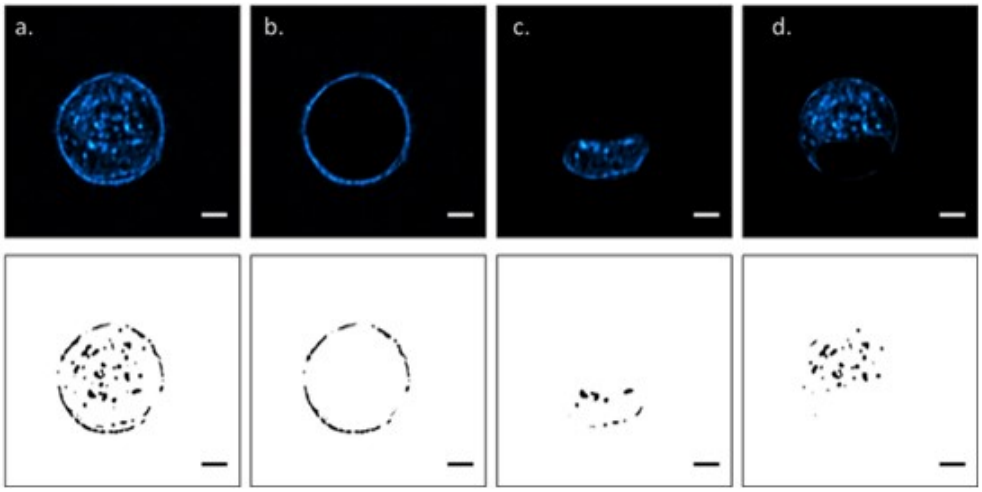

Figure 5.13: z projection THG images of cancer cell's parts (a) whole cell (b) cellular membrane (c) nucleus area and (d) intracellular area. Lower their threshold images are shown respectively. Scale bar depicts 5 μm.

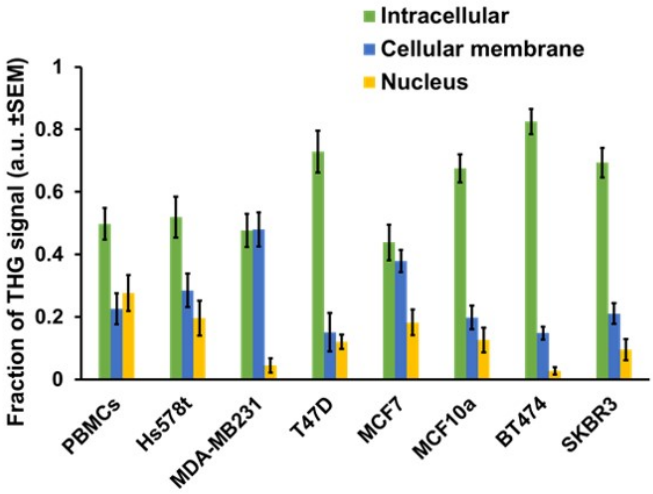

Figure 5.14: THG area of the different cellular compartments (intracellular organelles, cellular membrane, nucleus) divided by the total area of each cell.

Quantification of the THG signal in the different sub-cellular regions demonstrated that BT474 cells mostly displayed intracellular localization of the signal, while in MDA-MB231 cells the cellular membrane was the major source of THG signal. In normal PBMCs, signal mostly originated from nuclear membranes, whereas in SKBR3 cells THG signal was emitted by surface membrane, intracellular area as well as the nucleus (Figure 5.14).

Moreover, THG intensity signal quantification analysis was performed in breast cancer cell lines and PBMCs. This quantification analysis was normalized to a standard THG intensity value and then quantified by setting a constant threshold so that only the regions that provide high THG signals would be examined (see Chapter 4). The weighed mean pixels value of each cell was obtained by repeating this procedure for the 10 central slices of the sample. THG intensity quantification revealed that all

breast cancer cell lines displayed significantly higher values as compared to PBMCs ($p<0.005$) (Figure 5.15).

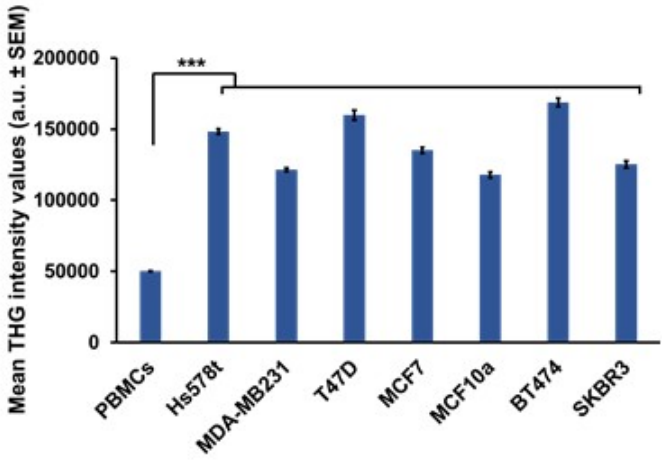

Figure 5.15: THG intensity. Data represent mean values ± S.E.M. (n=40 each case). The $***$ denotes $p<0.005$ statistical significance.

Summarizing the above results in a 3D graph can easily be concluded that THG microscopy has the potential to discriminate between breast cancer cells of different subtypes and could therefore be used for the label-free detection of breast cancer cells among PBMCs (Fig. 16). Thus, quantification of the THG signal provides an objective classification pattern.

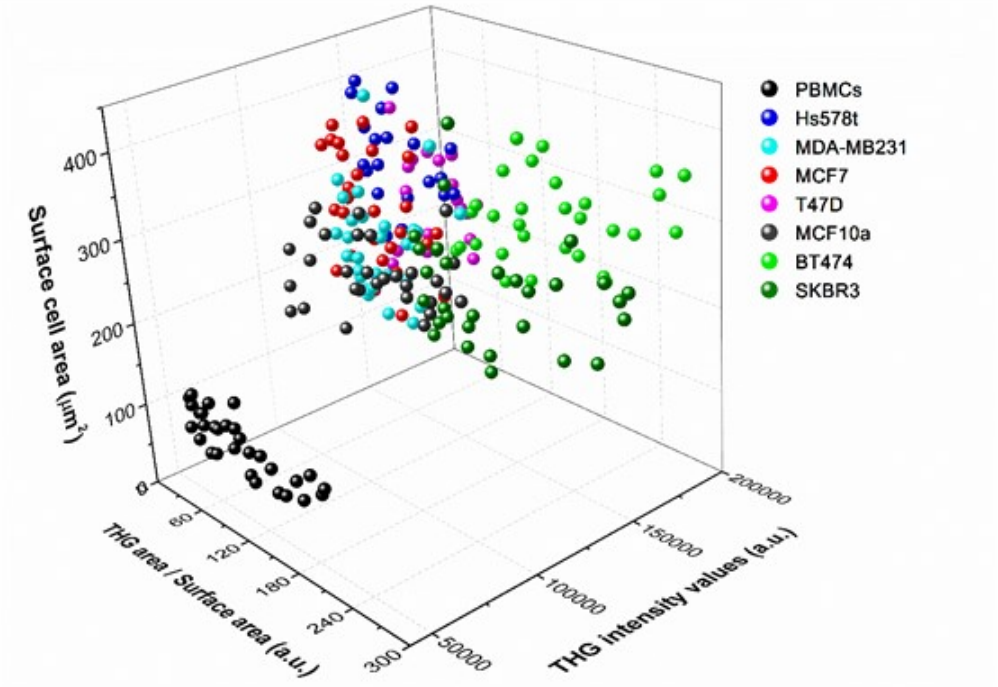

Figure 5.16: 3D graph for the distinction between cancer and PBMCs cells via THG signals quantification. THG area/ surface area of the cell in x-axis, THG intensity values in y-axis and cell surface area in z- axis. The Her2 positive cancer cells (BT474 and SKBR3) and the PBMCs normal cells appeared clearly as separable sub populations of spots in the scatter plot (N=20 for each cell type).

5.4 FTIR spectroscopy and correlation to THG signal of breast cancer cell lines

In an attempt to correlate THG signalling to chemistry, one representative cell line from each subtype type of breast cancer cells was submitted to FTIR analysis. FTIR spectroscopy has been identified as a viable method for lipid analysis [50–52]. Due to their complex chemical composition, lipids absorb in many different regions of the FTIR spectrum. Specifically, characteristic lipid bands, such as the aliphatic group stretching (2800-3000 cm^{-1}) and (900-1800 cm^{-1}) permit qualitative and quantitative analysis of lipid content. Given that each lipid possesses an IR signature uniquely defined by its chemical composition and structure, IR spectroscopy further offers a means of qualitative lipid discrimination.

For FTIR analysis, a smaller sample of breast cancer cell lines was chosen because of the difficulty of obtaining the numbers of cells needed (see Chapter 4). Figure 5.17 depicts the obtained FTIR spectra of the breast cancer cell lines (BT474, MCF7, MDA-MB231) and control cells (PBMCs). As it can been seen, the spectra of PBMCs present lower absorbance values compared with breast cancer cell lines. Appendix A shows the complement collected data of FTIR peaks for each cell type.

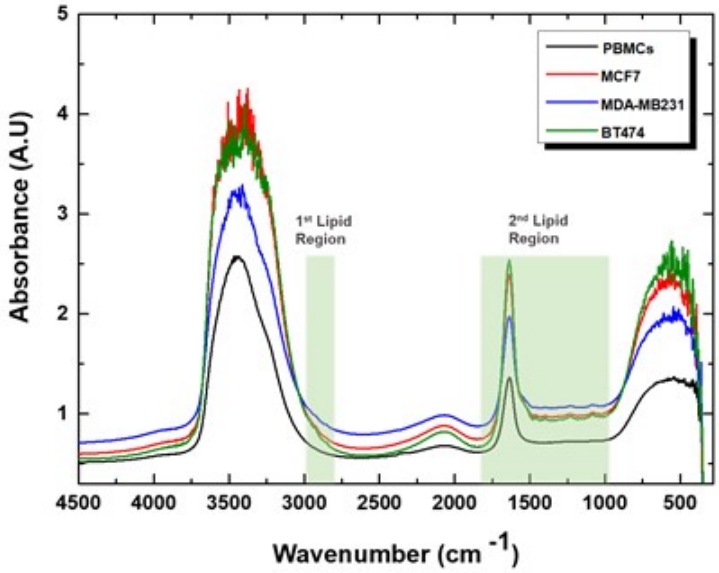

Figure 5.17: FTIR spectra of cancer cell lines (BT474, MCF7, MDA-MB231) and control cells (PBMCs).

Focusing on MCF7, MDA-MB231, BT474 cells and PBMCs, the FTIR spectra analysis could clearly distinguish between cancer cells and control PBMCs, which were always showing lower absorbance levels (Figure 5.17). However, except from the absorbance amplitude, analysis of FTIR spectra could not reveal any specific wavelengths differentiating PBMCs from cancer cells. The complete spectral analysis is shown in Appendix A.

A qualitative inspection between the cells revealed several characteristic features of the FTIR spectra. In particular, specific FTIR spectra were presented only in cancer cells. However, the distinctness between the different cancer cell lines and PBMCs was minimal. Consequently, further analysis of spectra derivative was accomplished. The first order derivative analysis was acquired and could not reveal any specific features differentiating PBMCs from cancer cells. For this reason, second order derivative analysis was accomplished on cancer cell lines and PBMCs. As was pointed out, FTIR spectra were obtained from cells for possible complementarity of THG measurements. Thus this thesis focused on 2nd derivative analysis of lipid bodies and specifically concentrated on spectra characterizing cholesterolsphingomyelin rich regions, as a simulation to lipid rafts.

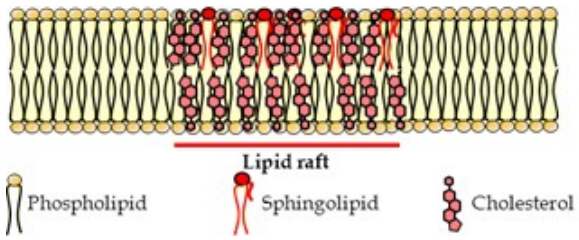

Figure 5.18: Schematic diagram of lipid raft.

Except from lipid bodies which have been considered to play an important role in the tumorigenic process, lipid rafts have also been shown to be involved in cell adhesion and migration of tumour cells [53]. Lipid rafts are cholesterol-enriched microdomains of the cell membrane and possess a highly dynamic nature (Figure 5.18). Lipid rafts have been implicated in cell survival, proliferation, invasion, cell adhesion, protein sorting, and cholesterol metabolism [54]. A significant number of proteins involved in cancer development are associated with lipid rafts. The most important properties of lipid rafts are that they are small, dynamic and heterogeneous, and can include or exclude proteins to variable extents. There is growing interest in the possibility of targeting lipid rafts for cancer treatments due to their role in the regulation of many steps of tumour transformation and progression, such as the apoptotic pathways [44]. To evaluate whether membrane acquired THG signal could correspond to lipid rafts, FTIR analysis was performed and correlated to THG signalling.

Calculation of second order derivative indicates the rate of change of curvature with respect to wavelength and offers additional information about the spectra. Upon acquisition of 2nd derivative, the calculation of the 2nd derivative mean area of FTIR spectra, unwrapped some significant differences between the different breast cancer cell lines and PBMCs (Figure 5.19).

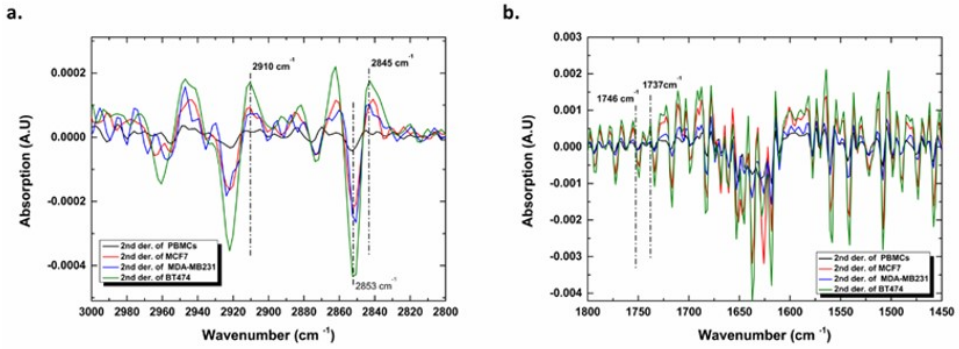

Figure 5.19: 2nd derivative of FTIR spectra of cancer cell lines (BT474, MCF7 , MDA-MB231) and control cells (PBMCs) specified in lipid regions a (3000-2800 cm^{-1}), b(1800-1450 cm^{-1}).

Concentrating on the 2nd derivative spectral peaks 1737 cm^{-1} (lipids), 1746 cm^{-1} (lipids), 2845 cm^{-1} (lipids, cholesterol/phospholipids), 2853 cm^{-1} (lipids/phospholipids), 2910 cm^{-1} (cholesterol/phospholipids) mainly corresponding to lipid rafts, it could observed that BT474 cells displayed significantly higher mean areas as compared to MCF7, MDA-MB231,and PBMCs ($p<0.005$) (Table 5.2) (Figure 5.19). Table 5.2 summarizes the chemical information [52] of these specific peaks and the corresponding mean integrated area of breast cancer cell lines and PBMCs, respectively.

Table 5.2: Integrated 2nd derivative spectra depict the concentration (spectra peak area) of specific chemical bonds that presented in breast cancer cell lines and PBMCs.

Wavenumber (cm^{-1})	Chemical Information	BT474	MCF7	MDA-MB231	PBMCs
1737	C=O band, C=O stretching lipids	0.52	0.25	0.14	0.08
1746	v(C=C) lipids, fatty acids	0.49	0.23	0.21	0.08
2845	Stretching C-H (cholesterol, phospholipids)	0.40	0.23	0.22	0.15
2853-8	Symmetric stretching vibrations of CH_2 of acyl chains (lipids), Asymmetric CH_2 stretching mode of the methylene chains in membrane lipids	0.73	0.11	0.08	0.09
2910-2	Cholesterol, phospholipids. Stretching vibrations of CH_2 and CH_3 of phospholipids.	0.63	0.23	0.13	0.01

In Figure 5.20 the fraction of FTIR 2nd derivative area of breast cancer cell lines and PBMCs (N-3 respectively for each cell type) can been seen.

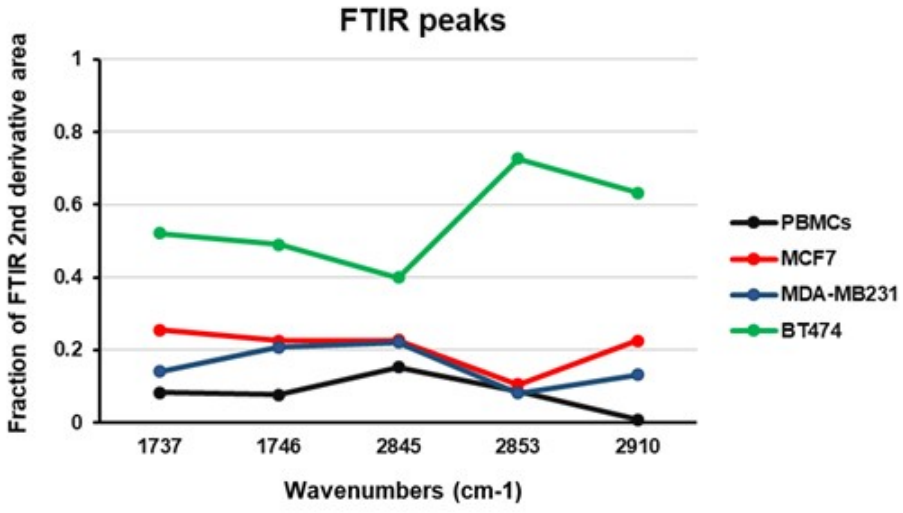

Figure 5.20: Percentage of FTIR 2nd derivative spectrum area at wavelengths 1737, 1746, 2845, 2853 and 2910 cm^{-1}. Data representing mean values of three single experiments of the five different peaks mainly correspond to lipid rafts. BT474 cells appear higher values as compared to MCF7, MDA-MB231 breast cancer cells and PBMCs. SEM is in the order of 25% of the values (not shown) due to the limited number of FTIR measurements (n=3 in each case).

After the descriptive FTIR analysis, the obtained FTIR integrated area that corresponds to the concentration of the respective chemical bonds was correlated to THG signals. Specifically, the results of Table 5.2 correlated to THG mean lipid surface area and THG signal intensity (Figure 5.21).

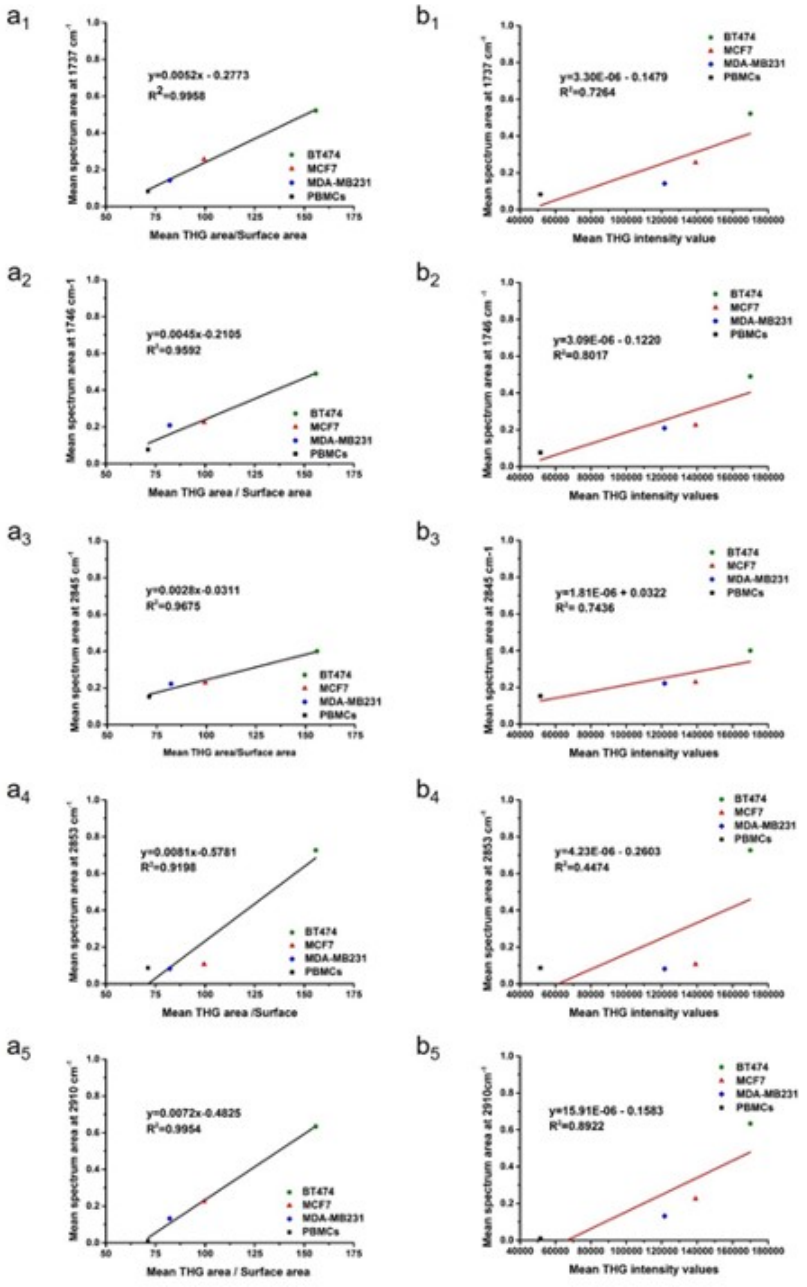

Figure 5.21: Correlation of FTIR 2nd derivative spectra with THG (a, left column) mean area divided by the surface cell area and (b, right column) mean THG intensity values for specific peaks of spectrum of lipid regions. With exception of the mean THG intensity at 2853 cm^1 (R^2_{2853} = 0.4474, Figure 5.21b_4), in all other cases, satisfactory fitting values were obtained.

These results correlated to the mean THG area divided by the cell surface (R^2_{1737}= 0.9958, R^2_{1746} =0.9592, R^2_{2845} =0.9675, R^2_{2853} =0.9198, R^2_{2910} =0.9954, Figure 5.21A) and to THG intensity (mean pixel value for each slice of a cell was calculated by multiplying the representative area with the

mean intensity value of the corresponding pixels, R^2_{1737} =0.7264, R^2_{1746} =0.8017, R^2_{2845} =0.7436, R^2_{2853} =0.4474, R^2_{2910} =0.8922, Figure 5.21B).

The above findings showed that the mean area of 2nd derivative spectra was correlated with THG signal mean area and intensity. Therefore, the results presented here showed for the first time a correlation between THG imaging and FTIR analysis, relating thus THG imaging to chemistry. Other techniques, such as Coherent Anti – stokes Raman Scattering (CARS) microscopy has been proposed as a promising possibility tool in chemical imaging with the benefit of providing chemical information. However, CARS has not gained widespread adoption for routine visualization of lipid depositions for two main reasons; first the cost of acquiring CARS microscopy instrumentation is substantial and second setting up and operation of a CARS microscope requires considerable expertise in nonlinear optics and attentive maintenance, including frequent fine-tuning and precise alignment of two tightly synchronized, mode-locked, ultra-fast laser light sources [55–57]. In contrast THG imaging requires a single pulsed-laser light source, alleviating the technical challenges of implementing more complex techniques to detect fat stores in living cells.

5.5 Conclusion

Nonlinear optical imaging techniques shed new light in the delineation of various biological and biomedical processes while providing a strong impact on early detection of diseases [18, 22, 58]. In this thesis, THG microscopy was used as a new, label free, easy to use, non-destructive imaging technique for the classification of different subtypes of breast cancer cell lines and their distinction from non-cancer cells. The discrimination between the different types of cells was based on the quantification of collected THG signals and their correlation to FTIR spectra. It was observed that breast cancer cells displayed an increased lipid content compared to normal cells, which correlated to FTIR 2nd derivative mean spectra area of cholesterol/ spingomyelin rich areas that possibly correspond to lipid rafts.

Previous studies had shown that THG imaging could distinguish between activated and non-activated microglia cells [22]. Breast cancer cell lines, which are expected to display a constantly metabolically activated profile, were shown to provide higher levels of THG signal in terms of both intensity and mean signal area, as compared to controls. Surprisingly, each cell subtype showed different THG signal location. Luminal cell lines showed intracellular and membrane THG signal, HER2+ cells lines depicted mainly intracellular THG signal, while triple negative cell lines showed mainly nuclear and cellular membrane signal.

The cytoplasmic structures were demonstrated to co-localize with LDs, which is in agreement with previous observations [21, 22, 25]. Indeed, increased numbers of LDs have been correlated to various pathologic conditions. Thus, increased cytoplasmic lipid accumulation in leukocytes and other cells has been observed in a number of clinical and experimental inflammatory and infectious diseases [23, 26, 27, 30].

Correlating THG imaging to organelle chemistry would be a quite important feature to the analysis of biological samples. Since THG signal is generated from the refractive index changes and dispersion, it can be hypothesized that chemical changes to the membranes could affect THG signalling. Indeed,

aromatic hydrocarbons cause dilation of the intracellular space, altering thus intra-cytoplasmic vacuoles [17, 59, 60]. The correlation of THG signal area and intensity to C-H, C=O stretching, cholesterol and phospholipid spectra indicates that THG signal could reflect the presence of aromatic hydrocarbons and cholesterol. In addition, cholesterol and the carbonyl group of sphingomyelin is obscured by the complexity of different possible hydrogen bonding and coupling between the N–H and the C=O group vibrations, apparent in lipid rafts [50]. Thus, the increased THG signal observed in activated cells could be extrapolated to increased lipid raft content of the membranes. Further studies using artificial membranes with variable hydrocarbon, sphingomyelin and cholesterol constitution are needed to definitely demonstrate such correlation. The correlation of THG signalling to chemistry could open new areas of research and technology, where fast label free imaging could provide valuable information on the malignant area of the cells or tissues.

The presented work has a significant clinical potential, since it perceives quantitative changes in healthy and malignant human cells. Understanding the intracellular lipid droplet distribution and membrane morphology could provide information on lipid metabolism in tumour cells for exploitation as therapeutic targets [23–25]. Although more research is needed to understand the correlation between lipids and cancer pathology and automate the segmentation analysis, the nonlinear imaging modality of THG has the potential to discriminate among the different cancer cell types [58]. THG microscopy assesses lipid and membrane changes in healthy, cancer cells and tissues ex vivo by absolute parameters that quantify inflammatory damage. This paves the way for novel, label free methods to quantify therapeutic response in cancer and computerize histological examinations in terms of digital pathology.

Bibliography

[1] url: http://anatomyhumancharts.com/diagram-of-the-breast/diagram-of-the-breast-breast-implant-diagram-stock-illustration-illustration-of-plastic/.

[2] Chinoy Lakhtakia. "A Brief History of Breast Cancer: Part II - Evolution of surgical pathology". In: *Sultan Qaboos Univ Med J.* 14.3 (2014), e319–e322. url: https://www.ncbi.nlm.nih.gov/pubmed/25097765.

[3] Vineeta Singh et al. "New diagnostic techniques for breast cancer detection". In: (2008).

[4] Jeffrey S Ross et al. "Breast cancer biomarkers and molecular medicine". In: *Expert review of molecular diagnostics* 3.5 (2003), pp. 573–585. issn: 1473-7159.

[5] E. Politaki et al. "A Comparison of Three Methods for the Detection of Circulating Tumor Cells in Patients with Early and Metastatic Breast Cancer". In: *Cellular Physiology and Biochemistry* 44.2 (2017), pp. 594–606. issn: 1015-8987. doi: 10.1159/000485115. url: https://www.karger.com/DOI/10.1159/000485115.

[6] Francois-Clement Bidard, Charlotte Proudhon, and Jean- Yves Pierga. "Circulating tumor cells in breast cancer". In: *Molecular Oncology* 10.3 (2016), pp. 418–430. issn: 1574-7891. doi: https://doi.org/10.1016/j.molonc.2016.01.001. url: http://www.sciencedirect.com/science/article/pii/S1574789116000041.

[7] Weissleder R. Condeelis J. "In vivo imaging in cancer." In: *Cold Spring Harb Perspect Biol* 2.12 (2010), a003848. doi: 10.1101/cshperspect.a003848.

[8] Liu TM. Chen CK. "Imaging morphodynamics of human blood cells in vivo with the video-rate third harmonic generation microscopy." In: *Biomed Opt Express* 3.11 (2012), pp. 2860–5. doi: 10.1364/BOE.3.002860.

[9] Shi-Wei Chu et al. "In vivo developmental biology study using noninvasive multi-harmonic generation microscopy". In: *Optics express* 11.23 (2003), pp. 3093–3099.

[10] S. Chen et al. "Virtual Biopsy of Human Skin by Using Noninvasive Higher Harmonic Generation Microscopy". In: *IEEE Journal of Selected Topics in Quantum Electronics* 16.3 (2010), pp. 478–492. issn: 1077-260X. doi: 10.1109/JSTQE.2009.2031987.

[11] S. Y. Chen, H. Y. Wu, and C. K. Sun. "In vivo harmonic generation biopsy of human skin". In: *J Biomed Opt* 14.6 (2009), p. 060505. issn: 1083-3668. doi: 10.1117/1.3269676.

[12] Cheng-Kun Tsai et al. "Imaging granularity of leukocytes with third harmonic generation microscopy". In: *Biomedical Optics Express* 3.9 (2012), pp. 2234–2243. doi: 10.1364/BOE.3.002234. url: http://www.osapublishing.org/boe/abstract.cfm?URI=boe-3-9-2234.

[13] Markus Rehberg et al. "Label-Free 3D Visualization of Cellular and Tissue Structures in Intact Muscle with Second and Third Harmonic Generation Microscopy". In: *PLOS ONE* 6.11 (2011), e28237. doi: 10.1371/journal.pone.0028237. url: https://doi.org/10.1371/journal.pone.0028237.

[14] Adam E Tuer et al. "Nonlinear multicontrast microscopy of hematoxylin-and-eosin-stained histological sections". In: *Journal of biomedical optics* 15.2 (2010), p. 026018.

[15] Chieh-Feng Chang et al. “Cell tracking and detection of molecular expression in live cells using lipid-enclosed CdSe quantum dots as contrast agents for epi-third harmonic generation microscopy”. In: *Optics express* 16.13 (2008), pp. 9534–9548.

[16] Chieh-Feng Chang, Che-Hang Yu, and Chi-Kuang Sun. “Multi-photon resonance enhancement of third harmonic generation in human oxyhemoglobin and deoxyhemoglobin”. In: *Journal of biophotonics* 3.10-11 (2010), pp. 678–685.

[17] Javier Adur et al. “Optical Biomarkers of Serous and Mucinous Human Ovarian Tumor Assessed with Nonlinear Optics Microscopies”. In: *PLOS ONE* 7.10 (2012), e47007. doi: 10.1371/journal.pone.0047007. url: https://doi.org/10.1371/journal.pone.0047007.

[18] X. Wu et al. “Label-free detection of breast masses using multiphoton microscopy”. In: *PLoS One* 8.6 (2013), e65933. issn: 1932-6203. doi: 10.1371/journal.pone.0065933.

[19] P. C. Wu et al. “In vivo quantification of the structural changes of collagens in a melanoma microenvironment with second and third harmonic generation microscopy”. In: *Sci Rep* 5 (2015), p. 8879. doi: 10.1038/srep08879.

[20] B. Weigelin, G. J. Bakker, and P. Friedl. “Third harmonic generation microscopy of cells and tissue organization”. In: *J Cell Sci* 129.2 (2016), pp. 245–55. issn: 0021-9533. doi: 10.1242/jcs.152272.

[21] Delphine Débarre et al. “Imaging lipid bodies in cells and tissues using third-harmonic generation microscopy”. In: *Nature methods* 3.1 (2006), p. 47.

[22] E Gavgiotaki et al. “Third harmonic generation microscopy as a reliable diagnostic tool for evaluating lipid body modification during cell activation: the example of BV-2 microglia cells”. In: *Journal of structural biology* 189.2 (2015), pp. 105–113.

[23] Robert V. Farese and Tobias C. Walther. “Lipid Droplets Finally Get a Little R-E-S-P-E-C-T”. In: *Cell* 139.5 (2009), pp. 855–860. issn: 0092-8674. doi: https://doi.org/10.1016/j.cell.2009.11.005. url: http://www.sciencedirect.com/science/article/pii/S0092867409014172.

[24] Parton RG Martin S. “Lipid droplets: a unified view of a dynamic organelle.” In: *Nat Rev Mol Cell Biol.* 7.5 (2006), pp. 373–8. doi: 10.1038/nrm1912.

[25] Fullekrug J Digel M Ehehalt R. “Lipid droplets lighting up: insights from live microscopy.” In: *FEBS Lett.* 584.11 (2010), pp. 2168–75. doi: 10.1016/j.febslet.2010.03.035.

[26] Patricia T Bozza and João PB Viola. “Lipid droplets in inflammation and cancer”. In: *Prostaglandins, Leukotrienes and Essential Fatty Acids (PLEFA)* 82.4-6 (2010), pp. 243–250.

[27] Halina Abramczyk et al. “The role of lipid droplets and adipocytes in cancer. Raman imaging of cell cultures: MCF10A, MCF7, and MDA-MB-231 compared to adipocytes in cancerous human breast tissue”. In: *Analyst* 140.7 (2015), pp. 2224–2235.

[28] Johannes V Swinnen, Koen Brusselmans, and Guido Verhoeven. “Increased lipogenesis in cancer cells: new players, novel targets”. In: *Current Opinion in Clinical Nutrition & Metabolic Care* 9.4 (2006), pp. 358–365.

[29] Sabine Daemen et al. “Microscopy tools for the investigation of intracellular lipid storage and dynamics”. In: *Molecular metabolism* 5.3 (2016), pp. 153–163.

[30] Luca Tirinato et al. “An overview of lipid droplets in cancer and cancer stem cells”. In: *Stem cells international* 2017 (2017).

[31] Rossana C. N. Melo et al. “Imaging Lipid Bodies Within Leukocytes with Different Light Microscopy Techniques”. In: *Methods in molecular biology (Clifton, N.J.)* 689 (2011), pp. 149–161.

[32] Evangelia Gavgiotaki et al. “THG imaging of lipid body profiles in diagnosis of biological samples”. In: *Medical Research Archives* 4.7 (2016).

[33] K. Palikaras et al. “Ectopic fat deposition contributes to age-associated pathology in Caenorhabditis elegans”. In: *Journal of lipid research* 58.1 (2017), pp. 72–80. issn: 0022-2275. doi: 10.1194/jlr.M069385.

[34] C. Kyvelidou et al. “Following the course of pre-implantation embryo patterning by non- linear microscopy”. In: *J Struct Biol* 176.3 (2011), pp. 379–86. issn: 1047-8477. doi: 10.1016/j.jsb.2011.09.007.

[35] M. Lacroix and G. Leclercq. “Relevance of breast cancer cell lines as models for breast tumours: an update”. In: *Breast Cancer Res Treat* 83.3 (2004), pp. 249–89. doi: 10.1023/B:BREA.0000014042.54925.cc.

[36] Speirs Holliday. “Choosing the right cell line for breast cancer research”. In: *Breast cancer research : BCR* 13.4 (2011), pp. 215–215. doi: 10.1186/bcr2889.

[37] Richard M Neve et al. “A collection of breast cancer cell lines for the study of functionally distinct cancer subtypes”. In: *Cancer cell* 10.6 (2006), pp. 515–527. doi: 10.1016/j.ccr.2006.10.008.

[38] Manwen He, Shuai Guo, and Zhili Li. “In situ characterizing membrane lipid phenotype of breast cancer cells using mass spectrometry profiling”. In: *Scientific reports* 5 (2015), p. 11298.

[39] Izabela Dobrzyńska et al. “Characterization of human bladder cell membrane during cancer transformation”. In: *The Journal of membrane biology* 248.2 (2015), pp. 301–307.

[40] Hideki Yamaguchi et al. “Lipid rafts and caveolin-1 are required for invadopodia formation and extracellular matrix degradation by human breast cancer cells”. In: *Cancer research* (2009), pp. 0008–5472.

[41] Kin-Hoe Chow, Rachel E Factor, and Katharine S Ullman. “The nuclear envelope environment and its cancer connections”. In: *Nature Reviews Cancer* 12.3 (2012), p. 196.

[42] Parveen Yaqoob. “The nutritional significance of lipid rafts”. In: *Annual review of nutrition* 29 (2009), pp. 257–282.

[43] Séverine Colas et al. “Sensitization by dietary docosahexaenoic acid of rat mammary carcinoma to anthracycline: a role for tumor vascularization”. In: *Clinical cancer research* 12.19 (2006), pp. 5879–5886.

[44] Irina S Babina et al. “Lipid rafts as master regulators of breast cancer cell function”. In: (2011).

[45] Rena Chiotaki, Hara Polioudaki, and Panayiotis A Theodoropoulos. “Differential nuclear shape dynamics of invasive andnon-invasive breast cancer cells are associated with actin cytoskeleton organization and stability”. In: *Biochemistry and cell biology* 92.4 (2014), pp. 287–295.

[46] Micah Webster, Keren L Witkin, and Orna Cohen-Fix. “Sizing up the nucleus: nuclear shape, size and nuclear-envelope assembly”. In: *Journal of cell science* 122.10 (2009), pp. 1477–1486.

[47] Jian Lin et al. “Label-free three-dimensional imaging of cell nucleus using third- harmonic generation microscopy”. In: *Applied Physics Letters* 105.10 (2014), p. 103705. doi: 10.1063/1.4895577. url: https://aip.scitation.org/doi/abs/10.1063/1.4895577.

[48] William H Wolberg, W Nick Street, and Olvi L Mangasarian. “Importance of nuclear morphology in breast cancer prognosis”. In: *Clinical Cancer Research* 5.11 (1999), pp. 3542–3548.

[49] Daniele Zink, Andrew H Fischer, and Jeffrey A Nickerson. “Nuclear structure in cancer cells”. In: *Nature reviews cancer* 4.9 (2004), p. 677.

[50] Zoran Arsov and Luca Quaroni. “Detection of lipid phase coexistence and lipid interactions in sphingomyelin/cholesterol membranes by ATR-FTIR spectroscopy”. In: *Biochimica et Biophysica Acta (BBA)-Biomembranes* 1778.4 (2008), pp. 880–889.

[51] Andreas Barth and Parvez I Haris. *Biological and biomedical infrared spectroscopy*. Vol. 2. IOS press, 2009.

[52] Zanyar Movasaghi, Shazza Rehman, and Dr Ihtesham ur Rehman. “Fourier transform infrared (FTIR) spectroscopy of biological tissues”. In: *Applied Spectroscopy Reviews* 43.2 (2008), pp. 134–179.

[53] Toshiyuki Murai. “The role of lipid rafts in cancer cell adhesion and migration”. In: *International journal of cell biology* 2012 (2012).

[54] Anil Badana et al. “Lipid raft integrity is required for survival of triple negative breast cancer cells”. In: *Journal of breast cancer* 19.4 (2016), pp. 372–384.

[55] Hilde A Rinia et al. “Quantitative label-free imaging of lipid composition and packing of individual cellular lipid droplets using multiplex CARS microscopy”. In: *Biophysical journal* 95.10 (2008), pp. 4908–4914.

[56] Conor L Evans and X Sunney Xie. “Coherent anti-Stokes Raman scattering microscopy: chemical imaging for biology and medicine”. In: *Annu. Rev. Anal. Chem.* 1 (2008), pp. 883–909.

[57] Claudia Di Napoli et al. “Chemically-specific dual/differential CARS micro-spectroscopy of saturated and unsaturated lipid droplets”. In: *Journal of biophotonics* 7.1-2 (2014), pp. 68–76.

[58] N. V. Kuzmin et al. “Third harmonic generation imaging for fast, label-free pathology of human brain tumors”. In: *Biomedical Optics Express* 7.5 (2016), pp. 1889–1904. doi: 10.1364/BOE.7.001889. url: http://www.osapublishing.org/boe/abstract.cfm?URI=boe-7-5-1889.

[59] Rüdiger Meiß et al. “Effect of silybin on hepatic cell membranes after damage by polycyclic aromatic hydrocarbons (PAH)”. In: *Inflammation Research* 12.1 (1982), pp. 254–257.

[60] Woowon Lee et al. “Third-harmonic generation imaging of breast tissue biopsies”. In: *Journal of microscopy* 264.2 (2016), pp. 175–181.

Chapter 6

THG microscopy in breast tissue

In the previous chapter, THG microscopy used to differentiate and categorize the different breast cancer cell subtypes of control cells. Herein, nonlinear microscopy utility was integrated in the case of human breast cancer tissues. The main object of this research was to find a new diagnostic tool to recognize and grade the tumor type using nonlinear microscopy, without the need of staining the preparation or damage of the tissues. Quantification analysis of THG signals successfully differentiated malignant from normal tissue samples and discriminated the different grades of tumor tissues based on their THG area and THG intensity signals. Additionally, FTIR spectroscopy operated with three different methods, was able to provide chemical information about the different tissues and correlated with THG signals.

6.1 Breast cancer and diagnosis

Nonlinear microscopy has already been successfully utilized as diagnostic tool for the distinction of cancer cells from control cells. In this chapter, nonlinear microscopy will focus on the analysis of multicellular layers, namely breast tissues. In tissues, the cells are committed to collaboration by sending, receiving and interpreting a highly developed set of extracellular signals that can be seen as social control dictating to each cell, how to act. Thus, cancer could be defined as the disease in which certain cells cease to respond to normal stimuli.

An abnormal cell that grows and divides out of control and escapes immunosurveillance will give rise to a tumor. A tumor that has spread beyond the layer of the tissue in which it developed, and is growing into surrounding healthy tissues is called invasive. As long as the tumor cells do not become invasive, the tumor is said to be benign. A tumor is considered as cancer (malignant), only if tumor cells have the ability to invade the surrounding tissue. The invasiveness allows cancer cells to break loose, enter blood or lymph vessels and form secondary tumors called metastases. The abnormal cell growth and division together with invasiveness is what makes cancers especially dangerous.

Breast cancer is defined as a malignant growth that originates from breast tissue, mostly from breast epithelium. Epithelial tissue surrounds the cavities and surfaces of many structures throughout the body. Its location defines the borders between the internal and external environments and consequently epithelial cells are constantly exposed to mechanical damage. To be able to replace lost cells

and maintain their integrity, epithelial cells display very good proliferative properties. Indeed, many of the different cancers throughout the body are in fact the result of uncontrolled proliferation of epithelial cells. Breast epithelial include the milk- secreting cells in the alveoli, and the ductal cells of the ducts. Most breast tumors originate from the ductal epithelium, while only a minority originates from the lobule epithelium. Non-invasive breast cancers stay within the milk ducts or lobules in the breast, whereas invasive cancers grow into or invade the surrounding healthy tissues or beyond breast, establishing tumor sites at other locations throughout the body. Most breast cancers are invasive.

Breast cancer is one of the most common malignancies in females worldwide, which caused by a combination of genetic and environmental factors. Numerous risk factors associated with breast cancer have been recognized. Nonetheless, not all breast cancer patients have the same clinical picture, but it believed that some factors increase a woman's risk of breast cancer more than others [1].

Breast cancers encompass a heterogeneous array of tumor cell types that are classified according to their histological and molecular characteristics. Currently, breast cancers are sorted into one of at least four subtypes, although classification methods are being refined as molecular profiling techniques improve. Each subtype is associated with a different prognosis and course of treatment. Therefore, to generate the most effective treatment options, investigators need in vitro research tools that represent the heterogeneity of breast cancers in vivo.

Early detection of breast cancer both primary and recurrent is of considerable clinical importance, and it can be used to make treatment decisions. Until now, the use of molecular biomarkers assures that breast cancer (BC) patients receive treatment. Tumor markers play a crucial role in diagnosis, monitoring response to therapy, early detection of metastasis and determination of recurrence in patients with breast cancer. However, the real usefulness of tumor markers in the management of breast cancer has been questioned because of the low diagnostic sensitivity and specificity.

In literature, several studies have demonstrated the relevance of the use of biomarkers obtained from tissue samples for classification and assessment of tumor development. Although molecular markers, such as hormone receptors (estrogen receptor [ER]/progesterone receptor [PR]), HER2 and Ki67 have been used to classify the heterogeneous disease into categories, to predict the prognosis and determine the treatment modalities, current diagnoses and therapies are incomplete because numerous patients die of relapsed disease. Thus, improved diagnosis using novel methods for cell evaluation to decide therapeutic strategy is required [2–5].

Currently, there are not ideal tumor markers that can be specific and sensitive for evaluating the disease for all cancer patients. Consequently, there is an ongoing search for new tools to reduce recalls and unnecessary biopsies while maintaining or improving cancer detection rates.

The idea of this research is to specifically use the intrinsic optical property of the tissue to reveal qualitatively and quantitatively information of cells in breast cancer tissues by using nonlinear microscopy.

6.2 Nonlinear microscopy in cancer studies

As previously referred in detail, label-free nonlinear optical microscopy produces high-resolution images with rich functional and structural information based on intrinsic molecular contrast. Several

studies have shown that nonlinear optical microscopy provides high probing sensitivity and makes it a potential imaging method for early detection of cancer and inflammations [6–14].

The last decade, nonlinear optical modalities have been used to detect the response in neoadjuvant therapy during cancer [15–17] and to define surgical margins in tissues [9, 15, 18]. Recently, the application of this technology has been proposed for clinical studies, whereas it has been used for intravital imaging of biological models [19–21].

The last decade, nonlinear optical modalities have been used to detect the response in neoadjuvant therapy during cancer [15–17] and to define surgical margins in tissues[9, 15, 18]. Recently, the application of this technology has been proposed for clinical studies, whereas it has been used for intravital imaging of biological models [19–21].

THG is a striking technique that can potentially be translated as a diagnostic tool for the early detection of cancer and inflammatory disorders **??**. In contrast to other nonlinear imaging techniques, THG not only enables recording of label free images of the biological samples but also potentially provides quantitatively information of the samples [6, 8, 14, 22, 23]. THG signal can be enhanced by the presence of a multilayered structure, found in membranes and the lipid bodies [24](see Chapter 5). Moreover, the THG technique is enabling label free examination of the samples without photobleaching and photoxicity.

6.3 Lipid Bodies as indicators in cancer

During the last decade, LBs were drawn an increased attention by the scientific community. LBs are considered dynamic and functional organelles and seem to be involved in inflammation and cancer. Nowadays, there is a general consensus that cancer cells display metabolic reprogramming compared to healthy cells, related not only to mechanisms of ATP synthesis through glycolysis (Warburg effect) but also to de novo lipid synthesis, with fatty acid synthase (FASN) and sterol regulatory element-binding protein (SREBP) family as key players in many human cancers. Under physiological conditions, normal cells tend to maintain lipid levels under control, by regulating uptake, synthesis, and mobilization from internal storages. In contrast, tumor cells are able to uptake larger amount of lipids, as well as to enhance lipogenesis and CH production, and to increase FA β-oxidation [25–27].

6.4 Non-linear imaging of breast tissues

The goal of this study is to develop a novel system for determining, as an “imaging pen”, the malignant tissue limits intravitally during surgery. Thus, as a first approach, nonlinear microscopy was applied to breast cancer tissues collected from different patients.

Although various studies have shown the potential of label free nonlinear imaging for cancer research, this is the first time in the present study that THG microscopy was employed for the accurate imaging and quantification of the lipid content and inhomogeneities in breast cancer tissues. In particular, based on THG signal (mean lipid area, cell volume and intensity) we could evaluate the tumor state, the malignant or benign nature of the outgrowth, and further define the grade of cancerous tissue.

Multimodal nonlinear imaging is an emerging microscopy approach gaining widespread use in a

variety of biomedical applications. It harnesses and integrates the unique capabilities of nonlinear processes such as multiphoton fluorescence, second- and third-harmonic generation (SHG and THG) and combines them seamlessly into a single, unified microscopy platform. A combination of label-based (e.g. H&E staining) and label-free imaging modalities enables simultaneous acquisition of complementary structural information within individual cells and elucidates the health of biological tissue at the submicron level. Figure 6.1 depicts a multimodal nonlinear image of breast cancer tissue. With a single beam, without the need of any staining, multiple morphological information of the tissue can be obtained, including autofluorescent proteins (MPEF), inhomogeneities and LBs concentration (THG) and collagen distribution (SHG). It has to be mentioned that the detected autofluorescence signals is a combination of 2-photon and 3-photon excitation procedures. NADH (reduced form of nicotinamide adenine dinucleotide) elastin fibers and flavin adenine dinucleotide (FAD) are the main contributors to the recorded MPEF signals from the tissue [28]. Moreover, we can detect the cell nucleus in the tissue as the black area in the cells, which because of its homogeneity makes THG signal to achieve a destructive interference.

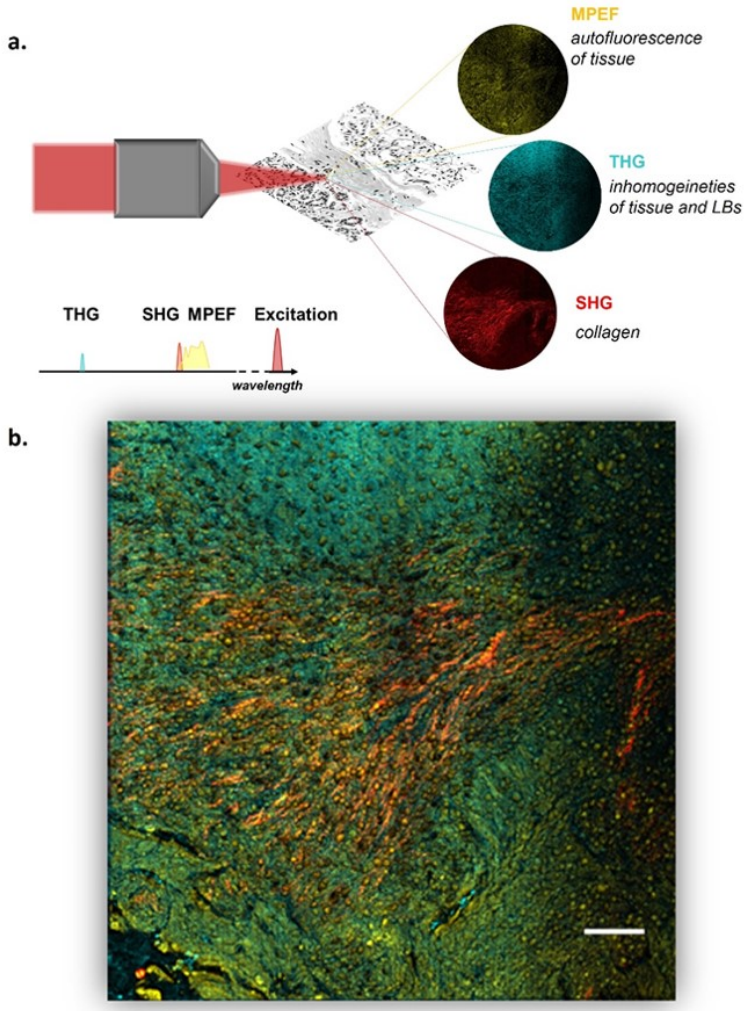

Figure 6.1: a) Schematic diagram of collecting multimodal nonlinear signal of breast tissue, b) Multimodal nonlinear image (MPEF, THG, SHG) . SHG (in red) indicates collagen ,THG (in cyan) reflects inhomogeneities of the sample and lipid droplets while MPEF (in yellow) distributes autofluorescence of the tissue. Scale bar depicts 100 μm.

Changes within the tissue concerning its surface, volume, the nucleus/cytoplasm ratio, shape and density, as well as structure and homogeneity are indicator for cancer [29]. Nonlinear imaging offers the capability to demonstrate tissue morphology (cells, nucleus, LBs and collagen) without the need of staining.

In this research, breast tissues from different patients (N=15) were obtained from the hospital university of Crete. The tissues tested were benign (control) and malignant, characterized to be at different grades (grade I, grade II, grade III), with a thickness of ~ 10 μm (see Table 6.1). The grade of a cancer is representative of the "aggressiveness" of the tumor, where a low grade is considered less aggressive than a high. The determination of grading from the pathologist is mainly based on three criteria. The tubule formation, which is the percent of normal duct structures within the tumor; the nuclear grade, which is the abnormality in size and shape of tumor cells compared to normal cells, giving a higher grade to cells that are larger, darker and more irregular than normal cells; and last but

Table 6.1: List of the investigated breast tissues

	Subtype	Grade
Cancer A1	ER+/PR+	Grade I (N=4)
Cancer A2	ER+/PR+	
Cancer A3	ER+/PR+	
Cancer A4	ER+/PR+	
Cancer B1	ER+/PR-	Grade II (N=5)
Cancer B2	ER+/PR-	
Cancer B3	ER+/PR-	
Cancer B4	ER+/PR+	
Cancer B5	ER+/PR+	
Cancer C1	ER+/PR+	Grade III (N=4)
Cancer C2	ER+/PR+	
Cancer C3	ER+/PR-	
Cancer C4	ER-/PR-	
Control 1	-	Normal (N=2)
Control 2	-	

not least, the mitotic rate, which is a measure of the rate of tumor cells growth and division.

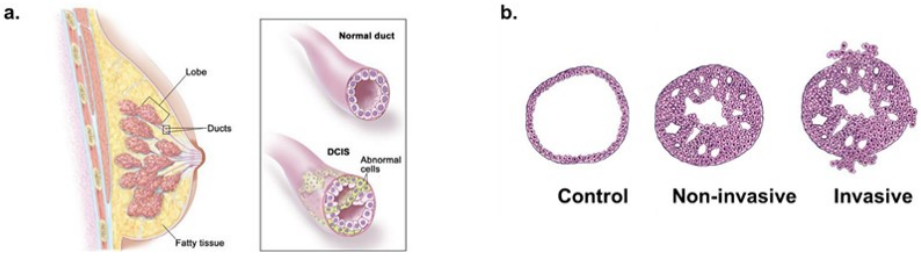

Figure 6.2: Illustration of human breast (a) and the different cases of ductal carcinoma in situ (b).[30]

In this study, most of the cancerous tissues were diagnosed from the pathologists as ductal carcinoma (Figure 6.2). Ductal carcinoma in situ (DCIS) is characterized by cancerous cells that are confined to the lining of the milk ducts and have not spread through the duct walls into surrounding breast tissue. If DCIS lesions are left untreated, over time cancer cells may break through the duct and spread to nearby tissue, becoming an invasive breast cancer [31].

Thus the present study included tissues from four patients in grade I and grade III, five patients in grade II and two control cases. Moreover, in each case, serial sections were submitted to H&E (Hematoxylin/Eosin) staining for additional evaluation of the tissues (Figure 6.3).

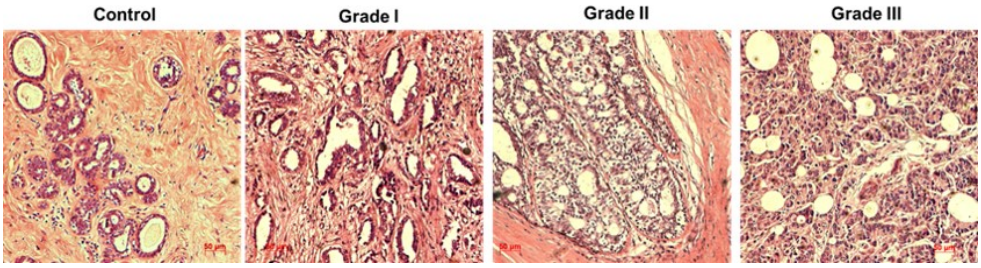

Figure 6.3: Characteristic H&E stained images of the investigated breast tissues

Figure 6.4 depicts the capability of nonlinear microscopy to visualize large areas of breast cancer tissue (grade II) approximately in the scale of millimeters. Moreover Figure 6.4c depicts the complementarity of nonlinear image -SHG in red and THG in cyan- to the H&E staining of the tissue section.

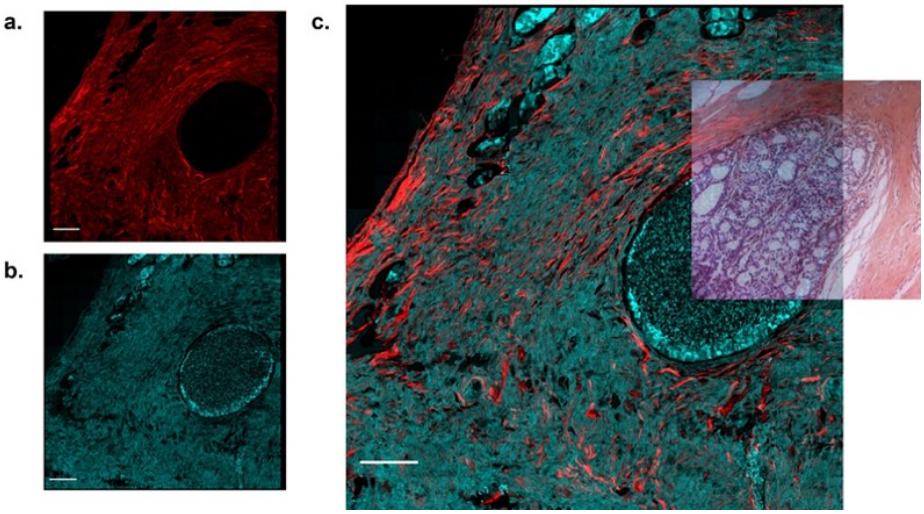

Figure 6.4: Nonlinear images (a. SHG, b. THG) of breast cancer tissue and the multimodal nonlinear image with the corresponding sequential tissue section image of H&E stained. Scale bars denotes 100 μm

Figure 6.5 demonstrates representative THG and SHG images and their corresponding H&E stained images (serial tissue sections) of control tissue samples, grade I, grade II and grade III. These characteristic nonlinear images show the cells, their intracellular organelles (mainly LBs) as well as inhomogeneities in the tissue through THG signal in cyan and collagen distribution and organization through SHG signal in red. In control tissues, the cells are oriented along with collagen and depict regular cell size and nucleus. Morphologically, the cancerous cell is characterized by a large nucleus, having an irregular size and shape, as depicted by THG images as well. Moreover, the collagen SHG signal in control tissues is higher as compared to malignant tissues. As tumor progresses, we can see cell proliferation with irregular nucleus and cell size as well as collagen degradation. The structural alterations of the collagen in the presence of malignancy has been investigated in numerous studies [32–34].

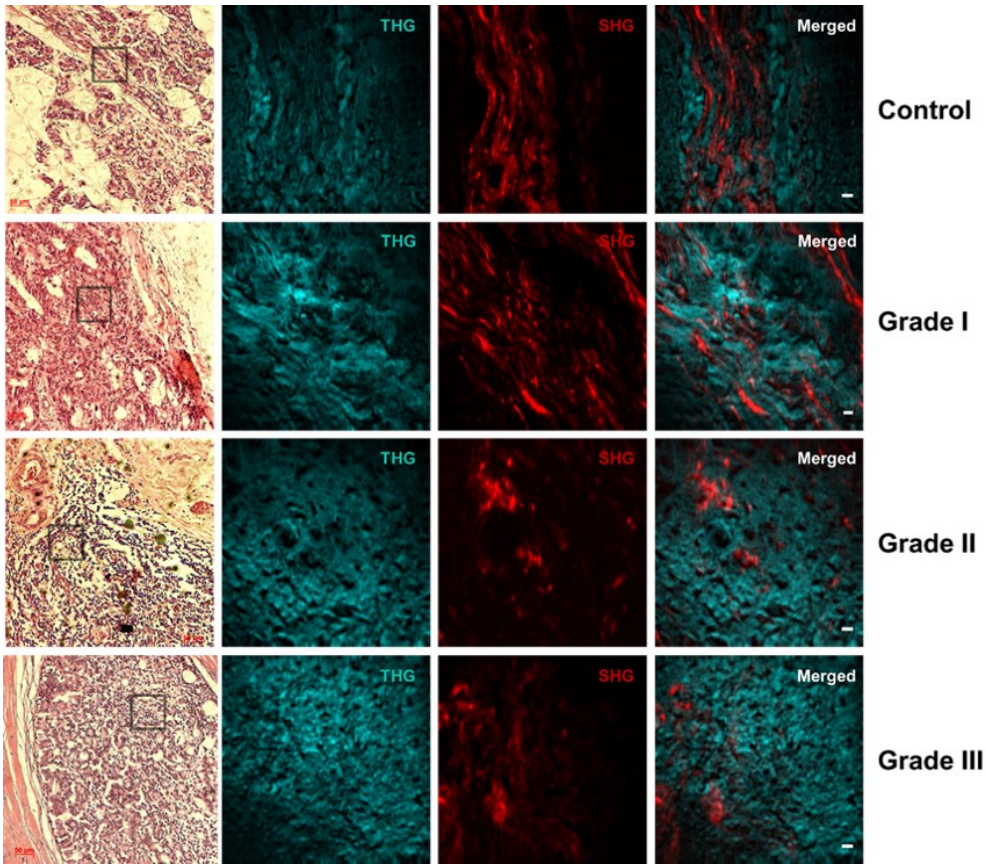

Figure 6.5: H&E images and the corresponding nonlinear images (SHG & THG) of benign and malignant (grade I, grade I , grade III) breast tissues. Characteristics THG images of tissues indicate LBs and inhomogeneities and SHG images collagen. Scale bar of nonlinear images depicts 5 μm. The squares in H&E images indicate the regions that were scanned via the performance of nonlinear imaging measurements.

6.5 Calculation of nuclear to cytoplasmic ratio

Because of the heterogeneous nature of breast tissue classification using cytomorphology and biological markers have been attempted to predict the behavior of the different lesions so far. Irregularities in both nuclear shape and size ('pleomorphism'), coupled with changes in chromatin amount and distribution, remain the basic microscopic criteria for a cytologic diagnosis of cancer [35]. In this study, THG utility can provide new insights and offer numerical analysis of the nuclear to cytoplasmic ratio (N/C ratio) that is an indicator of cancer prognosis for pathologists. Appendix B presents in detail the individual cell detection and isolation from the tissues via the performance of THG measurements.

Irregular nuclei, increased N/C ratio and conspicuous single prominent nucleoli were depicted in cases of cancerous tissues by utilizing THG imaging (Figure 6.6). In particular, the cells in lower grade showed moderate variation in nuclear size and shape. On the other hand, the cells in higher grades indicated variation in nuclear size and shape (pleomorphism) with a high nuclear- cytoplasmic ratio (N/C).

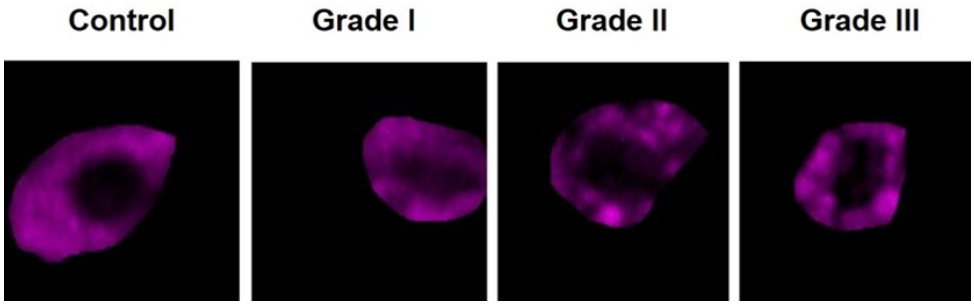

Figure 6.6: Morphological characteristics of the cell in benign and cancerous tissues respectively via THG imaging.

Morphologically, the cancerous cell is characterized by a large nucleus, having an irregular size and shape, the nucleoli are prominent and the cytoplasm area is reduced. The nucleus of neoplastic cells plays through its changes a main role in the assessment of tumor malignancy. Changes concern its surface, volume, the nucleus/cytoplasm ratio, shape and density, as well as structure and homogeneity. Figure 6.7 depicts irregularities of nuclear that detected via THG imaging in characteristic cells of cancerous tissues [29]. In addition, THG measurements of cells can offer precise images of the nucleoli due to the presence of an interface between nucleus and nucleoli (inhomogeneity) (Figure 6.8).

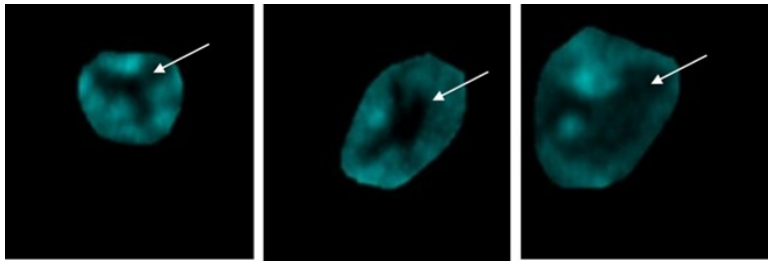

Figure 6.7: THG images of cancerous tissues. Arrows depict the irregular nuclear (distributed as black area) of cells.

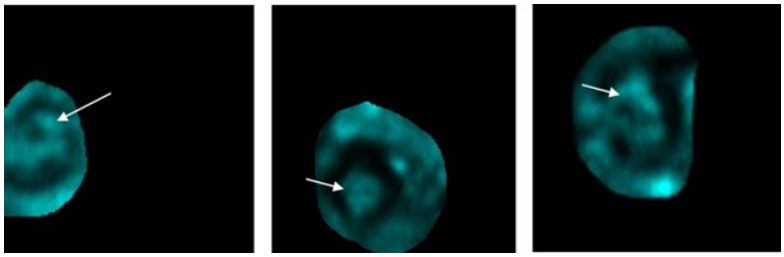

Figure 6.8: THG images of cells in cancerous tissues. Arrows depict the nucleoli located in nuclear area (interface of nucleus and nucleoli).

Moreover, THG utility can offer structural information about the nuclear/cytoplasmatic ratio that is an indicator of cancer prognosis for pathologists. Nuclear morphometry successfully differentiates benign from malignant tissues and grading the different cancerous cases [36].

Following morphometric features of the cells, it was calculated based on THG signals, the mean nuclear area (MCA), mean cytoplasmic area (MCA) and the nucleus to cytoplasmic ratio (N/C ratio)

respectively (Table 6.2). The results showed increased values of N/C ratio as increasing the grade of cancer (Figure 6.9) with significant statistically differences. These results are in agreement with previous related studies [37].

Table 6.2: Comparison of mean nuclear area (MNA) , mean cytoplasmic area (MCA) and mean nuclear to cytoplasmic ration (N/C ratio) in the various categories (N=150 cells for each case)

Category)	Number of cases	MNA±SEM (μm^2)	MCA±SEM (μm^2)	N/C ratio±SEM
Control	2	82.54 ± 0.67	267.47 ± 0.67	0.254 ± 0.005
Grade I	4	58.82 ± 0.47	161.38 ± 1.30	0.352 ± 0.003
Grade II	5	77.35 ± 1.51	186.62 ± 0.62	0.392 ± 0.002
Grade III	4	64.11 ± 0.52	145.32 ± 1.17	0.443 ± 0.002

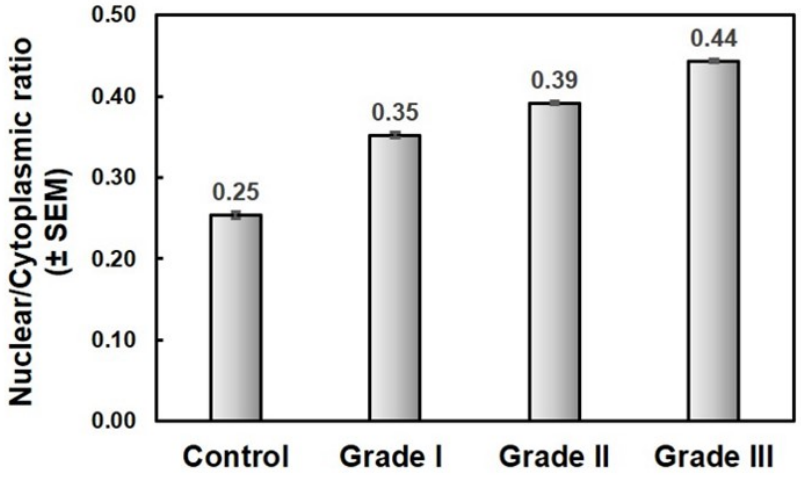

Figure 6.9: Calculation of N/C ratio of cells in benign (control) and cancerous tissues (grade I,II, III).

6.6 Quantification analysis

Except of the morphologically evaluation of the unstained tissues offered by the THG modality, THG also enables potentially quantitative information on the investigated tissues. In this study, nonlinear images could provide further details related with THG signal area, THG signal intensity and also the volume of each cell in the tissue.

As an initial step, after setting a constant threshold, cell detection and isolation was separately handled in order to perform quantification analysis (Figure 6.10). The identification was manually acquired using the Image J program. After isolating the cells from each tissue, these were then submitted to quantification processing. In this study, the cell volume, the mean THG signal area of each cell and the mean THG intensity signal of the tissue area, were calculated.

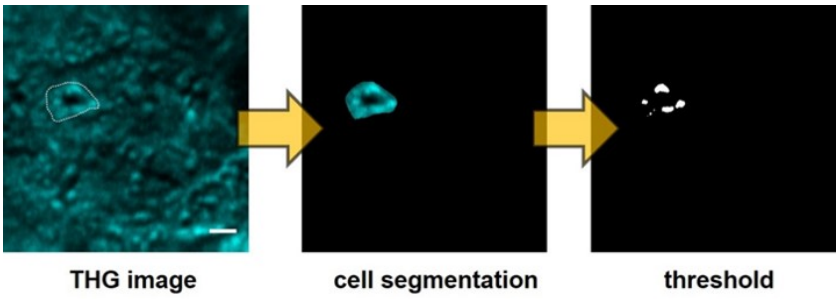

Figure 6.10: Illustration of THG tissue processing. The isolation of individual cells for quantification analysis (based on their LBs, membranes and inhomogeneities). Scale bar depicts 5 μm

THG signal area that represents the amount of LBs and inhomogeneities in the tissue was shown to differ in benign and malignant tissues (Figure 6.11a). In particular, the cells from control tissues depicted significant lower values of THG signal are as compared to cells of cancerous tissues. Moreover, B1 and C3 tissues that belong to subtype ER+/PR- showed higher values as compared to the other tissues. When pooling the results of the different samples following their grade, a significant linear increase of THG signal area could be detected along with cancer progression (higher grades) (Figure 6.11b).

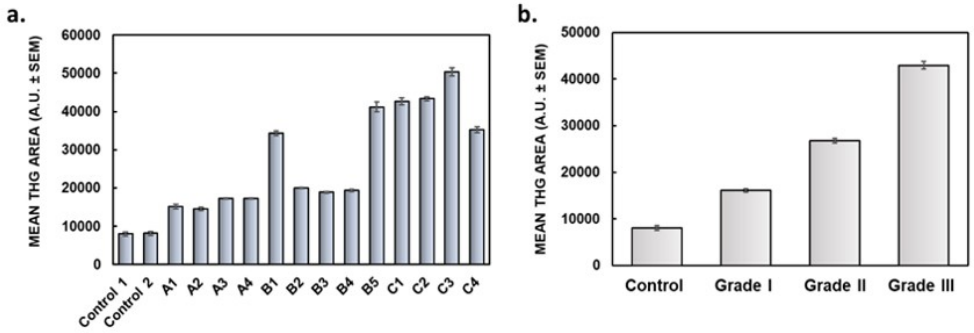

Figure 6.11: Quantification of THG signal area of breast tissues (N=40 cells of each tissue)

In addition, the calculation of cell volume in the different tissues showed that cancer cells displayed increased volume as compared to cells in control tissues. In addition, samples in grade III presented high deviations of the cell volume, also indicating the dissimilarity of the cells in case of a progressive cancer (Figure 6.12).

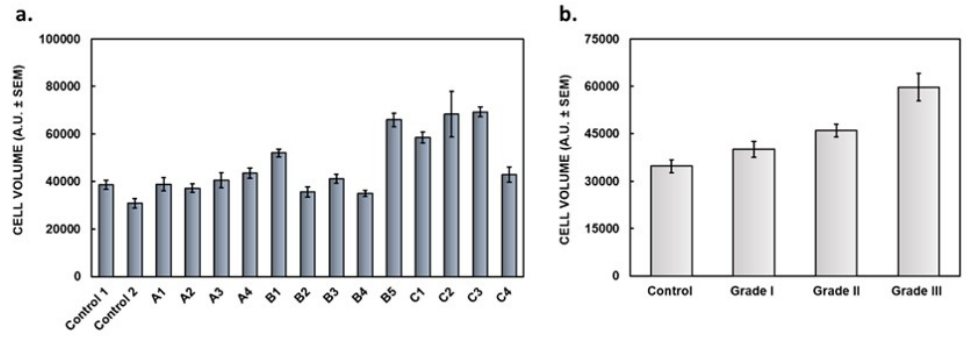

Figure 6.12: Quantification of cell volume (N=40 cells of each tissue)

When the number of THG signal area of each cell was divided by the respective cell volume (normalization by dividing the mean total area by the cell volume of each cell), significant difference between the cells of control and cancer tissues was detected (Figure 6.13). In particular, the cells in C4 tissue sample presented statistically significant higher values that may be connected to the profile of aggressiveness (ER-/PR-). Such analysis that takes into consideration the cell volume, confirms that independently of the cell volume, there is an increase of THG signal area.

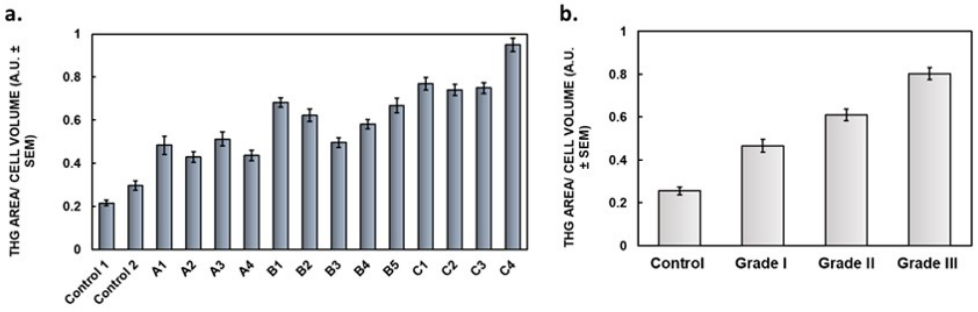

Figure 6.13: Quantification of mean THG signal area divided with cell volume (N=40 cells of each tissue)

Moreover, it is apparent from the data presented in Figure 6.14 that control tissues can be differentiated from breast cancer tissues, based on THG signal intensity. It has to be noted that in this analysis the quantification was based on the total area of the tissue but not in particular cells as previously shown, therefore a higher deviation between the same grade of tissues was observed.

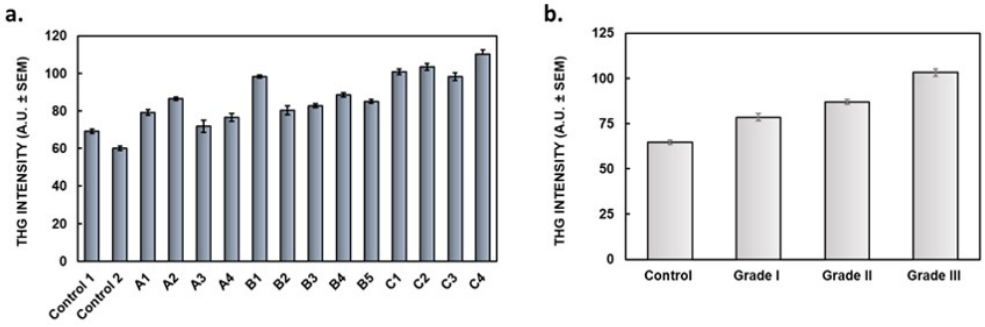

Figure 6.14: Quantification of THG signal intensity (N=40 cells from each tissue).

Summarizing the obtained results concerning mean THG signal area, mean THG area divided by the cell volume and THG intensity for N=40 cells of a characteristic tissue of each grade, it can be easily seen that THG undoubtedly enables discrimination of the different sample categories (Figure 6.15).

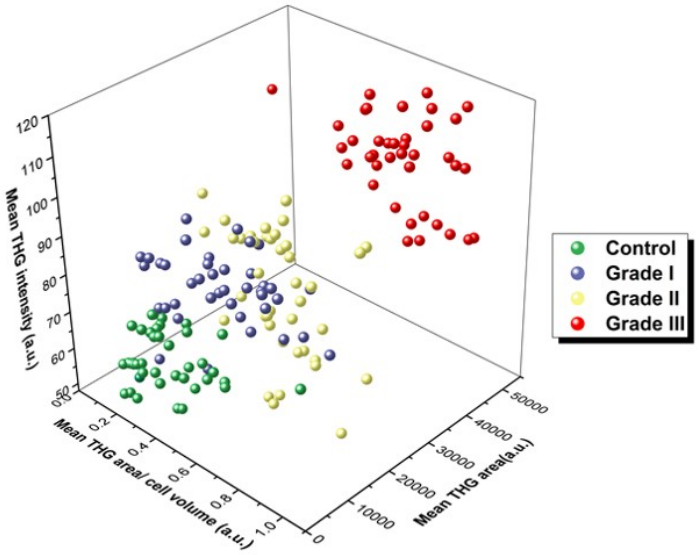

Figure 6.15: 3D graph for the distinction between cancerous and control tissues via THG signals quantification. THG area/ cell volume area of the cell in x-axis, THG intensity values in y-axis and mean THG area in z- axis. The grade III cancer tissue and the control tissue appeared clearly as separable sub populations of spots in the scatter plot (N=40 for each tissue type).

Such analysis could also be applied to follow up the progression of breast cancer in a patient. In this study, tissues C3 and control 1 are from the same patient in control and cancerous (grade III) states respectively. Comparing these tissues, it can be seen that cells of the different tissues can be easily discriminated (Figure 6.16).

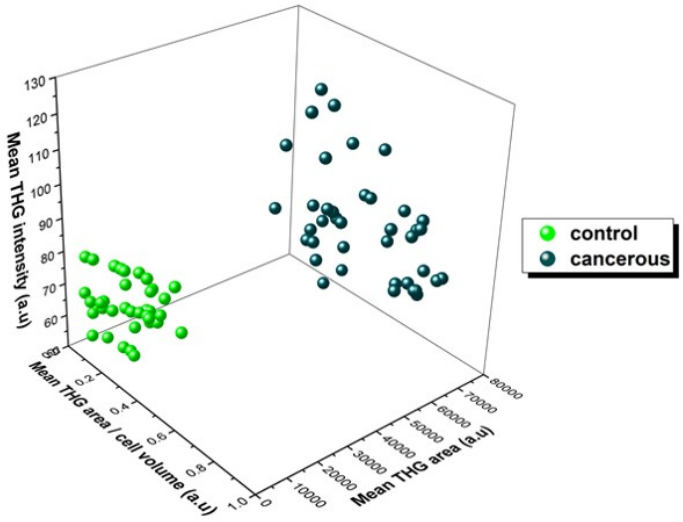

Figure 6.16: 3D graph for the distinction between cancerous and control area tissues of a patient via THG signals quantification. THG area/ cell volume area of the cell in x-axis, THG intensity values in y-axis and mean THG area in z- axis. N=40 cells for each tissue.

By the same token, A4 and B3 samples represent the progression of grade I to grade II in the same patient. In this analysis, there is a relevant discrimination of the grades but not significant between the samples (Figure 6.17).

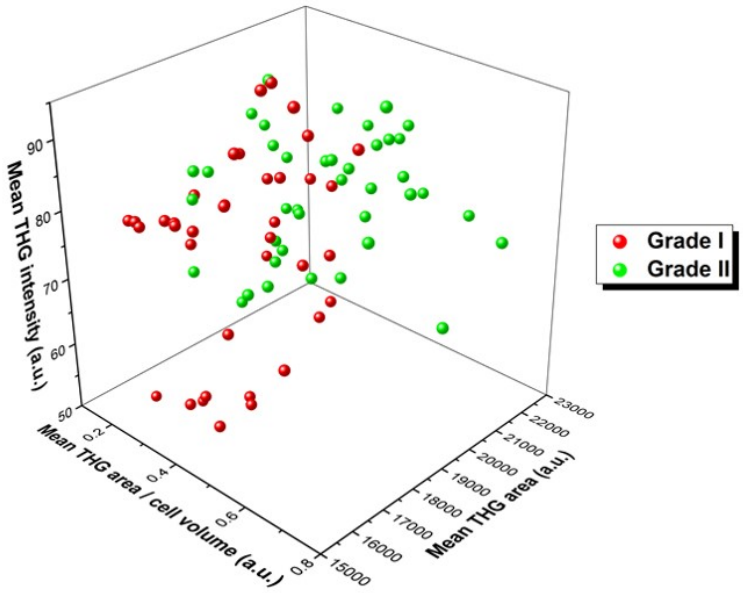

Figure 6.17: 3D graph for the distinction between cancerous and control tissues of same patient via THG signals quantification. THG area/ cell volume area of the cell in x-axis, THG intensity values in y-axis and mean THG area in z- axis. N=40 cells for each tissue.

In addition, THG signal analysis could gauge the number of cells that were detected in the scanned region of each tissue section. Thus, in a scanning region (45 μm $\times$ 45 μm) of almost 0.002 mm^2, $\sim$ 7 cells could be detected in control tissues, $\sim$ 13 cells in grade I tissues, $\sim$ 21 cells in grade II tissues

and $\sim$ 40 cells tissues in grade III tissues.

Finally, in the elucidation of cancer cells included in a tissue and the estimation of the percentage of control cells in malignant tissues was carried out. Based on THG signal area and cell volume, we could evaluate the percentage of control cells in the cancerous tissues. The output of this analysis indicates that for the examined tissues, in 0,1 mm^2 area, grade I samples included of 39% of control cells, grade II comprised 24% control cells, while grade III samples showed 23% of control cells. This result implies that for greater grades of cancerous tissues, cancer cell proliferation is increasing, while the amount of control cells is decreased.

6.7 FTIR spectroscopy in breast tissues

FTIR spectroscopy has proved to be a powerful tool for the study of biological molecules and the application of this technique to biological systems is continually expanding. Biological elements, including lipids, proteins, peptides, biomembranes, nucleic acids, tissues and clinical samples, have all been successfully studied by using infrared spectroscopy. This technique, within the last decade has rapidly given rise in the number of studies of more complex systems, such as breast cancer tissues [38–43].

Previously we employed FTIR spectrometer to examine breast cancer cell lines. In this chapter, FTIR spectra were acquired in two different configurations, namely absorption and attenuated total reflection (ATR). The tissue samples were deposited on infrared transparent windows of barium fluoride. Initially, absorbance spectra measurements of the total tissue region were recorded by using Bruker Vertex 70v FT-IR spectrometer. In this case, spectra analysis did not indicate any significant difference between the tissues. Therefore, the samples were then analyzed using a Bruker HYPERION 2000 FT-IR microscope which is attached in a Bruker Vertex 70V FTIR spectrometer and provides the possibility to collect spectra at specific regions of the tissue ($\sim$ 50 μm).

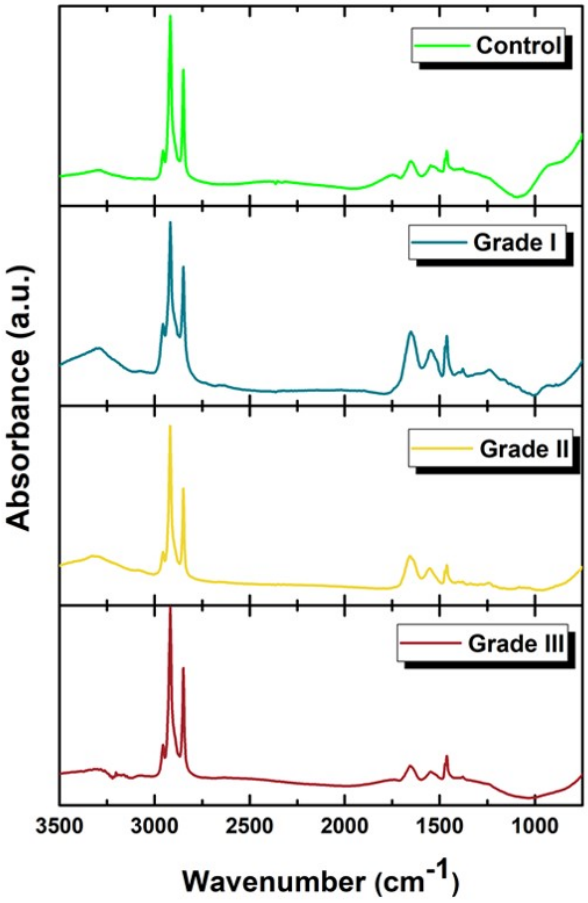

Figure 6.18: Stack graphs of characteristic FTIR spectra of breast tissues.

By using the FTIR microscope with an IR source, it was possible to focus in specific cancerous areas of the sample and acquire the absorbance only from the specific tissue region (Figure 6.18). However, due to tissue heterogeneity, each sample revealed a specific spectra fingerprint, and therefore no significant differences could be obtained. For this reason, quantification analysis calculated FTIR spectra, revealing the concentration of the chemical compounds. To quantitate the differences between control and cancerous tissues, integration of FTIR spectra was carried out focusing in lipid regions (Table 6.3). From each sample tested, an average the spectra of N=15 different regions was obtained. In addition, for each category of the cancer tissues investigated herein, samples from 2 patients (N=2) were analyzed. The results showed that cancer tissues displayed higher concentration of lipid compounds in 1085 cm^{-1} (membrane phospholipids, amide III), 1399 cm^{-1} (vibrational modes of methyl and methylene groups of proteins and lipids and amide groups) , 1469 cm^{-1} (CH_2 bending of the acyl chains of lipids), 1646 cm^{-1}, 1653 cm^{-1}, 1736 cm^{-1},1750 cm^{-1} (1600-1800 cm^{-1} C=O stretching of lipids), 2848 cm^{-1} (Stretching vibrations of CH_2 & CH_3 of phospholipids and cholesterol), 2873 cm^{-1} (Symmetric stretching vibration of CH_3 of acyl chains (lipids)), 2916 cm^{-1} (Stretching vibrations of CH_2 & CH_3 of phospholipids, cholesterol) and 2956 cm^{-1} (asymmetric stretching vibration of CH_3 of acyl chains (lipids)).

Table 6.3: Integrated FTIR spectra *The integrated spectra peak area depicts the concentration of chemical bonds of lipids for control, Grade I, Grade II and Grade III tissue samples.*

Wavenumber (cm^{-1})	**Description**	**Control**	**Grade I**	**Grade II**	**Grade III**
1085	Mainly from membrane phospholipids (amide III).	0.016	0.025	0.036	0.027
1399	CH_2 wagging vibration of the acyl chains (phospho-lipids)	0.028	0.036	0.063	0.029
1469	CH_2 bending of the acyl chains of lipids	0.322	0.529	0.540	0.550
1646	C=O stretching (lipids)	0.004	0.006	0.006	0.006
1653	C=O stretching (lipids)	0.011	0.015	0.023	0.023
1736	C=O stretching (lipids)	0.013	0.018	0.028	0.024
1750	C=O stretching (lipids)	0.025	0.028	0.031	0.032
2848	Stretching vibrations of CH_2 & CH_3 of phospho-lipids, cholesterol	7.903	9.952	11.270	10.250
2873	Symmetric stretching vi-bration of CH_3 of acyl chains (lipids)	0.008	0.032	0.0097	0.024
2916	Stretching vibrations of CH_2 & CH_3 of phospho-lipids, cholesterol	15.441	18.979	23.237	17.992

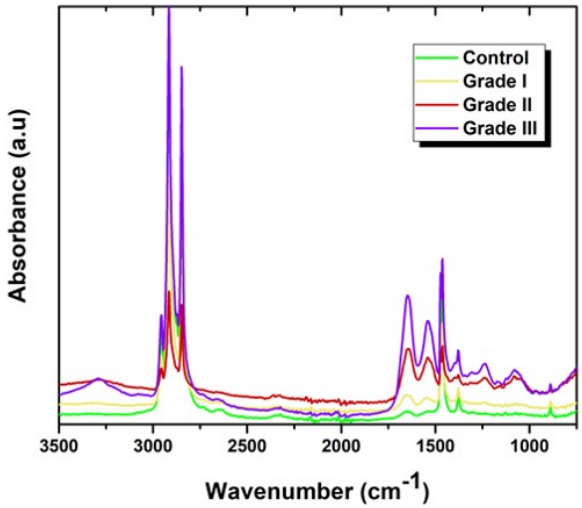

Figure 6.19: Characteristic ATR spectra of breast tissues (control and cancerous). One representative area for each tissue is shown (N=2 patients for each state of tissue).

Platinum ATR unit with a single reflection diamond crystal. ATR spectroscopy could provide information at the tissue surface ($\sim 2\ \mu$m). Figure 6.19 depicts a characteristic spectrum from each tissue. First, spectra measured in reflectance mode were converted using the Beer – Lamberts law to

absorbance. Comparing ATR spectra from control and cancerous tissues it was shown that controls displayed lower amplitude of absorbance than cancerous samples. However, except from the absorbance amplitude, no significant differences were recorded. For this reason, integration of ATR spectra could provide a quantitative evaluation of particular chemical bonds, which correspond to specific chemical compounds (Table 6.4). The obtained results of this analysis showed that only minimal changes could be depicted between control and cancerous tissues, mainly in 1063 cm^{-1} (C-O-C stretching of phospholipids), 1085 cm^{-1} & 1237 cm^{-1} (membrane phospholipids, amide III) , 1646 & 1653 cm^{-1} (C=O stretching of lipids), and 2873 cm^{-1} (Symmetric stretching vibration of CH_3 of acyl chains (lipids). Interestingly, the results obtained from the integrated areas (lipid compounds) of both ATR and FTIR microscopy analysis showed some common peaks and quite similar differences between control and cancerous tissues at 1085 cm^{-1}, 1646 cm^{-1} , 1653 cm^{-1} and 2873 cm^{-1}.

Table 6.4: Integrated ATR spectra

Wavenumber (cm^{-1})	**Description**	**Control**	**Grade I**	**Grade II**	**Grade III**
1063	C-O-C stretching (phospholipids).	0.003333	0.003667	0.009333	0.004
1085	Mainly from membrane phospholipids (amide III).	0.009	0.009333	0.017778	0.012667
1237	C-O-C stretching (phospholipids).	0.039333	0.045	0.041667	0.0515
1646	C=O stretching (lipids)	0.660167	0.775333	0.962444	1.4285
1653	C=O stretching (lipids)	0.002	0.002333	0.003889	0.004333
2873	Symmetric stretching vibration of CH_3 of acyl chains (lipids)	0.004667	0.008667	0.006556	0.007167

In order to obtain supplementary information on the tissues, 2nd derivative analysis of ATR spectra was applied (Figure 6.20). Such calculation showed minimal differences in the lipid regions of grade III samples, as compared to the rest of the tissues (Table 6.5). Particular differences were observed at 1453cm^{-1} CH_3 bending vibration (lipids and proteins), 2846 cm^{-1} stretching vibrations of CH_2 & CH_3 of phospholipids & cholesterol, 2857 cm^{-1} (asymmetric CH_2 stretching mode of the methylene chains in membrane lipids), 2872 cm^{-1} (symmetric stretching vibration of CH_3 of acyl chains (lipids)), 2915 cm^{-1} (Stretching vibrations of CH_2 & CH_3 of phospholipids, cholesterol), 2926 cm^{-1} (v_{as} CH_2 lipids) and 2957cm^{-1} (v_{as} CH_3 lipids). However, this method lacks of specificity because ATR spectrometer provides mainly information of the surface of the tissue (around 2 μm), as compared to the corresponding spectra region which extends to some milimeters. In contrast FTIR microspectroscopy provides the capability to scan smaller tissue regions.

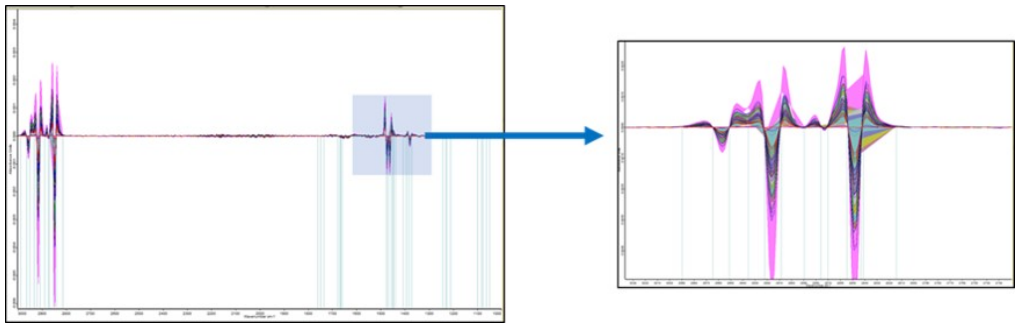

Figure 6.20: 2nd derivative integrated area of ATR characteristic spectra.

Table 6.5: Integrated 2nd derivative ATR spectra

Wavenumber (cm^{-1})	**Description**	**Control**	**Grade I**	**Grade II**	**Grade III**
1453	CH_3 bending vibration (lipids and proteins).	0.0005	0.0005	0.0001	0.0008
2846	stretching vibrations of CH_2 & CH_3 of phospholipids & cholesterol	0.02267	0.01683	0.01283	0.02617
2857	asymmetric CH_2 stretching mode of the methylene chains in membrane lipids	0.004667	0.003833	0.0030	0.005667
2872	symmetric stretching vibration of CH_3 of acyl chains (lipids)	0	0	0	0.00167
2915	Stretching vibrations of CH_2 & CH_3 of phospholipids, cholesterol	0.015	0.012	0.009	0.018
2926	v_{as} CH_2 lipids	0.0040	0.0033	0.0027	0.0052
2957	v_{as} CH_2 lipids	0.0028	0.002	0.0015	0.0033

6.8 Correlation of THG signal with FTIR spectra

Many studies have dealt with cancer cells and their need for large amounts of lipids used for cellular membrane generation due to high cell proliferation rates [44]. The previous analysis of THG signal area that is mainly originated from LBs showed that LBs could differentiate control from cancerous tissues and that tumor progression correlated with THG signal area increase. Since a significant contribution to the calculated THG signal area arising from LBs, it was then attempted to define the lipid compounds in the THG area by correlating THG area signal to FTIR integrated data. Because of breast cancer heterogeneity, such analysis focused only on lipids bonds specified in peaks 1399 cm^{-1}, 1469 cm^{-1}, 1736 cm^{-1}, 1750 cm^{-1}, 2873 cm^{-1} and 2956 cm^{-1}.

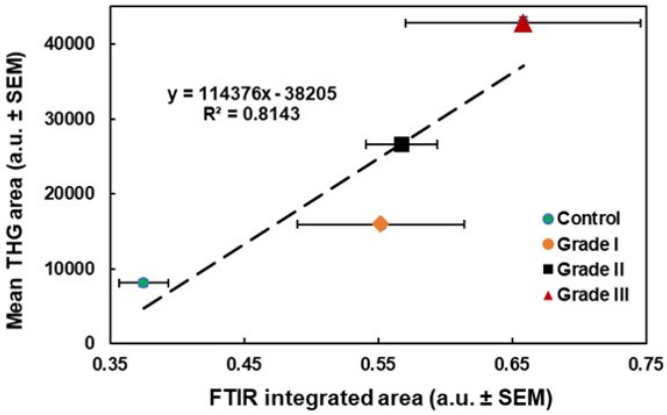

Figure 6.21: Correlation of FTIR spectra correlated with mean THG area in specific lipid bonds.

Indeed, the results of such analysis indicated that there is a significant correlation between the mean THG signal area and the integrated FTIR spectra of lipid compounds (R^2 ∼0.81) (Figure 6.21).

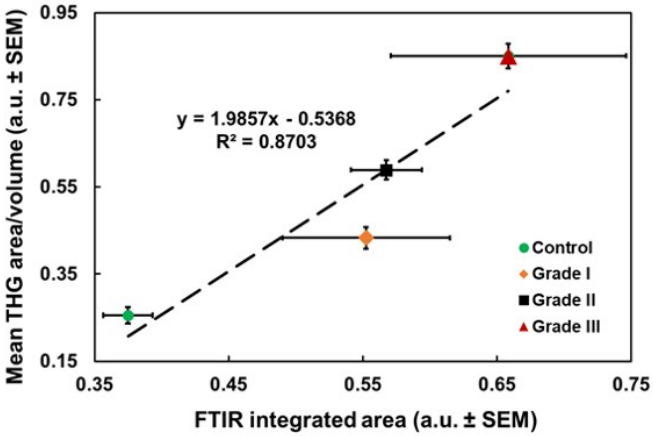

Figure 6.22: Correlation of FTIR spectra with mean THG area divided by cell volume in specific lipid bonds.

Additionally, when the relation of cell volume with the integrated FTIR spectra of lipid compounds was examined, a significant correlation was also detected (R^2 ∼0.87) (Figure 6.22).

6.9 Conclusion

Cancer is a disease caused by a combination of genetic and environmental factors. Currently, most types of cancer are recognized when a tumor mass develops and becomes palpable by feel. However, recent advances in imaging and screening methods have led to the earlier detection of cancer, which may lead to more effective therapy, significantly reducing the morbidity and mortality rates. Early detection is one of the most important strategies to improve breast cancer survival, since it gives for choosing the appropriate therapy and in case of surgery secures the margins of the malignant tissue

for safe removal. The diagnosis of cancer patients relies on the accuracy of the detection of cancerous sites in the body.

Determining the malignancy of a tumor using the established diagnosis protocols can take several weeks because it includes visits to an oncologist, obtaining a tissue sample (biopsy), and further histopathological analysis of the biopsied material. A late or missed diagnosis of a primary cancerous tumor increases the chances that cancer cells will enter the blood circulation, where a single cancer cell may lead to a secondary tumor; this significantly lowers the patient's survival. There are two primary risks associated with the above-described diagnosis protocol that increase the probability of metastasis. First, if a patient has a malignant tumor at the time the tumor is diagnosed, the tumor may grow into a blood vessel and cancer cells may be released into the blood circulation. Secondly, there is a risk associated with the invasiveness of biopsy; during a surgical cut or puncture, parts of biopsied tissue can come into direct contact with a blood vessel.

In cancer diagnosis, there is a growing need for the development of a multimodal imaging based diagnostic tool, to objectively evaluate morphological features with subcellular resolution, and molecular compositions that are closely associated with tumor malignancy. Under this perspective, NLO microscopy was proven to be useful in cancer research. These techniques have emerged as a valuable tool for high□resolution, nondestructive imaging of tumors. Following the need for novel non-destructive techniques in diagnosis of breast cancer, nonlinear optical imaging and FTIR spectroscopy were carried out to differentiate cancerous of benign tissues. Nonlinear optical modalities such as SHG, THG and MPEF provide unique morphologically information of the tissues, such as collagen (SHG), intracellular structures and inhomogeneities (THG) and autofluorescence proteins (MPEF) with a single fs laser beam. In this research, THG imaging modality was used to quantify further differences between benign and malignant tissues. The THG imaging method provides unique capabilities over other techniques, since it offers visualization of intracellular structures (LBs) and inhomogeneities without the need of staining. Quantification analysis of THG signals classified the identified regions as normal or cancerous and discriminated the malignant areas into different cancer grades, based on their inhomogeneities and LBs content. Complementary FTIR spectra could correlate specific chemical information of the different tissues. FTIR analysis showed an increased lipid content during cancer progression. In addition, 2nd derivative analysis of ATR spectra revealed an increased lipid content of grade III tissues. Correlating the findings of FTIR measurements with mean THG signal area, the linear regression analysis showed perfect agreement with the increased LB profile during tumor progression. The data presented here are complementary of existing clinical diagnostic approaches and can be used as a procedure to confirm the disease and evaluate its severity and treatment efficacy.

NLO images provided comparable results to standard H&E staining and enabled the evaluation of cell size, cell shape, nuclear shape and intracellular organelles (LBs) without any staining preparation. This technology was proved sensitive to detect cancer cells in tissues and could aid the surgeon to precisely excise as an "imaging pen" the unhealthy or precancerous margins of malignant lesion in order to minimize recurrence. The current scope of in vivo NLOM would be to determine the requirement or the best location of an invasive biopsy on a suspect region, rather than to provide an accurate pathology diagnosis. Moreover, this would help in reducing the number of unnecessary invasive biopsies considerably benefitting the patient and the pathologist.

In conclusion, the sensitivity and specificity of nonlinear optical imaging based diagnosis is compared to conventional histopathology. The deeper penetration of the tumor with nonlinear microscopy as compared to other techniques (e.g. confocal microscopy) provides three-dimensional imaging and function deep within the tumor, which could result in new types of therapeutics for tumor biology. The implementation of this study could be applicable to clinical diagnostic and could be supplement hitherto existing diagnostic techniques. Automated detection of clinically meaningful malignant regions of interest is an essential step for diagnosis. More broadly, research is also needed to develop a machine learning algorithm that will be able to predict automatically cancer cells in tissues based on cell volume, THG area and intensity signal and therefore, categorize the grade of cancer tissue.

Bibliography

[1] Ahmed M. Kabel. “Tumor markers of breast cancer: New prospectives”. In: *Journal of Oncological Sciences* 3.1 (2017), pp. 5–11. doi: https://doi.org/10.1016/j.jons.2017.01.001. url: http://www.sciencedirect.com/science/article/pii/S2452336416300395.

[2] Bruna Karina Banin Hirata et al. “Molecular Markers for Breast Cancer: Prediction on Tumor Behavior”. In: *Disease Markers* 2014 (2014), p. 12. doi: 10.1155/2014/513158. url: http://dx.doi.org/10.1155/2014/513158.

[3] A. L. Mota et al. “Molecular characterization of breast cancer cell lines by clinical immunohistochemical markers”. In: *Oncol Lett* 13.6 (2017), pp. 4708–4712. doi: 10.3892/ol.2017.6093.

[4] Jeffrey S Ross et al. “Breast cancer biomarkers and molecular medicine”. In: *Expert review of molecular diagnostics* 3.5 (2003), pp. 573–585. issn: 1473-7159.

[5] Vineeta Singh et al. “New diagnostic techniques for breast cancer detection”. In: *Future Oncology* 4.4 (2008), pp. 501–513. doi: 10.2217/14796694.4.4.501. url: https://www.futuremedicine.com/doi/abs/10.2217/14796694.4.4.501.

[6] J. Adur et al. “Quantitative changes in human epithelial cancers and osteogenesis imperfecta disease detected using nonlinear multicontrast microscopy”. In: *Journal of Biomedical Optics* 17.8 (2012). issn: 1083-3668. doi: 10.1117/1.jbo.17.8.081407. url: %3CGo%20to%20ISI%3E://WOS:000309696800017.

[7] S. Chen et al. “Virtual Biopsy of Human Skin by Using Noninvasive Higher Harmonic Generation Microscopy”. In: *IEEE Journal of Selected Topics in Quantum Electronics* 16.3 (2010), pp. 478–492. issn: 1077-260X. doi: 10.1109/JSTQE.2009.2031987.

[8] Evangelia Gavgiotaki et al. “THG imaging of lipid body profiles in diagnosis of biological samples”. In: *Medical Research Archives* 4.7 (2016).

[9] Michael G Giacomelli et al. “Multiscale nonlinear microscopy and widefield white light imaging enables rapid histological imaging of surgical specimen margins”. In: *Biomedical optics express* 9.5 (2018), pp. 2457–2475. issn: 2156-7085.

[10] K. Harpel et al. “Imaging of targeted lipid microbubbles to detect cancer cells using third harmonic generation microscopy”. In: *Biomedical Optics Express* 7.7 (2016), pp. 2849–2859. issn: 2156-7085. doi: 10.1364/boe.7.002849. url: %3CGo%20to%20ISI%3E://WOS:000379758400033.

[11] N. V. Kuzmin et al. “Third harmonic generation imaging for fast, label-free pathology of human brain tumors”. In: *Biomedical Optics Express* 7.5 (2016), pp. 1889–1904. doi: 10.1364/BOE.7.001889. url: http://www.osapublishing.org/boe/abstract.cfm?URI=boe-7-5-1889.

[12] P. P. Provenzano et al. “Nonlinear Optical Imaging of Cellular Processes in Breast Cancer”. In: *Microscopy and Microanalysis* 14.6 (2008), pp. 532–548. issn: 1431-9276. doi: 10.1017/s1431927608080884. url: %3CGo%20to%20ISI%3E://WOS:000261164800007.

[13] Chi-Kuang Sun. “Noninvasive Histopathological Imaging by Using Harmonic Generation Microscopy for Onsite Differential Diagnosis and Treatment Assessment”. In: *Biophotonics Congress: Biomedical Optics Congress 2018 (Microscopy/Translational/Brain/OTS)*. OSA Technical Digest. Optical Society of America, MF4A.1. doi: 10.1364/MICROSCOPY.2018.MF4A.1.

[14] P. C. Wu et al. “In vivo quantification of the structural changes of collagens in a melanoma microenvironment with second and third harmonic generation microscopy”. In: *Sci Rep* 5 (2015), p. 8879. doi: 10.1038/srep08879.

[15] L. H. Li et al. “Visualization of Tumor Response to Neoadjuvant Therapy for Rectal Carcinoma by Nonlinear Optical Imaging”. In: *Ieee Journal of Selected Topics in Quantum Electronics* 22.3 (2016). issn: 1077-260X. doi: 10.1109/jstqe.2015.2456108. url: %3CGo%20to%20ISI%3E://WOS:000361206600001.

[16] L. H. Li et al. “Monitoring neoadjuvant therapy responses in rectal cancer using multimodal nonlinear optical microscopy”. In: *Oncotarget* 8.63 (2017), pp. 107323–107333. issn: 1949-2553. doi: 10.18632/oncotarget.22366. url: %3CGo%20to%20ISI%3E://WOS:000419534900110.

[17] Y. K. Tao et al. “Assessment of breast pathologies using nonlinear microscopy”. In: *Proceedings of the National Academy of Sciences of the United States of America* 111.43 (2014), pp. 15304–15309. issn: 0027-8424. doi: 10.1073/pnas.1416955111. url: %3CGo%20to%20ISI%3E://WOS:000343729500028.

[18] Tadayuki Yoshitake et al. “Rapid histopathological imaging of skin and breast cancer surgical specimens using immersion microscopy with ultraviolet surface excitation”. In: *Scientific Reports* 8.1 (2018), p. 4476. issn: 2045-2322. doi: 10.1038/s41598-018-22264-2. url: https://doi.org/10.1038/s41598-018-22264-2.

[19] Danielle Tokarz et al. “Intravital imaging of osteocytes in mouse calvaria using third harmonic generation microscopy”. In: *PLOS ONE* 12.10 (2017), e0186846. doi: 10.1371/journal.pone.0186846. url: https://doi.org/10.1371/journal.pone.0186846.

[20] Bettina Weigelin, Gert-Jan Bakker, and Peter Friedl. “Intravital third harmonic generation microscopy of collective melanoma cell invasion”. In: *IntraVital* 1.1 (2012), pp. 32–43. issn: null. doi: 10.4161/intv.21223. url: https://doi.org/10.4161/intv.21223.

[21] S. X. You et al. “Intravital imaging by simultaneous label-free autofluorescence- multiharmonic microscopy”. In: *Nature Communications* 9 (2018). You, Sixian Tu, Haohua Chaney, Eric J. Sun, Yi Zhao, Youbo Bower, Andrew J. Liu, Yuan-Zhi Marjanovic, Marina Sinha, Saurabh Pu, Yang Boppart, Stephen A. issn: 2041-1723. doi: 10.1038/s41467-018-04470-8. url: %3CGo%20to%20ISI%3E://WOS:000433299000008.

[22] Evangelia Gavgiotaki et al. “Distinction between breast cancer cell subtypes using third harmonic generation microscopy”. In: *Journal of biophotonics* 10.9 (2017), pp. 1152–1162.

[23] Z. Q. Zhang et al. “Quantitative comparison of 3D third harmonic generation and fluorescence microscopy images”. In: *Journal of Biophotonics* 11.1 (2018). Zhang, Zhiqing Kuzmin, Nikolay V. Groot, Marie Louise de Munck, Jan C. issn: 1864-063X. doi: 10.1002/jbio.201600256. url: %3CGo%20to%20ISI%3E://WOS:000425294600004.

[24] D. Debarre et al. “Imaging lipid bodies in cells and tissues using third-harmonic generation microscopy”. In: *Nat Methods* 3.1 (2006), pp. 47–53. doi: 10.1038/nmeth813.

[25] Patricia T Bozza and João PB Viola. “Lipid droplets in inflammation and cancer”. In: *Prostaglandins, Leukotrienes and Essential Fatty Acids (PLEFA)* 82.4-6 (2010), pp. 243–250.

[26] Rossana C. N. Melo et al. “Lipid Bodies in Inflammatory Cells: Structure, Function, and Current Imaging Techniques”. In: *Journal of Histochemistry and Cytochemistry* 59.5 (2011), pp. 540–556. doi: 10.1369/0022155411404073. url: http://www.ncbi.nlm.nih.gov/pmc/articles/PMC3201176/.

[27] L. Tirinato et al. “An Overview of Lipid Droplets in Cancer and Cancer Stem Cells”. In: *Stem Cells International* 2017 (2017), p. 17. doi: 10.1155/2017/1656053. url: https://doi.org/10.1155/2017/1656053.

[28] Yi Sun et al. “Intraoperative visualization of the tumor microenvironment and quantification of extracellular vesicles by label-free nonlinear imaging”. In: *Science Advances* 4.12 (2018), eaau5603. doi: 10.1126/sciadv.aau5603.

[29] Câtoi C. Baba AI. “TUMOR CELL MORPHOLOGY”. In: *Comparative Oncology*. The Publishing House of the Romanian Academy, 2007. Chap. 3.

[30] Terese Winslow. *Risk of Breast Cancer Death is Low After a Diagnosis of Ductal Carcinoma in Situ*. Figure. 2015. url: https://www.cancer.gov/news-events/cancer-currents-blog/2015/dcis-%20low-risk.

[31] Sandra M. Swain. “Ductal Carcinoma in Situ”. In: *Cancer Investigation* 10.5 (1992), pp. 443–454. issn: 0735-7907. doi: 10.3109/07357909209024802. url: https://doi.org/10.3109/07357909209024802.

[32] Raghu Ambekar et al. “Quantifying collagen structure in breast biopsies using second-harmonic generation imaging”. In: *Biomedical optics express* 3.9 (2012), pp. 2021–2035. doi: 10.1364/BOE.3.002021.

[33] G. Falzon, S. Pearson, and R. Murison. “Analysis of collagen fibre shape changes in breast cancer”. In: *Phys Med Biol* 53.23 (2008), pp. 6641–52. doi: 10.1088/0031-9155/53/23/001.

[34] K. Tilbury and P. J. Campagnola. “Applications of Second-Harmonic Generation Imaging Microscopy in Ovarian and Breast Cancer”. In: *Perspectives in Medicinal Chemistry* 7 (2015). Tilbury, Karissa Campagnola, Paul J., pp. 21–32. issn: 1177-391X. doi: 10.4137/pmc.s13214. url: %3CGo%20to%20ISI%3E://WOS:000215781100003.

[35] Ivana Prvulović et al. “Morphometry of tumor cells in different grades and types of breast cancer”. In: *Collegium antropologicum* 34.1 (2010), pp. 99–103.

[36] Aparna Narasimha, B Vasavi, and M Harendra Kumar. “Significance of nuclear morphometry in benign and malignant breast aspirates”. In: *International Journal of Applied and Basic Medical Research* 3.1 (2013), pp. 22–26. issn: 2229-516X. doi: 10.4103/2229-516x.112237.

[37] D Parmar, Nilima Sawke, and G Sawke. “Diagnostic application of computerised nuclear morphometric image analysis in fine needle aspirates of breast lesions”. In: *Saudi Journal for Health Sciences* 4.1 (2015), pp. 51–55. issn: 2278-0521. doi: 10.4103/2278-0521.151409.

[38] K. Chrabaszcz et al. “Label-free FTIR spectroscopy detects and visualizes the early stage of pulmonary micrometastasis seeded from breast carcinoma”. In: *Biochimica Et Biophysica Acta-Molecular Basis of Disease* 1864.11 (2018), pp. 3574–3584. doi: 10.1016/j.bbadis.2018.08.022. url: %3CGo%20to%20ISI%3E://WOS:000447477400002.

[39] Wael M Elshemey, Alaa M Ismail, and Nihal S Elbialy. “Molecular-level characterization of normal, benign, and malignant breast tissues using FTIR spectroscopy”. In: *Journal of Medical and Biological Engineering* 36.3 (2016), pp. 369–378.

[40] S. G. Kazarian and K. L. A. Chan. “Applications of ATR-FTIR spectroscopic imaging to biomedical samples”. In: *Biochimica et Biophysica Acta (BBA) - Biomembranes* 1758.7 (2006), pp. 858–867. doi: https://doi.org/10.1016/j.bbamem.2006.02.011. url: http://www.sciencedirect.com/science/article/pii/S0005273606000630.

[41] Zanyar Movasaghi, Shazza Rehman, and Dr Ihtesham ur Rehman. “Fourier Transform Infrared (FTIR) Spectroscopy of Biological Tissues”. In: *Applied Spectroscopy Reviews* 43.2 (2008), pp. 134–179. issn: 0570-4928. doi: 10.1080/05704920701829043. url: https://doi.org/10.1080/05704920701829043.

[42] RK Sahu and S Mordechai. “Fourier transform infrared spectroscopy in cancer detection”. In: (2005).

[43] J. Zhao et al. “FTIR Spectrum Comparisons Among the Breast tissues: the Normal Tissues, Hyperplasia, Fibroadenoma and Cancer”. In: *Chemical Journal of Chinese Universities-Chinese* 32.2 (2011), pp. 246–251. url: %3CGo%20to%20ISI%3E://WOS:000287826200010.

[44] Shiro Koizume and Yohei Miyagi. “Lipid Droplets: A Key Cellular Organelle Associated with Cancer Cell Survival under Normoxia and Hypoxia”. In: *International journal of molecular sciences* 17.9 (2016), p. 1430. issn: 1422-0067. doi: 10.3390/ijms17091430.

Chapter 7

Detection of the T cell activation state using non-linear optical microscopy

The final target of this thesis was the development of a non invasive label free imaging technique for real time monitoring of T cell activation. After studying how nonlinear microscopy could be a useful diagnostic tool in case of cancer, in this final chapter it was inquired whether nonlinear microscopy could provide valuable information during treatment. Immunotherapy is an effective and promising treatment option for cancer. This final chapter describes the study of T cells activation by using Third Harmonic Generation (THG) imaging as diagnostic tool. Qualitative and quantitative analysis showed statistically significant increase of THG mean area and THG signal intensity in activated versus resting T-cells. Moreover, the correlation of THG imaging to chemical information (lipids, cholesterol distribution) was achieved using Raman spectroscopy.

7.1 T cells

The immune system (from the Latin word immunis, meaning: ”free” or ”untouched”) protects the body like a guardian from harmful environmental influences and is essential for survival. The adaptive immune system is crucial for many diseases. The acquired immune system, mainly composed by T and B lymphocytes, plays a key role in protecting the host from infection. It is important and technically challenging to identify immune cell types and their activation status in living and intact state, without staining or fixation. The last years tremendous progress has been made in terms of understanding not only how the immune system acts, but also how new therapies targeting the immune system might enrich the strategies which can be used to manage a devastating disease [1–3]. The immune system works in a coordinated manner to monitor the body for germs or substances that might cause problems. The immune system is probably the most disseminated and mobile system of the body, consists of individual cells that are in continuous circulation endlessly surveying peripheral tissues for possible infection and returning to mount defenses.

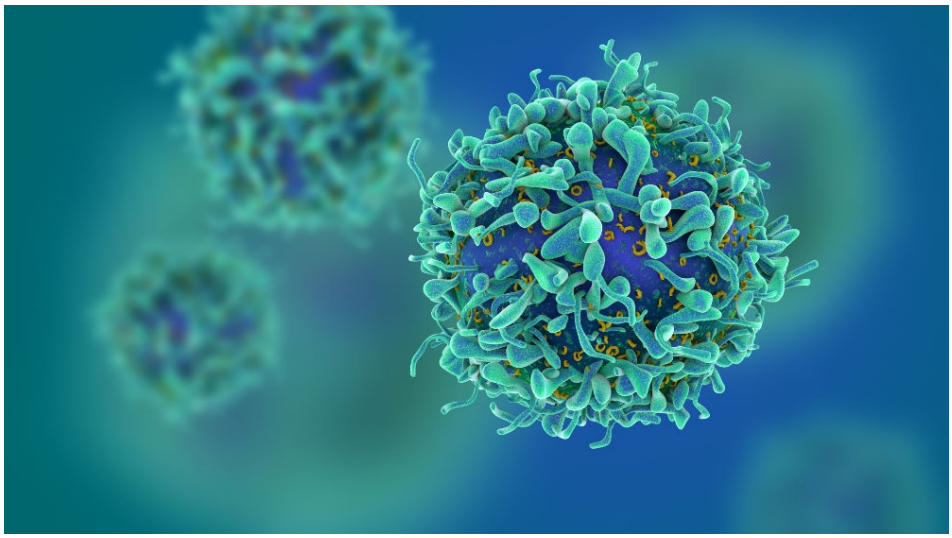

Figure 7.1: Image of a T cell.

T cells that are also known as T lymphocytes (Figure 7.1), are a type of white blood cells that plays a key role in the immune system. Specifically, the function of T cells is to recognize specific "non-self" antigens, during a process known as antigen presentation. Once they have identified an invader, they generate specific responses that are tailored to maximally eliminate specific pathogens or pathogen-infected cells. T cells are the basic type of cells that maintain homeostasis in all systems of an organism, including hematopoietic, nervous, reproductive and hormonal. T cell activation indicates the body's reaction to exogenous and endogenous stimuli. The goal of such activation is primarily the defense of the organism against exogenous infectious pathogenic microorganisms, or against endogenous oncogenic targets (control of cancer/ mutant cells). In contrast to the beneficial effect of T cells, the uncontrolled impel triggering them, leads to auto-inflammatory reactions, auto-immunities and immune deficiencies.

Much of recent focus has been concentrated on the role of the activated immune response and inflammation in many physical disorders, including cancer. Tumors use many strategies to evade the host immune response, including downregulation or weak immunogenicity of target antigens and creation of an immune- suppressive tumor environment. In recent years, tumor-induced immunosuppression mediated by factors and cells has been extensively studied. The major targets of immunosuppression are effector T cells. Tumors develop various mechanisms to escape T cell attack. Thus, tumor cells can influence T cell trafficking by upregulating adhesion molecules, evade T cell recognition by downregulating major histocompatibility complex class I and class II antigens, impact T cell metabolism through production of indoleamine 2,3-dioxygenase, arginase, inducible NO synthase mostly by activating myeloid-derived suppressor cells, dysregulate T cell function by inducing suppressive factors (gangliosides, interleukin-10, transforming growth factor-β, prostaglandin E2, etc), induce T cell apoptosis through stimulation of programmed death-1/ programmed death ligand-1 (PD-1/PDL-1), FasL etc [4].

The goal of cancer therapies is to destroy malignant cells, without damaging healthy tissues. Thus, many immune therapies are designed to take advantage of the specificity and cytotoxic capacity of T

cells. T cell adoptive therapies for immune-mediated regression of cancers have attracted a great deal of recent attention [2, 3, 5].

As our understanding of the immune system has advanced, increasing numbers of innovative therapies are being developed that utilize the cells of the immune system and optimize their disease-targeted response through genetic modification. Recently, strategies to genetically modify T cells either through altering the specificity of the T cell receptor (TCR) or through introducing antibody-like recognition in chimeric antigen receptors (CARs) have made substantial advances (Figure 7.2). Specifically, tumor immunotherapy lies on T cell blocking parameters and targets on T cell activation against tumor cells. Such therapies include inactivation of the PD-1/PDL-1 system as well as blockage of CTLA-4 by specific antibodies [3].

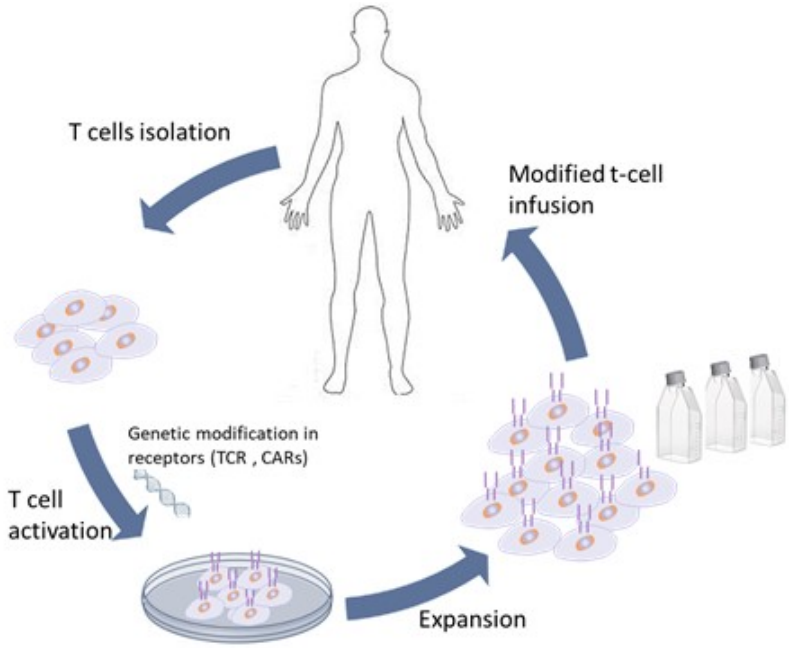

Figure 7.2: Schematic diagram of personalized T cell therapy.

T-cell therapy has become an increasingly attractive modality for the treatment of cancer (Figure 7.3), and has been suggested as a clinical path to a more effective cancer treatment for patients with metastatic disease [6].

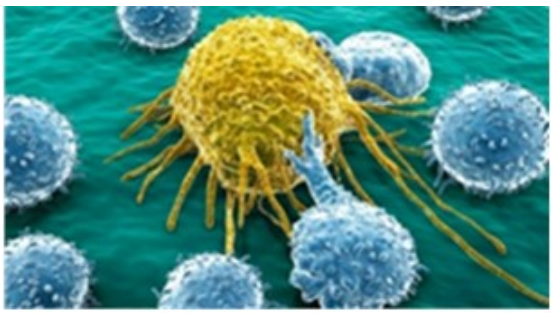

Figure 7.3: Image of killer T cells attacking a cancer cell.

Despite its clinical success, it is being shown that each type of tumor and each individual is subjected to specific regulatory mechanisms, which make the choice of treatment unpredictable. Many efforts focus on defining molecular markers to predict the responsiveness of each patient to specific immunotherapies, but no definite results have been obtained so far [1–3]. Yet, a common goal of all these treatments would be the modulation of T cells from the non-energetic to the active state.

Although the manipulation of the patient's immune system against the tumor is one of the most promising practices, the susceptibility and/or responsiveness to a specific therapy cannot be evaluated before or during treatment, but it can only be appreciated after completion of the therapy, which in the case of non-responsive patients can be fatal because of precious time consumption. It becomes thus mandatory to define diagnostic tools monitoring the activation state of T cells during the treatment.

Despite the wealth of knowledge of the molecular and physiological aspects of the immune system, we know surprisingly little of how cells coordinate the initiation of suppression of an immune response. Specifically at the molecular level, T cell activation is a very complicated issue to address. Multiple markers can be expressed, miscellaneous products can be secreted, most of which are not sufficiently studied, and thus detection of a limiting number of stimulatory markers could not ensure the overall T cell activation. A pressing need has existed for non invasive techniques that overcome these issues and permit real-time observation of single cells. The present study attempted to define a universal method for detecting T cell activation, without concentrating on specific marker expression. Thus, the capacity of non-linear optical imaging microscopy, in obtaining quantitative information for T cells activation, was investigated. This information has the potential to correlate the stage of T cell activation with the response to a specific treatment.

7.2 Study of T cell activation via THG microscopy

The application of non-linear microscopy techniques and especially THG microscopy has enabled a revolution in biomedical studies [7–12]. As already aforementioned, the efficiency of these modalities is that they offer valuable and complementary information on the specimen under investigation.

THG advantage is that it provides unique structural, anatomical and morphological information in various biological samples at cellular and sub-cellular level. THG excitation occurs predominantly at interfaces that are formed between aqueous interstitial fluids and lipid-rich structures, such as cellular membranes and lipid droplets [10, 12–14].

Previous studies have shown that lipid bodies are the main intracellular sources for the high THG signals [7, 15], while others have indicated that polarized THG microscopy can discriminate triacylglycerols from cholesteryl esters in intact mammalian cells [16]. There have been a number of longitudinal studies from our group that have utilized THG optical imaging for quantification analysis, which is mainly based on the lipid contents of different biological samples. Specifically, these studies concentrated on the efficiency of THG signal quantification to be used as an innovative diagnostic tool in the follow-up of mouse embryo development, and in distinguishing mouse BV2 microglia cell activation [17].

In previous chapters it was quoted that in biological samples, THG signal is enhanced by the presence of multilayered structures, like membranes and lipid bodies. In particular, cancer cells were

embedded with nile red, staining of LBs, and revealed significant colocalization with THG signals. Moreover, another research has shown that in THG imaging, the primary sub-cellular source of contrast, are lipid bodies (LBs) [15]. Therefore, such approach can be used to study lipid bodies in complex environments.

7.3 Lipid Bodies and Inflammation

In addition, it was denoted that LBs or LDs have engendered considerable recent interest and considered as dynamic and functionally active organelles. Over the past years substantial progress has been made to demonstrate that lipid body biogenesis is a highly regulated process that culminates in the compartmentalization of a specific set of proteins and lipids. Specifically, in leukocytes lipid bodies are considered to be inducible cytoplasmic organelles with roles in cell signaling and activation, regulation of lipid metabolism, membrane trafficking and control of the synthesis and secretion of inflammatory mediators [18]. Furthermore, active LBs biogenesis is observed in vivo during inflammatory reactions of different causes. Increased cytoplasmic lipid accumulation in leukocytes and other cells has been observed in a number of clinical and experimental inflammatory and infectious diseases [19].

In leukocytes, lipid bodies are functionally active organelles with central roles in inflammation and are considered as structural markers of inflammatory cells in a range of diseases. Lipid bodies were shown to characteristically increase both in size and number in vivo in cells associated with inflammatory diseases. Studies of leukocyte lipid bodies are providing functional, ultrastructural and protein compositional evidence that lipid bodies are not solely storage depots of neutral lipids [18]. Recently, researchers have shown an increased interest in investigating the mechanisms of lipid bodies in cancer progression and how they affect cancer biology [20–22]. The knowledge of how lipids orchestrate the complex interactions between transformed epithelial cells and the surrounding stromal cells is crucial for understanding tumor evolution, progression and metastasis. However, the identification of lipid bodies has methodological limitations because lipid bodies dissipate upon drying or dissolve upon fixation and staining with alcohol-based reagents [21].

7.4 Non-linear microscopy applications in immunological studies

The development of microscopic apparatuses to detect leucocytes and to delineate their key role in immune system has gained a lot of attention during the last years [19, 23]. The application of nonlinear microscopy techniques has enabled a revolution in immunological studies. The last decade nonlinear optical microscopy and specifically multiphoton microscopy have been applied to observe T cell behavior [24]. T cells are involved in many different types of immune response during infection, cancer, autoimmunity and allergic diseases. In 2002, Miller et al. visualized for the first time lymphocyte motility and response during infection by using two photon excitation fluorescence (TPEF) microscopy [25]. Thereafter, the same authors focused their research on the visualization of single cell dynamics and concentrated on CD4(+) T cell activation by dendritic cells in lymph nodes [26]. Using intravital epifluorescence and two photon microscopy imaging, Hoeller et al. visualized the cutaneous T cell lymphoma migration to the skin in vivo [27]. Recently, Rossi et al. studied immune response develop-

ment in Central Nervous System (CNS) using live imaging by two photon laser scanning microscopy [28].

Previous research of our group concentrated on non-linear microscopy techniques for detecting lipid droplet-mediated cell activation. Specifically, THG microscopy has been employed to discriminate the activation state of the BV-2 microglia mouse cell line by quantifying the amount of lipid droplets. In BV-2 microglia cells, it was shown that the number of LBs significantly increased upon activation with lipopolysaccharide [17]. Furthermore, based on the amount and size of LBs as well as the signal emitted by the cellular membranes, THG microscopy allowed quantitative discrimination of the different types of human breast cancer cell lines as compared to peripheral blood mononuclear cells (PBMCs) (see Chapter 5). Combining these findings with Fourier Transform Infrared (FTIR) spectroscopy additional valuable chemical information on breast cancer cells was provided, correlating THG signal to lipid rafts [7].

In addition, THG microscopy has been implemented as label free diagnostics tool for immunological studies. Tsai et al. demonstrated the granularity differences of mouse leucocytes based on THG signal [29]. In addition, Wu et al. developed a label-free imaging cytometry based on THG microscopy combined with a clustering algorithm in human leucocytes [30].

7.4.1 Discrimination between B and T cells

The methodological approach taken in this study is a combined methodology of the previous research (see Chapter 5). The main objective of this essay was to develop a novel system based on the collection of non-linear signals that provides information as to the activation state of T cells. Using a mitogenic or a specific antigenic stimulus for T cells, the present work inquired whether in the absence of any specific marker immunostaining, THG imaging and Raman spectroscopy could provide information as to the activation state of the cells.

Spleen cells from naïve mice were submitted to a mitogenic T cell response using Concanavalin-A (Con A) in order to evaluate maximal activation and an antigen- specific response using human serum albumin (HSA) to evaluate minimal single antigen-specific activation (see in detail the procedure in Chapter 4) (Figure 7.4).

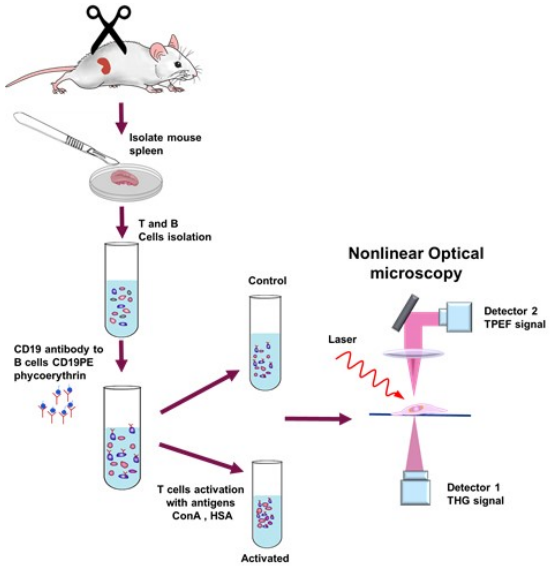

Figure 7.4: Cell preparation for the performance of the non-linear imaging measurements.

However, the problem that had to be faced was the morphological similarity between T-and-B-cells, which are both present in the spleen cell preparations used in these studies. Normally, flow cytometry testing is used for specific lymphocyte population counts. For this reason, a fluorescence staining procedure was used for the distinction-isolation of the two cell types.

Because of the interference of TPEF/THG signals, T cells were negatively distinguished from B cells. The discrimination of B cells was based on the specific expression of CD19, which was detected using anti-CD19-PE antibody through TPEF measurements, while also recording THG signals (Figure 7.5). Using phycoerythrin (PE) as a detection marker it was feasible to identify the specific antigen (CD-19) expressed on the surface of B cells via TPEF measurements. At the same time THG imaging could detect a polarized signal, which as previously shown reflects LBs in the cells, while also identifying nucleus, characterized by the absence of any THG signal due to its homogeneous distribution (Figure 7.5). Such approach allowed B cell distinction in the sample and their exclusion from further processing.

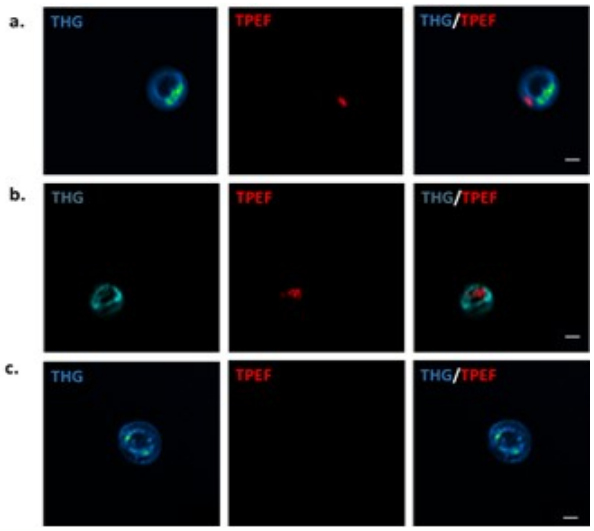

Figure 7.5: Discrimination T cells of B cells by using anti-CD19PE staining. The first two (a, b) are B cells while the last present T cell (c) as not TPEF signal detected. Cells are visualized by THG imaging (first column), and TPEF imaging (second column). Merged signals are shown in third column. Scale bar depicts 2 μm.

7.4.2 T cell activation

Upon exclusion of B cells, a combination of qualitative and quantitative approaches of T cell activation was used in this essay for data analysis. T cell activation was achieved using two different methods: a mitogenic stimulation with concanavalin A (Con A), which is a potent non-specific stimulator of T cells and a specific antigenic challenge with human serum albumin (HSA). At the first glance, it could be easily demonstrated that activated T cells, both with Con A and HSA, were bigger in size and contained more intracellular organelles as compared to resting T cells (Figure 7.6). The nucleus in the antigen-stimulated cells was placed centrally and THG signal showed a uniform polarized distribution. However, the mitogen-stimulated cells displayed a large and expanded cytoplasmic area with sparsely distributed LBs, while the nucleus was pushed to the cellular pole, indicating the active secretory ability of these cells.

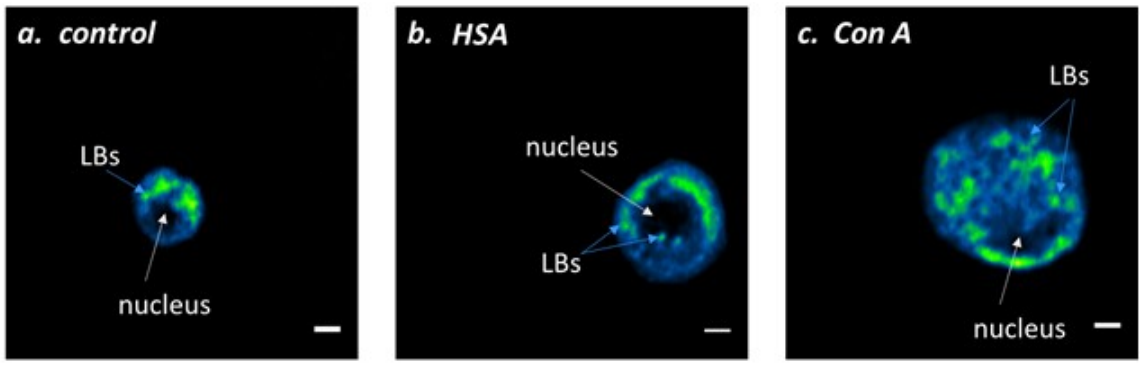

Figure 7.6: THG images of T cells (a) control, (b) HSA activation and (c) Con A activation. A characteristic example of one cell out of at least 40 in each case is shown here. The white arrows depict nuclei while blue arrows show intracellular LBs. Scale bar depicts 2 μm.

7.4.3 Quantification of THG signal area

THG modality is not limited to visualization, since it also allows quantitative analysis and testing of specific mechanisms and activities of high biological significance. Thus, except from the difference in size, which can be successfully detected using common technologies as well, the important information provided by THG imaging is the significant changes in signal emission by the activated cells, in the absence of any specific immunostaining. However, the application of this technology in diagnosis needs quantitative measurements in order to be subjectively applied to clinic. After setting the threshold for THG intensity and area (Figure 7.7), the mean THG area, THG intensity and THG area per cell volume were evaluated.

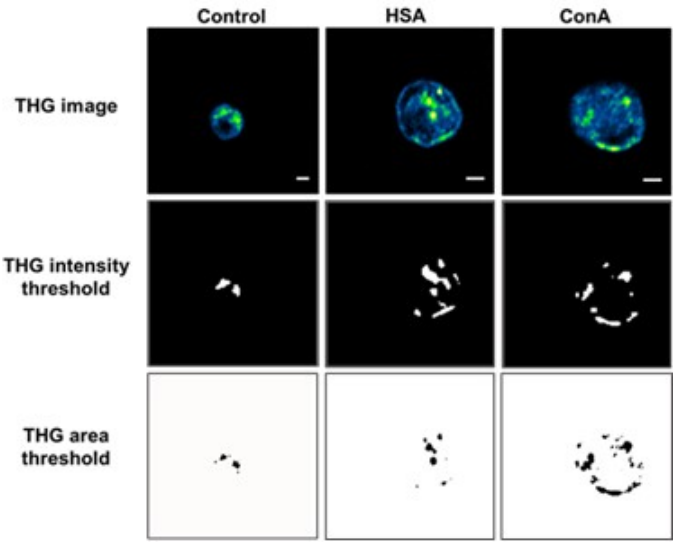

Figure 7.7: THG images and the corresponding threshold images for THG intensity and THG area quantification. Scale bar depicts 3 μm.

Quantification analysis for mean THG area was accomplished under constant irradiation conditions (mean energy per pulse, linear polarization of the incident beam t the sample plane, dimensions of the scanning region, number of pixels, amplification of the PMT units) for all samples. THG intensity values were collected from the photomultipliers' tubes (PMTs), stored in 2D 500 by 500 matrices that represented a single slice image of the sample. Image J software was used for image processing and thresholding. THG signal quantification was performed by setting a constant threshold in the obtained normalized 8-bit slice images, so that regions generating high levels of non-linear signal were solely detected and isolated. The threshold was set in a way to allow only 33% of the THG signal of the cell area to be analyzed and measured. The obtained calculated area of each cell corresponded mainly to lipid bodies. The quantification of mean THG area was calculated from the 5 central sequential z slices of each cell. Forty cells were tested in each case (control, ConA activated cells, HSA activated cells).

The statistical analysis of T cell quantification applied for multi group comparisons and two-tailed unpaired Student's T-test respectively. P-values < 0.05 were considered significant (*), values < 0.01 were considered very significant (**), and values < 0.001 and < 0.0001 were considered highly significant ($***$ and $****$). Statistics were performed using GraphPad Prism 6.01 (Graphpad Software,

La Jolla, CA).

The results showed that the Con A-activated T cells displayed a statistically significant 4-fold larger mean THG area (mean number of pixels above an intensity threshold, $p < 0.0001$) as compared to controls (Figure 7.8), while T cells activated with HSA displayed a statistically significant 2-fold bigger area ($p < 0.0001$) as compared to resting cells. Apparently, the mitogenic stimulation, which corresponds to a robust activation of the cells, could correspond to the maximal activation state, while the single antigenic stimulus could correspond to a regular activation state of the cells.

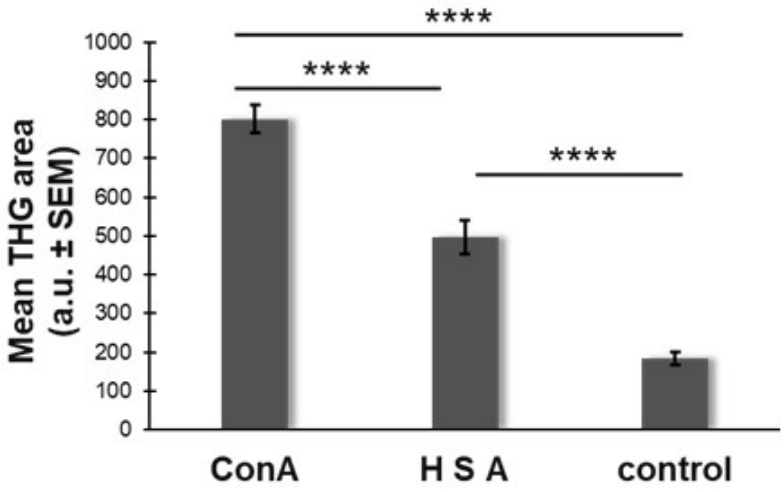

Figure 7.8: Quantification of mean THG area of T cells before and after activation. N=40 for each case.

Taking into consideration the cell size (normalization by dividing the mean total area by the cell volume of each cell type), activated cells still demonstrated significantly increased levels of THG signal as compared to controls ($p < 0.0001$ and $p = 0.00317$ for Con A and HSA stimulation respectively; Figure 7.9). Cell volume was calculated by multiplying the cell surface of each layer with the number of stacks for each cell. These results indicated that THG signal quantification could distinguish between activated and resting T cells, independently of the cell volume increase. However, the mitogenic stimulus showed a 63% higher THG signal area/cell volume as compared to the antigenic stimulus ($p < 0.0001$), observation that supports the mitogen-induced generalized cell activation process.

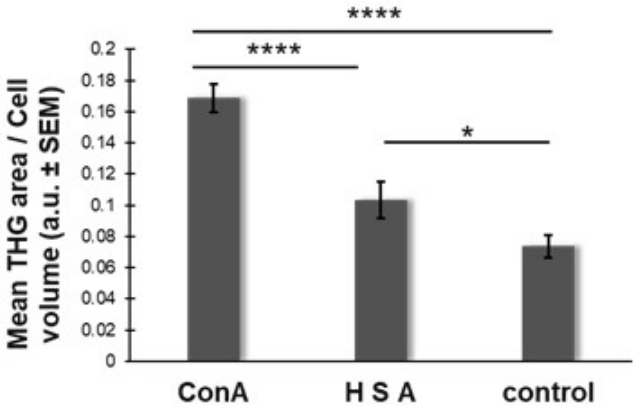

Figure 7.9: Quantification of mean THG area divided by cell volume of T cells before and after activation . N=40 for each case.

For THG intensity quantification, the values of a number of N cells were normalized to their maximum THG intensity value. Then the values were quantified by setting again a constant threshold, so that only the regions that provide high THG signals could be examined (mainly intra cellular lipid bodies). An algorithm that was designed and programmed in MATLAB environment was employed for the manual selection of representative cell areas of each slice and estimation of their mean pixel value. The integrated THG intensity over total pixel area for each slice of a cell was calculated by multiplying the representative area with the mean intensity value of the corresponding pixels. The weighted mean pixel value of each cell was obtained by repeating this procedure for the 5 central slices of the sample.

Figure 7.10 depicts the results of mean THG intensity signal values for control and activated T cells respectively. Quantification of THG intensity signals showed a statistically significant difference between activated and resting cells ($p = 0.0001$ and $p < 0.0001$ for Con A and HSA stimulation respectively), while an approximately 10% increase of THG intensity signals for HSA- as compared to Con A-activated cells was observed ($p = 0.0014$; Figure 7.10). Such difference is in favor of an antigen-specific stimulation and could be linked to potential changes in the chemical constitution of antigen- and mitogen-stimulated T cells.

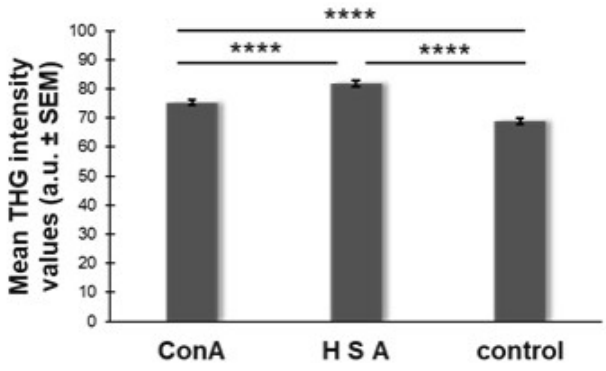

Figure 7.10: Quantification of mean THG area divided by cell volume of T cells before and after activation. N=40 for each case.

Moreover, in this research it was possible to quantitatively evaluate the activation of T cells. The numerical analysis of the percentage of activation by Con A or HSA respectively was calculated by developing an algorithm in MATLAB. This algorithm was determined to set at the same time, the threshold values of the mean volume area and mean lipid area of control cells. The cells were counted as activated when both values of Con A- or HSA-treated cells exceeded the defined thresholds. This analysis showed that in all experiments, the Con A mitogenic stimulus activated approximately 66% of the cells, while HSA activated 54% of the cells. Thus, the obtained results showed that T cell activation not only induced the formation of a bigger amount of subcellular structures, mostly lipid droplets, but also increased cell volume and non-linear intensity signals. THG imaging could be a potential diagnostic tool on distinguishing resting from activated T cells.

7.5 Raman Spectroscopy of resting and activated T cells

Raman spectroscopy provides intrinsic biochemical insights of molecular vibration modes with characteristic frequencies, which can provide information related to molecular species, composition and concentration. The recent years, Raman spectroscopy is gaining popularity for diagnostic applications in the analysis of cellular dynamics [31, 32]. This technique was used to discriminate among different lymphocyte cell lines without labeling [33] and to define the immune cell state and detect dynamic changes in single mouse cells [34]. Moreover, Raman spectroscopy combined with digital holographic microscopy were employed to identify individual immune cells in humans [35].

During activation, T cells are characterized by accumulation of active molecules at the immune synapse in rich in cholesterol lipid raft structures of the membrane. In order to obtain additional biochemical information on T cell activation, Raman spectroscopy was applied on control and activated with Con A or HSA T cells (Figure 7.11). Fifteen cells were tested for each case.

Raman spectra was recorded using a Horiba LabRAM HR spectrometer from at least five points of the cytoplasmic area of T cells, also reflecting membrane chemical structure; Figure 7.11 presents the average Raman spectrum, for each cell. In this case T cells were separated from B cells using magnetic-bead negative section protocols (see chapter methods). Raman spectra of activated and control cells were quite similar, however, distinctive differences were observed in some peaks in lipid regions [36]. Specifically, activated cells – both with Con A and HSA- showed higher peaks at 1336 cm^{-1} (CH_2 / CH_3 in lipids), 1441-5 cm^{-1} (CH_2 & CH_3 in lipids, and cholesterol esters) and 2848 cm^{-1} (CH_2 of lipids). Only within the case of Con A activation, higher peaks at 1078 cm^{-1}, which correspond to phospholipids as well as 1379 cm^{-1} and 1652 cm^{-1}, which are also assigned to lipids, were detected.

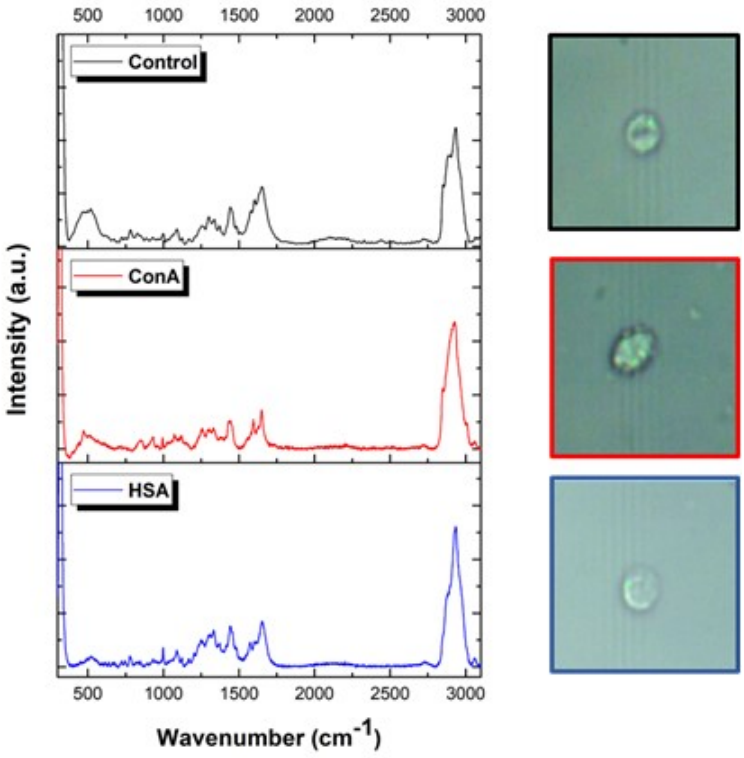

Figure 7.11: Characteristic Raman spectra and brightfield images of control and activated (Con A, HSA) T cells. One representative cell out of N=15 cells for control and for the two different ways of activation is shown here.

All types of cells showed a wide peak at 2876-910 cm^{-1} corresponding to the CH_2 of lipids and at 1453 cm^{-1} linked to the CH_2/CH_3 deformation of phospholipids. Furthermore, integration of Raman spectra could provide a quantitative evaluation of the particular chemical bonds, which consequently correspond to specific compounds (Table 7.1). Table 7.1 illustrates the integrated Raman spectra depicting the concentration (spectra peak area) of chemical bonds for lipids, cholesterol and triglycerides for the three states of cells (control, Con A-activated, HSA-activated). Moreover, Table 7.1 presents the ratios of activated and control cells.

Table 7.1: Integrated Raman spectra *Integrated Raman spectra depict the concentration (spectra peak area) of chemical bonds for lipids, cholesterol and triglycerides for the three states of cells (control, Con A-activated and HSA-activated). The last three columns presented the ratios of Con A/ control, HSA/control and Con A/HSA cells respectively. Fifteen cells were used in each experimental condition.*

Peak (cm^{-1})	**Description**	**Control**	**Con-A**	**HSA**	$ConA/Control$	$HSA/Control$	$ConA/HSA$
614	Cholesterol esters	3.42	17.03	12.12	4.98	3.54	1.41

980	=CH bending (lipids)	6.05	13.80	7.57	2.28	1.25	1.82
1057	Lipids	6.07	15.84	10.22	2.61	1.68	1.55
1073	Triglycerides (fatty acids)	5.85	15.13	8.22	2.59	1.41	1.84
1076-8	v(C-C) or v(C-O), phospholipids (lipid assignment)	11.39	48.65	15.39	4.27	1.35	3.16
1123	C-C stretching mode of lipids & protein, C-N stretch	10.47	28.81	44.80	2.75	4.28	0.64
1264	Triglycerides (fatty acids)	10.47	28.81	44.80	2.75	4.28	0.64
1270	Typical phospholipids	7.66	22.21	12.17	2.90	1.59	1.82
1302	CH_2/CH_3 twisting or bending mode of lipid, $\delta(CH_2)$ twisting, wagging, phospholipids (lipid assignment)	4.91	4.72	11.53	0.96	2.35	0.41
1336	Tryptophan, CH_2/CH_3 wagging, twisting &/or bending mode of collagens & lipids, CH_2/CH_3 wagging & twisting mode in collagen, nucleic acid & tryptophan	5.16	14.44	14.10	2.80	2.73	1.02

1379	$\delta(CH_3)$ symmetric (lipid assignment)	5.77	16.47	7.49	2.85	1.30	2.20
1437	$\delta(CH_2)$ lipids	2.08	9.61	11.21	4.62	5.39	0.86
1441	CH_2 scissoring & CH_3 bending in lipids, Cholesterol & its esters, C-H bending mode of accumulated lipids	5.23	15.12	24.12	2.89	4.62	0.63
1444-5	Cholesterol band, $\delta(CH_2)$, $\delta(CH_3)$, lipids, phospholipids, fatty acids	2.68	22.42	9.59	8.37	3.58	2.34
1453	Overlapping asymmetric CH_3 bending & CH_2 scissoring (in associated with phospholipids)	23.48	16.32	18.11	0.70	0.77	0.90
1465	Lipid	4.74	11.96	11.32	2.52	2.39	1.06
1652	Lipid (C=C stretch)	8.09	16.32	8.79	2.02	1.09	1.86
1656	Amide I C=C (lipids) , triglycerides (fatty acids)	4.96	14.96	2.28	3.02	0.46	6.56
1669	Cholesterol esters	8.73	12.25	14.08	1.40	1.61	0.87
1736	Esters, C=O stretching (lipids)	5.52	11.40	5.76	2.07	1.04	1.98

1743	Carbonyl feature of lipid spectra	6.41	14.22	4.28	2.22	0.67	3.32
1745	Phospholipids, v(C=O)	5.37	11.41	20.69	2.12	3.85	0.55
2848	CH_3 symmetric stretch of lipids	5.19	15.57	15.48	3.00	2.98	1.01
2850	v_sCH_2 lipids , fatty acids	6.60	13.14	3.38	1.99	0.51	3.89
2919	CH stretch of lipids	7.50	14.76	3.58	1.97	0.48	4.12

Thus, activated T cells (both Con A and HSA stimulation) presented enhanced peaks at 1336 cm^{-1}, 1437 cm^{-1}, 1465 cm^{-1} and 2848 cm^{-1} as compared to controls. In addition, activated T cells showed increased triglyceride concentration at 1264 cm^{-1} and cholesterol esters at 614 cm^{-1}, 1444 cm^{-1} and 1669 cm^{-1} respectively.

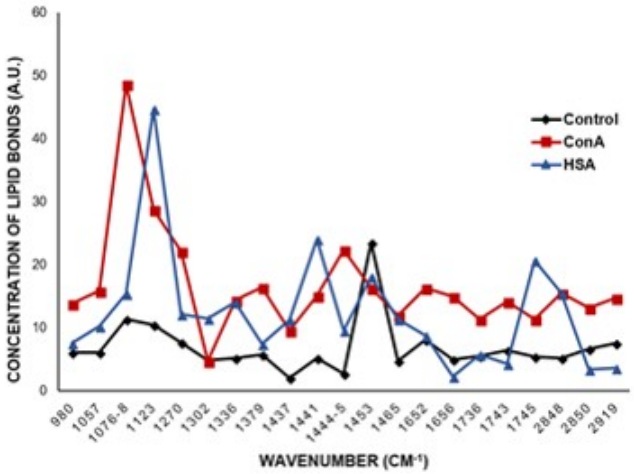

Figure 7.12: Line chart represents the concentration of lipid and phospholipids bonds of control and activated (Con A & HSA) T cells. Data represents mean values of N=15 cells for each case. Activated T cells appear higher values of lipid concentration as compared to control cells in most of the peaks.

As can been seen from the line chart in Figure 7.12, Raman spectra integration revealed that Con A activation displayed an increased concentration of lipids as compared to control and HSA-activated cells . Specifically, increased levels were observed at 980 cm^{-1} which is attributed to =C-H bending of lipids, at 1057 cm^{-1} attributed to lipid regions, at 1076-8 cm^{-1} which is assigned to v(C-C) phospholipids, at 1270 cm^{-1} corresponding to the amide III area of phospholipids, at 1379 cm^{-1} for $\delta(CH_3)$, at 1445 cm^{-1} for CH_2 and CH_3 phospholipids, at 1652 cm^{-1} for C=C stretching, at 1736 and

1743 cm^{-1} for C=O ester in lipids, at 2850 cm^{-1} for CH_2 symmetric stretching of lipids and fatty acids and at 2919 cm^{-1} for CH stretching of lipids (Figure 7.12). Moreover, Con A activated T cells showed an accumulative concentration of triglycerides (fatty acids) at 1073 cm^{-1} and 1656 cm^{-1} (Figure 7.13).

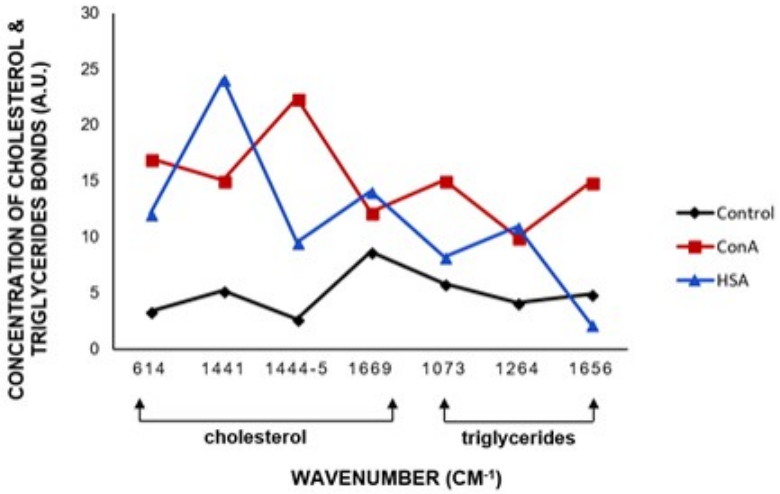

Figure 7.13: Line chart represents the concentration of cholesterol (614 cm^{-1}, 1441 cm^{-1}, 1444-5 cm^{-1}, 1669 cm^{-1}) and triglycerides (1073 cm^{-1}, 1264 cm^{-1}, 1656 cm^{-1}) bonds of control and activated (ConA or HSA) T cells. Data represents mean values of N=15 cells for each case.

The HSA-activated T cells were shown to display enhanced peak concentrations at 1123 cm^{-1} corresponding to C-C stretching in lipids and proteins as well as C-N stretching , at 1302 cm^{-1} corresponding to $\delta(CH_2)$ in phospholipids and at 1745 cm^{-1} corresponding to v(C=O) and phospholipids, as compared to control cells (Figure 7.12). In addition, regarding cholesterol bonds, which were obtained at 1441 cm^{-1} and 1669 cm^{-1}, the HSA activation provided higher concentrations as compared to control and Con A-stimulated T cells (Figure 7.13).

7.6 Correlation THG signals with Raman spectra

Based on the above observations, it was then inquired whether lipid bodies could be correlated to the triacylglycerol-enriched structures and cholesteryl esters. These compounds are of great interest because are the most clinically relevant lipid constituents found in cells and tissues and are hallmarks of the most common lipid – related disorders [16]. Data from table 7.1 can be compared with the data of THG area and intensity respectively. Thus, correlation analysis of the mean THG area and the mean of Raman spectrum area of lipids, cholesterol esters and triglycerides was performed. In this case, the ratios of Con A-stimulation/control, HSA-stimulation/control and $^{ConA}/_{HSA}$ stimulation of mean THG and Raman spectra areas were examined (Figure 7.14). Linear fitting analysis showed high correlation of THG area with cholesterol and lipid compounds (R^2 sin 0.91, R^2 sin0 .94), but not with triglycerides (R^2 sin 0.02).

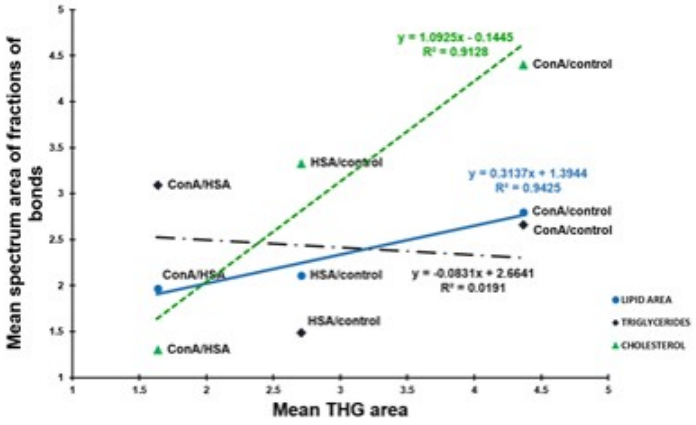

Figure 7.14: Correlation of Raman spectra with mean THG area in lipids, cholesterol and triglyceride peaks respectively. The mean values of fractions for $^{ConA}/_{control}$, $^{HSA}/_{control}$ and $^{ConA}/_{HSA}$ were calculated from Table 7.1 for Raman spectra and from Figure 7.8 for THG area.

Moreover the correlation between mean THG intensity signal and mean Raman spectrum area of lipids, cholesterol esters and triglycerides was tested. Figure 15 presents the correlations between the ratios of $^{ConA}/_{control}$, $^{HSA}/_{control}$ and $^{ConA}/_{HSA}$. The outcome of this correlation (Linear fitting analysis revealed moderate correlation of THG intensity with lipid compounds (R^2 sin 0.83) poor with cholesterol (R^2 sin0.58) and no correlation with triglycerides (R^2 sin 0.10).

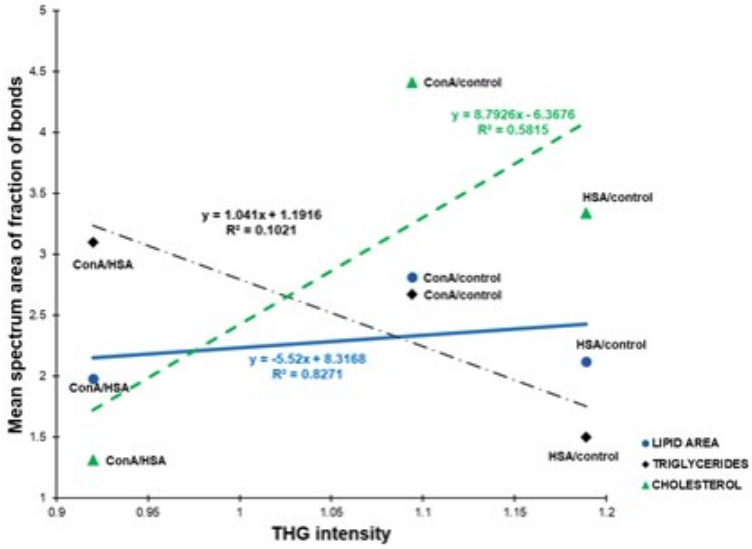

Figure 7.15: Correlation of Raman spectra with mean THG signal intensity in lipids, cholesterol and triglyceride peaks respectively. The mean values of fractions for $^{ConA}/_{control}$, $^{HSA}/_{control}$ and $^{ConA}/_{HSA}$ were calculated from Table7.1 for Raman spectra and from Figure7.10 for THG intensity signal.

Interestingly, the correlation analysis suggested that there is an association between THG area and the Raman spectra corresponding to cholesterol and lipid bonds, during activation (better quality of linear fitting Figure 7.14). The data supports the assumption that the detected increase of THG area during T cell activation may be correlated to the concentration of cholesterol and lipid compounds.

However, it has to be noted that no significant correlation between mean THG intensity signals and mean Raman spectra area could be observed in cholesterol and triglyceride compounds except from a moderate correlation to lipid bonds (Figure 7.15).

7.7 Conclusion

This project was undertaken to develop a diagnostic optical tool to evaluate T cell activation. The evidence of this study suggests that liposome storage is of great importance in cellular defense mechanisms since by trapping fatty acids they protect the cell from liposuction and lipotoxicity. Such liposome activity is correlated with the function of immune system, observation that is based on the accumulation of leukocytes at inflammatory sites during infections, cancer or allergies. The present study aimed to correlate T cell activation with LB cellular content and specific membrane compound accumulation in the context of a marker-free evaluation system, which would be very useful in immunotherapy. Choosing a mitogenic stimulus for maximal T cell activation and an antigen specific response for regular activation, THG imaging showed that except from increasing cell size, T cell activation significantly increased the formation of subcellular structures, mostly lipid droplets. Interestingly, the mitogenic activation showed higher mean THG area values which was correlated to specific Raman spectra corresponding to cholesterol and lipids in favor to the T cell activation profile.

This assay extents our knowledge during immunotherapy, and provides information as to whether the patient is responsive to the therapeutic protocol, which is of great importance for the management of the disease. Activation of T cells by the means of marker expression is a very complicated and not fully exploited manner. Previous studies have shown that THG imaging could distinguish between activated and non-activated microglia cells based on the significant increase of LDs, largely reflecting the energetic state of the cells[17]. Yet, different types of activation states do exist and it is therefore important to be able to distinguish even a minimal antigen specific response. Therefore, the present study concentrated on a mitogenic and a specific antigenic response, considering that these would represent a maximal and a minimal type of stimulation. Con A binds and cross-links co-stimulatory molecules of the T cell receptor (TCR) in the immune synapse [37], therefore activating in a non-specific manner all TCR bearing cells. On the other hand, HSA activates only specific T cell populations bearing HSA-specific TCRs and for this reason the activation ranges at lower levels.

Following the permanent need for novel diagnostic non-destructive label free tools in biomedical studies at subcellular level, THG imaging and Raman spectra analysis were used to evaluate the activation state of T cells. THG modality presents distinct advantages over other techniques since it can visualize intracellular structures (lipid bodies) without any labeling and without affecting the viability of the biological sample. THG imaging is a valuable technique particularly for cellular imaging and quantification analysis studies and it is being increasingly employed in a number of different biological applications [7, 17, 30]. Thus, T cell activation could be visualized and quantified using THG imaging through the detection of the LB content of the cells. Mean THG area values were higher in Con A-stimulated cells and lower in HSA-activated T cells, but in both cases statistically significantly higher than resting T cells. The recorded results suggest that the different activation pathways can provide different quantitative information, based on the number of lipid depositions, distinguishing thus,

in a reliable and accurate manner, the condition of the cells in each case of activation. Specifically, the comparison between a mitogenic and an antigen-dependent activation can provide information on the different use of co-receptors and activators. Moreover, the increase of THG signal intensity during activation, although not perfectly correlated with the recorded Raman spectra, could be linked to potential changes in chemical constitution of the cells. The increase of THG signal intensity during activation with HSA as compared to resting and Con A-stimulated T cells could be correlated with the increased concentration of cholesterol specific bonds at 1441 cm^{-1} and 1669 cm^{-1}.

Additionally, Raman spectroscopy measurements correlated specific chemical information to the increased THG signal during activation of the cells. Raman analysis enables the determination of chemical alterations of cellular components during the different ways of activation. Raman analysis showed an increased lipid content during Con A activation that is in perfect agreement with the results obtained with the THG technology. The quantification of the recorded THG signals provides reliable biological criteria, through a novel non-destructive label free approach, for the investigation of the activation state of T cells. The implementation of this study could be applicable to clinical diagnostic practice. This technique could act synergistically with flow cytometry for obtaining complementary information related to the activation state of cells during immunotherapy. However, for clinical use, these findings should be validated employing human PBMCs. Simple blood sampling would provide immediate reliable information on the immune system activation status which could be useful in autoimmune diseases, allergies, vaccines, as well as antitumor therapies. It should be noted, that by employing unstained samples the cost of diagnosis is significantly reduced, resulting in long term economic benefits. Furthermore, one could foresee the development of a compact apparatus integrating nonlinear microscopy and Raman spectroscopy modalities to a single instrument. Such optimized system would be extremely useful as a new, nondestructive diagnostic tool for the simultaneously acquisition of structural sub-cellular information, lipid content quantification and chemical analysis of various cell types.

The results in this research indicate that THG microscopy provides a unique tool for assessing the activation state of a cell via the detection of lipid bodies. By evaluating lipid body modifications during T cell activation the present work achieved discrimination between control and mitogen- or antigen-activated T cells based on the THG mean total area, cell surface area and THG intensity signals. Although non-linear imaging cannot directly provide specific chemical information, further analysis using Raman spectroscopy has correlated the recorded THG signals of control and activated T cells to lipids and cholesterol. The detection of T cell activation is an important issue in cancer immunotherapy as it allows easy following–up of immune response development. It is thus anticipated that in near future, non-linear optical imaging of immune cells could be extended to screening and understanding the action of immunosuppressive drugs, infections, tumor immunotherapy and autoimmune diseases.

Bibliography

[1] Richard S. Hotchkiss, Guillaume Monneret, and Didier Payen. “Immunosuppression in sepsis: a novel understanding of the disorder and a new therapeutic approach”. In: *The Lancet Infectious Diseases* 13.3 (2013), pp. 260–268. issn: 1473-3099. doi: https://doi.org/10.1016/S1473-3099(13)70001-X. url: http://www.sciencedirect.com/science/article/pii/S147330991370001X.

[2] Padmanee Sharma and James P. Allison. “The future of immune checkpoint therapy”. In: *Science* 348.6230 (2015), pp. 56–61. doi: 10.1126/science.aaa8172. url: http://science.sciencemag.org/content/sci/348/6230/56.full.pdf.

[3] Michaela Sharpe and Natalie Mount. “Genetically modified T cells in cancer therapy: opportunities and challenges”. In: *Disease Models & Mechanisms* 8.4 (2015), pp. 337–350. doi: 10.1242/dmm.018036. url: http://www.ncbi.nlm.nih.gov/pmc/articles/PMC4381333/.

[4] A. A. Wu et al. “Reprogramming the tumor microenvironment: tumor-induced immunosuppressive factors paralyze T cells”. In: *Oncoimmunology* 4.7 (2015), e1016700. issn: 2162-4011 (Print) 2162-4011. doi: 10.1080/2162402x.2015.1016700.

[5] S. Gottschalk et al. “T cell therapies”. In: *Ernst Schering Found Symp Proc* 4 (2006), pp. 69–82.

[6] Kunyu Li et al. “Adoptive cell therapy with CD4(+) T helper 1 cells and CD8(+) cytotoxic T cells enhances complete rejection of an established tumour, leading to generation of endogenous memory responses to non-targeted tumour epitopes”. In: *Clinical & Translational Immunology* 6.10 (2017), e160. doi: 10.1038/cti.2017.37. url: http://www.ncbi.nlm.nih.gov/pmc/articles/PMC5671987/.

[7] Evangelia Gavgiotaki et al. “Distinction between breast cancer cell subtypes using third harmonic generation microscopy”. In: *Journal of Biophotonics* 10.9 (2017), pp. 1152–1162. doi: 10.1002/jbio.201600173. url: http://dx.doi.org/10.1002/jbio.201600173.

[8] N. V. Kuzmin et al. “Third harmonic generation imaging for fast, label-free pathology of human brain tumors”. In: *Biomedical Optics Express* 7.5 (2016), pp. 1889–1904. doi: 10.1364/BOE.7.001889. url: http://www.osapublishing.org/boe/abstract.cfm?URI=boe-7-5-1889.

[9] T. Meyer et al. “Accumulating advantages, reducing limitations: multimodal nonlinear imaging in biomedical sciences - the synergy of multiple contrast mechanisms”. In: *J Biophotonics* 6.11-12 (2013), pp. 887–904. issn: 1864-063x. doi: 10.1002/jbio.201300176.

[10] Aaron M. Streets et al. “Imaging without Fluorescence: Nonlinear Optical Microscopy for Quantitative Cellular Imaging”. In: *Analytical Chemistry* 86.17 (2014), pp. 8506–8513. issn: 0003-2700. doi: 10.1021/ac5013706. url: https://doi.org/10.1021/ac5013706.

[11] G. J. Tserevelakis et al. “Femtosecond laser nanosurgery of sub-cellular structures in HeLa cells by employing Third Harmonic Generation imaging modality as diagnostic tool”. In: *J Biophotonics* 5.2 (2012), pp. 200–7. issn: 1864-063x. doi: 10.1002/jbio.201100055.

[12] B. Weigelin, G. J. Bakker, and P. Friedl. “Third harmonic generation microscopy of cells and tissue organization”. In: *J Cell Sci* 129.2 (2016), pp. 245–55. issn: 0021-9533. doi: 10.1242/jcs.152272.

[13] Jeff Squier and Michiel Müller. “High resolution nonlinear microscopy: A review of sources and methods for achieving optimal imaging”. In: *Review of Scientific Instruments* 72.7 (2001), pp. 2855–2867. issn: 0034-6748.

[14] Warren R. Zipfel, Rebecca M. Williams, and Watt W. Webb. “Nonlinear magic: multiphoton microscopy in the biosciences”. In: *Nature Biotechnology* 21 (2003), p. 1369. doi: 10.1038/nbt899. url: http://dx.doi.org/10.1038/nbt899.

[15] D. Debarre et al. “Imaging lipid bodies in cells and tissues using third-harmonic generation microscopy”. In: *Nat Methods* 3.1 (2006), pp. 47–53. doi: 10.1038/nmeth813.

[16] Godofredo Bautista et al. “Polarized THG Microscopy Identifies Compositionally Different Lipid Droplets in Mammalian Cells”. In: *Biophysical Journal* 107.10 (2014), pp. 2230–2236. doi: 10.1016/j.bpj.2014.10.009. url: http://www.ncbi.nlm.nih.gov/pmc/articles/PMC4241439/.

[17] E. Gavgiotaki et al. “Third Harmonic Generation microscopy as a reliable diagnostic tool for evaluating lipid body modification during cell activation: The example of BV-2 microglia cells”. In: *Journal of Structural Biology* 189.2 (2015), pp. 105–113. doi: https://doi.org/10.1016/j.jsb.2014.11.011. url: http://www.sciencedirect.com/science/article/pii/S1047847714002627.

[18] Patricia T. Bozza, Kelly G. Magalhães, and Peter F. Weller. “Leukocyte lipid bodies — Biogenesis and functions in inflammation”. In: *Biochimica et Biophysica Acta (BBA) - Molecular and Cell Biology of Lipids* 1791.6 (2009), pp. 540–551. doi: https://doi.org/10.1016/j.bbalip.2009.01.005. url: http://www.sciencedirect.com/science/article/pii/S1388198109000080.

[19] Rossana C. N. Melo et al. “Lipid Bodies in Inflammatory Cells: Structure, Function, and Current Imaging Techniques”. In: *Journal of Histochemistry and Cytochemistry* 59.5 (2011), pp. 540–556. doi: 10.1369/0022155411404073. url: http://www.ncbi.nlm.nih.gov/pmc/articles/PMC3201176/.

[20] P. T. Bozza and J. P. Viola. “Lipid droplets in inflammation and cancer”. In: *Prostaglandins Leukot Essent Fatty Acids* 82 (2010), pp. 243–50. doi: 10.1016/j.plefa.2010.02.005.

[21] Rossana C. N. Melo et al. “Imaging Lipid Bodies Within Leukocytes with Different Light Microscopy Techniques”. In: *Methods in molecular biology (Clifton, N.J.)* 689 (2011), pp. 149–161. doi: 10.1007/978-1-60761-950-5_9. url: http://www.ncbi.nlm.nih.gov/pmc/articles/PMC3659330/.

[22] L. Tirinato et al. “An Overview of Lipid Droplets in Cancer and Cancer Stem Cells”. In: *Stem Cells International* 2017 (2017), p. 17. doi: 10.1155/2017/1656053. url: https://doi.org/10.1155/2017/1656053.

[23] Matan M. Winer et al. “In vivo noninvasive microscopy of human leucocytes”. In: *Scientific Reports* 7.1 (2017), p. 13031. issn: 2045-2322. doi: 10.1038/s41598-017-13555-1. url: https://doi.org/10.1038/s41598-017-13555-1.

[24] M. D. Cahalan et al. “Two-photon tissue imaging: seeing the immune system in a fresh light”. In: *Nat Rev Immunol* 2.11 (2002), pp. 872–80. doi: 10.1038/nri935.

[25] Mark J Miller et al. “Two-photon imaging of lymphocyte motility and antigen response in intact lymph node”. In: *Science* 296.5574 (2002), pp. 1869–1873.

[26] M. J. Miller et al. “Imaging the single cell dynamics of CD4+ T cell activation by dendritic cells in lymph nodes”. In: *J Exp Med* 200.7 (2004), pp. 847–56. doi: 10.1084/jem.20041236.

[27] Christoph Hoeller et al. “In vivo imaging of cutaneous T-cell lymphoma migration to the skin”. In: *Cancer research* 69.7 (2009), pp. 2704–2708.

[28] B. Rossi and G. Constantin. “Live Imaging of Immune Responses in Experimental Models of Multiple Sclerosis”. In: *Front Immunol* 7 (2016), p. 506. doi: 10.3389/fimmu.2016.00506.

[29] Cheng-Kun Tsai et al. “Imaging granularity of leukocytes with third harmonic generation microscopy”. In: *Biomedical Optics Express* 3.9 (2012), pp. 2234–2243. doi: 10.1364/BOE.3.002234. url: http://www.osapublishing.org/boe/abstract.cfm?URI=boe-3-9-2234.

[30] Cheng-Ham Wu et al. “Imaging cytometry of human leukocytes with third harmonic generation microscopy”. In: *Scientific reports* 6 (2016), p. 37210.

[31] Rachael Smith, Karen L. Wright, and Lorna Ashton. “Raman spectroscopy: an evolving technique for live cell studies”. In: *Analyst* 141.12 (2016), pp. 3590–3600. issn: 0003-2654. doi: 10.1039/C6AN00152A. url: http://dx.doi.org/10.1039/C6AN00152A.

[32] Henk-Jan van Manen et al. “Single-cell Raman and fluorescence microscopy reveal the association of lipid bodies with phagosomes in leukocytes”. In: *Proceedings of the National Academy of Sciences of the United States of America* 102.29 (2005), pp. 10159–10164. doi: 10.1073/pnas.0502746102. url: http://www.pnas.org/content/pnas/102/29/10159.full.pdf.

[33] Alison J. Hobro et al. “Raman spectroscopy as a tool for label-free lymphocyte cell line discrimination”. In: *Analyst* 141.12 (2016), pp. 3756–3764. issn: 0003-2654. doi: 10.1039/C6AN00181E. url: http://dx.doi.org/10.1039/C6AN00181E.

[34] Taro Ichimura et al. “Non-label immune cell state prediction using Raman spectroscopy”. In: *Scientific Reports* 6 (2016), p. 37562.

[35] Naomi McReynolds et al. “Multimodal discrimination of immune cells using a combination of Raman spectroscopy and digital holographic microscopy”. In: *Scientific Reports* 7 (2017), p. 43631. issn: 2045-2322. doi: 10.1038/srep43631. url: http://www.ncbi.nlm.nih.gov/pmc/articles/PMC5335250/.

[36] Zanyar Movasaghi, Shazza Rehman, and Ihtesham U. Rehman. “Raman Spectroscopy of Biological Tissues”. In: *Applied Spectroscopy Reviews* 42.5 (2007), pp. 493–541. issn: 0570-4928. doi: 10.1080/05704920701551530. url: https://doi.org/10.1080/05704920701551530.

[37] A Weiss et al. “Ligand-receptor interactions required for commitment to the activation of the interleukin 2 gene.” In: *The Journal of Immunology* 138.7 (1987), pp. 2169–2176.

Chapter 8

Outlook and future aspects

The core of this thesis was the application of nonlinear microscopy to biomedical studies in diagnosis and treatment, and the combination of nonlinear signals with vibrational spectroscopy for obtaining additional chemical information.

As has been described and exemplified in the previous chapters, the advantages of these techniques are numerous, namely high depth penetration (due to near infrared (NIR) laser), intrinsic 3D sectioning and 3D resolution (due to the increased spatial confinement of the signal to the laser focus), multiple nonlinear processes summed to the possibility to detect several endogenous molecular structures, and low phototoxicity. All these advantages allow us to postulate that in the near future the NLO techniques together with nonlinear signal processing methods can be very useful in the field of medical diagnosis. In combination with sophisticated animal models and computer-assisted data analysis, NLO microscopy techniques and image processing methods are opening new doors to the study of cancer and inflammation disorders, facilitating the development of new strategies for early tumor diagnosis and other diseases. Additionally, the possibility of obtaining images at high speed and their correlation with methods providing chemical specificity makes NLO microscopy a powerful tool to evaluate the dynamic behavior of in vivo disease progression.

In this thesis nonlinear microscopy techniques, in combination with advanced image analysis approaches and vibrational spectroscopy modalities, represented a powerful tool to investigate biological processes. This capability may allow the implementation of new diagnostic procedures for early detection of various diseases. The integration of a set of microscopy techniques is one of the evolving areas in bioimaging that promises to have a strong impact on the understanding and early detection of diverse pathologies.

In translational research, NLO microscopy has demonstrated the ability to diagnosing diseases. This essay provides a perspective on how nonlinear optical imaging can potentially be applied for cancer diagnostics and therapy. These advances ensure efficient cancer detection in a non-invasive manner with improved sensitivity and specificity. In addition, in this study NLOM has been efficiently combined with other emerging vibrational techniques such as Raman and FTIR spectroscopy. As a result, anatomical, physiological as well as biochemical details can now be jointly obtained from these multimodal imaging techniques with increased sensitivity. In this manner, the limitations of this particular optical imaging technique are countered by the other complimentary spectroscopy modality.

For successful translation of nonlinear optical imaging as a diagnostic tool in the clinic, it is essential to integrate this study in vivo and automate the analysis procedure with advanced computational methods.

Today, the application of multimodal nonlinear imaging is highly appreciated in basic biological research and biomedical sciences; however, regular applications in clinics are still rare, mainly because of the lack of personnel for its operation. So, mainly technological progresses are required for miniaturization, enhancement of the ease of control, automated data processing, and extraction of significant information. To achieve this goal, the modification of typical clinical endoscopes for in vivo multimodal nonlinear imaging is necessary. The development of nonlinear optical endoscopy, which allows imaging under conditions in which a conventional nonlinear optical microscope cannot be used, will be the primary goal to extend applications of nonlinear optical microscopy toward clinical practice. There are several key challenges involved in the pursuit of in vivo nonlinear optical endoscopy. A few of them are the necessity of obtaining efficient ultrashort pulse laser liberations into a remote place, the need to enhance scan rates for faster monitoring of biological processes, and the miniaturization of the laser□scanning mechanisms to the millimeter scale. Finally, the design of a nonlinear optical endoscope based on micro□optics with great flexibility, and compact enough to be incorporated into endoscopes, will become an evolution of these microscopy platforms. With the continuous advancement in this endoscopic technique and new laser sources, we have reason to believe that these particularly promising techniques in conjunction with efficient image analysis algorithm will open up many new possibilities for the diagnosis and treatment of different diseases in the near future.

Appendices

Appendix A

Appendix A

A.1 FTIR analysis in breast cancer cells

Table A.1: Peak analysis of absorbance (FTIR spectra) of breast cancer cell lines in lipid regions(900-1800 cm^{-1}, 2800-3000 cm^{-1}). The symbols depict the different experiments. (PBMCs-control, BT474-HER2+, MDA-MB231-triple negative, MCF7-Luminal) N=3 measurements for each cell line. (∗)1st experiment , (o) 2nd experiment , (x) 3rd experiment, 4th experiment (#) ,(@)

Cell line / Wavenumber (cm^{-1})	**Assignment**	**PBMCs**	**BT474**	**MDA-MB231**	**MCF7**	**Comments**
1016		□ √				Ring Stretching vibrations mixed strongly with CH in plane bending
1020	DNA	∗		□ ox		
1077	Symmetric phosphate stretching	√ □				
1084-5	Mainly from phospholipids (membrane)	∗ √ □	xo ∗	xo	xo	
1163	C−O stretching band of collagen	√ □				

1180	Amide III region	√ □				
1224	Collagen Sym. stretch-ing of phosphate groups in phospho-lipids	√ □				
1340	CH_2 wagging /Collagen	∗ □ √	xo∗	x	xo	
1388		∗ √ □	xo	x	x	
1439		∗ □ √				1400-500 cm−1 Ring stretching vibrations mixed strongly with CH in-plane bending
1448		√ □				
1449	Asymmetric CH_3 bend-ing of the methyl groups of proteins		xo	x □	xo	*Only in cancer cells*
1474			xo	x □	xo	
1491		∗ √ □	o	□		
1541-2	Amide II absorption (primarily an N−H bending coupled to a C−N stretching vibrational mode)		xo	x □	xo	

midrule 1570	Amide III		o		o	Only cancer cells - appear peaks (MCF, BT474)
1576	C=N adenine				*	
1578	Ring C−C stretch of phenyl		o		o	
1597	C=N, NH_2 adenine				*	
1624			o			1600-1800cm−1 C=Ostretching lipids
1632-3	Ring C−C stretch of phenyl, C=C uracil, C=O		o	o		1630-1700cm−1 Amide I region
1826		* √ □				
1920-5		□	ox	x□	xo	*Only in cancer cells*
1943		□	xo	x□	xo	
1944-5			o		o	
1969			x	x	x	
1971			o		o	
1992-3			xo	x	xo	
2018			o		o	
2031			o			
2359		* √ □				*Only in control cells*
2761	CH_3modes	*				*Only in control cells*
2764	Streching N−H NH_3^+	√				
2772		√				
2777		□				

2781		√				
2790-2			o			
2848			o	o	o	
2851-4	CH_2 symmetric (lipids)	∗ □	xo ∗	xo □	xo	2800-3000 cm^{-1} C-H Lipid region CH_3 CH_2 lipid & proteins
2855			o	o	o	
2856		□	ox	ox	ox	
2857			ox	ox	ox	
2858			o	o	o	2846-80 cm^{-1} C-H stretching band Stretching C-H, ν_s CH_2, lipids, fatty acids Symmetric stretching of CH_2 of acyl chains lipids
2859			o	o	o	
2860	Stretching C−H		o	o	o	
2916	Cholesterol, phospholipids and creating (higher in normal tissues) Stretching vibrations of CH_2 & CH_3 of phospholipids, cholesterol and creatine	∗	x	x	x	2800-3100 cm^{-1} C-H stretching vibrations of methyl CH_3 & methylene CH_2 groups & olefins
2917	Stretching C−H	∗	x	x	x	
2918	Stretching C−H	∗	x	x	x	

2919	Stretching C−H	∗	x	x	x	
2920		∗	x	x	x	
2921		∗	x	x	x	Cholesterol, phospholipids and creating (higher in normal tissues) (2916)
2922	Asymmetric stretching vibration of CH_2 of acyl chains (lipids)	∗	x	x□	x	
2923	2923-33 cm^{-1} C−H stretching band in malignant tissues	∗	x	x□	x	
2924		∗	xo	xo□	xo	Stretching vibrations of CH_2 & CH_3 of phospholipids, cholesterol and creatine
2925	C−H stretching bands in normal tissues ν_{as} CH_2 lipids	∗	xo ∗	xo □	xo	
2926	StretchingC−H	∗	xo	xo	xo	
2927		∗	xo	xo	xo	
2928		∗	xo	xo	xo	Stretching C-H (2923/8)
2930			o	o	o	
2962	CH_3 modes			o □		
2964-5	Stretching C-H	∗ o	□			

3016	CH_2 aromatic stretch		o			Asymmteric stretching vibration of CH_2 of acyl chains (lipids) (2922) ν_{as} CH_2 of lipids (2925)
3055	Amid B (N−H stretching)				∗	
3086					∗	
3100					∗	
3340		∗ √ □			∗	*Only in control cells*
3435	Stretching O−H asymmetric		o	□ ox		
3451		∗ √ □		x		
3458-9			∗xo		∗x	

Appendix B

Appendix B

B.1 Cell segmentation

The scanning region for quantification analysis was $45 \times 45\ \mu m^2$ (x-y), resolution 500×500 pixels, 20 accumulation per image, acquisition time $\sim$ 20 sec/image. Moreover, to obtain total information of the tissue (3D image) was scanned in z dimension (1 μm step). First the images were normalized with maximum global value for all slices of each tissue in MATLAB. Then the stacks were imported to the Image J program.

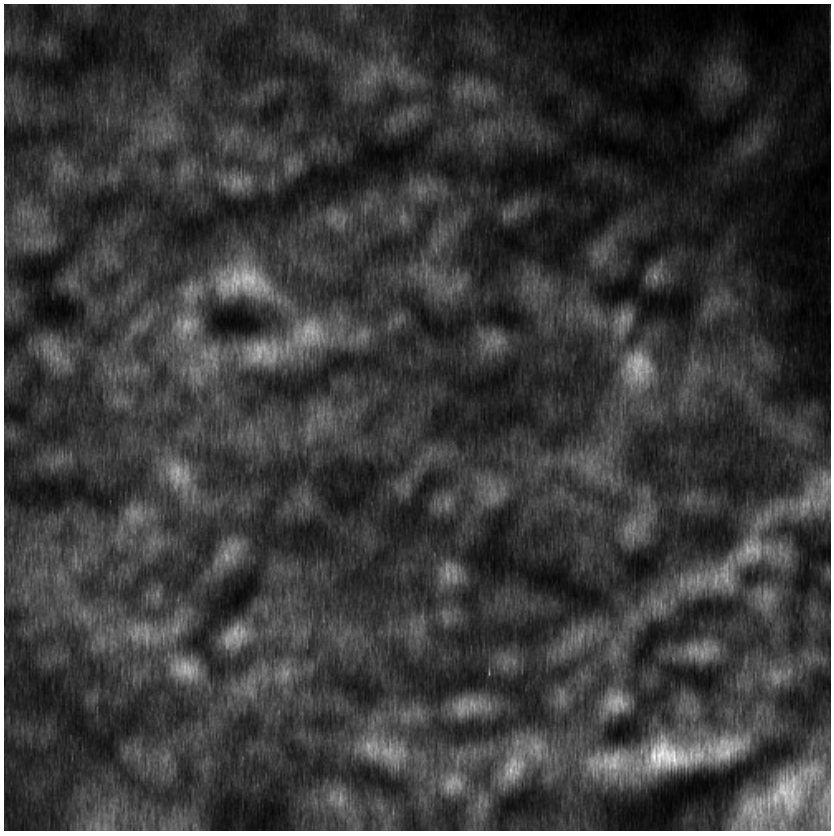

Figure B.1: Characteristic scanning region of tissue.

Image J was used to remove the noise and smooth the tissues.

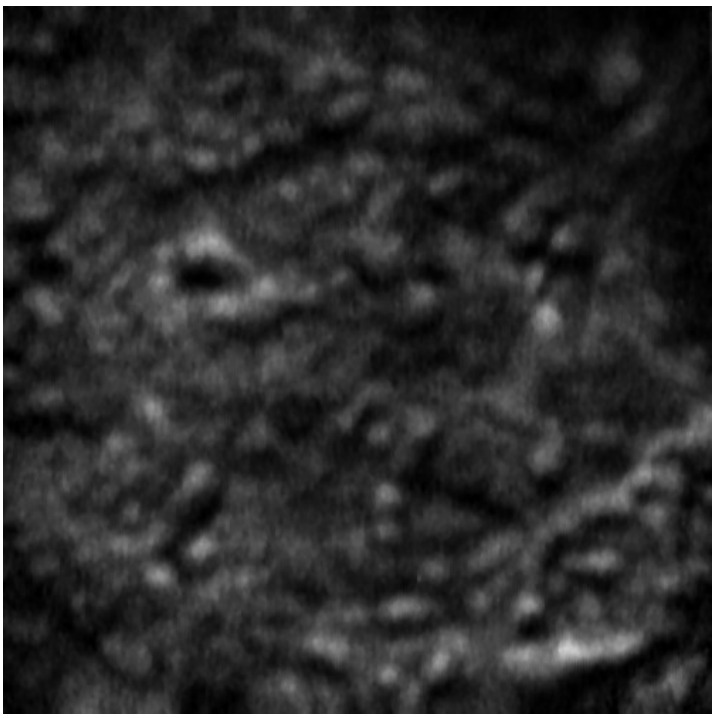

Figure B.2: Smoothing of tissue

After processing the tissues, the cell segmentation was performed. Cell limits were then recognized manually in the tissue, by looking at all the z slices of the tissue.

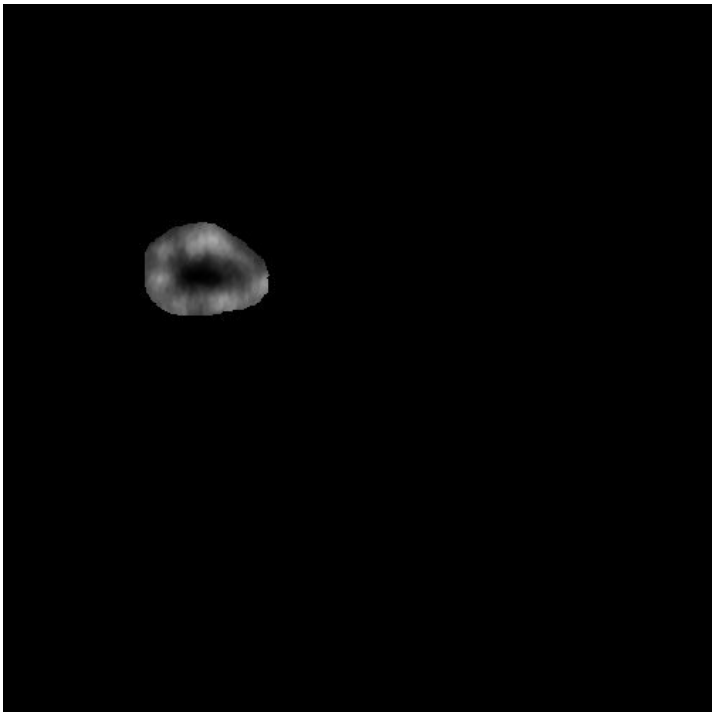

Figure B.3: Cell segmentation

The unwanted signal was then excluded.

Continuously, a threshold was adjusted, in order to calculate only the higher THG signal (almost 25%).

Figure B.4: Set threshold

Particles were then measured and analyzed. In this analysis the number of values and their mean pixel values were calculated.

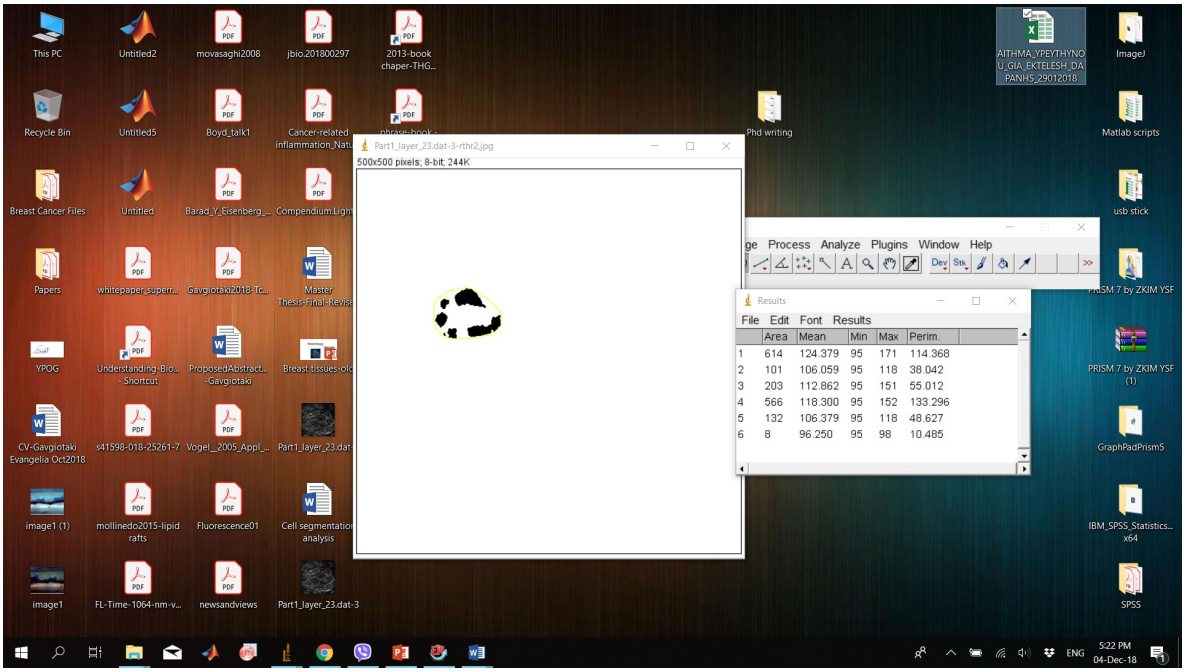

Figure B.5: Measure mean area of particles

This result was saved in an excel format and then using a MATLAB script the mean area THG value was calculated for all the slices of each cell.

B.2 THG intensity quantification

This analysis did not require cell segmentation as previously described. In this case all the tissue area was calculated after setting a constant threshold (see Chapter 4).